2017

CO2 Capture From Flue Gas By A PSA Process Using A Novel Structured Adsorbent

Nima Mohammadi
University of South Carolina

CO_2 CAPTURE FROM FLUE GAS BY A PSA PROCESS USING A NOVEL STRUCTURED ADSORBENT

by

Nima Mohammadi

Bachelor of Science
Isfahan University of Technology, 2008

Master of Science
Sharif University of Technology, 2010

Submitted in Partial Fulfillment of the Requirements

For the Degree of Doctor of Philosophy in

Chemical Engineering

College of Engineering and Computing

University of South Carolina

2017

Accepted by:

James A. Ritter, Major Professor

Armin D. Ebner, Committee Member

Harry J. Ploehn, Committee Member

Jamil A. Khan, Committee Member

Cheryl L. Addy, Vice Provost and Dean of the Graduate School

DEDICATION

To my beloved parents whom without their support, encouragement and sacrifice none of my achievements would be possible.

ACKNOWLEDGEMENTS

I want to express my deepest appreciation to my advisor Dr. James A. Ritter, for being a great mentor for me. It was a privilege to be supervised by a world class researcher and a true expert like him. Without his guidance, encouragement and support this dissertation would have not been possible. I would particularly like to thank my second advisor Dr. Armin D. Ebner for his ingenious comments and suggestions and patience while teaching me the art of problem solving. Many thanks to my committee members, Dr. Harry Ploehn, Dr. Jamil Khan, and Dr. John Weidner for their time, and guidance.

I am grateful to Dr. Marjorie Nicholson not only for all her help in carrying out my Experiments but also for being kind, caring and supportive throughout my PhD program. I would also like to express my thanks to all my previous and present research group mates, Dr. Anahita Abdollahi Govar, Dr. Fan Wu, Dr. Mohammad Iftekhar Hossain, Dr. Lutfi Erden, Dr. Hanife Erden.and Dr. Atikur Rahman.

I owe much gratitude to my hard working parents Aslan Mohammadi and Farideh Bigdeli for all the sacrifices they have made, their love and endless care.

ABSTRACT

First adsorption equilibrium isotherms for N_2, O_2, Ar and CO_2 on zeolite 13X were measured at three temperatures (25, 50, 75 °C) and pressures up to 110 kPa with a volumetric method and validated by also measuring the same isotherms with a gravimetric system.

Then a comprehensive 2-D mathematical model was developed to study the fundamentals of adsorption processes in parallel channel structured adsorbents. The results clearly indicated that under studied circumstances the plug flow condition can be assumed and therefore the system is not subject to premature breakthrough.

The pressure drop of corrugated structured adsorbents with narrow triangular channels was then investigated both experimentally and numerically. A 1-D model in the form of Darcy-Weisbach equation was developed and successfully tested for different components under different density and viscosity conditions.

Next DAPS equipped with 1-D pressure drop expression was used in preliminary studies proving the capability of structured adsorbent in achieving the desired performance with bulk densities as low as 240 kg/m3. Then a complex single bed setup was equipped with the structured adsorbents and was analyzed with breakthrough runs revealing the average adsorbent layer thickness and the significant dispersion in the system. A set of experiments tested the designed PSA cycle with the newly developed adsorbent. Promising results for recovery (> 93.0 vol% in all cases except one) was obtained. Experimental

results were validated with accuracy using DAPS concluding that the adsorbent bulk density was too low to produce high purity CO_2 and that by increasing the adsorbent layer thickness this issue can be resolved. Then a step by step scale up procedure was followed using validated DAPS. Results indicated that although structured adsorbents are an excellent choice for high pressure applications, they encounter inherent limitations under vacuum conditions leading to insufficient regeneration during CnD and LR steps and a lowered performance. It was shown that reducing the bed size by increasing the number of the units along with increasing the regeneration time by increasing the total cycle time resolved the problem and the desired performance was achieved.

TABLE OF CONTENTS

LIST OF TABLES

LIST OF FIGURES

LIST OF SYMBOLS

a	Side length of triangular cells, m
$B_{1,i}$	Three process Langmuir model parameter for component i, K^{-1}
$B_{2,i}$	Three process Langmuir model parameter for component i, K^{-1}
$B_{3,i}$	Three process Langmuir model parameter for component i, K^{-1}
$b_{1,i}$	Three process Langmuir model parameter for component i, kPa^{-1}
$b_{2,i}$	Three process Langmuir model parameter for component i, kPa^{-1}
$b_{3,i}$	Three process Langmuir model parameter for component i, kPa^{-1}
$b^0_{1,i}$	Three process Langmuir model parameter for component i, kPa^{-1}
$b^0_{2,i}$	Three process Langmuir model parameter f or component i, kPa^{-1}
$b^0_{3,i}$	Three process Langmuir model parameter for component i, kPa^{-1}
$B_{m,i}$	Heat of adsorption for component i on site m, K^{-1}
$b_{m,i}$	Affinity parameter for site m in TPL isotherm for comp. i, kPa^{-1}
$b^0_{m,i}$	Pre-exponential constant for temperature dependence of $b_{m,\mathrm{I}}$, kPa^{-1}
C_D	Cells per unit area of structure cross section, cells per square inch (CPSI)
C_p	Gas phase heat capacity, J/(mol.K)
$C_{p,,m}$	Metal layer heat capacity, J/(mol.K)

$C_{p,,i}$	Gas phase heat capacity of component i, J/(mol.K)
$C_{p,i,a}$	Adsorbed phase heat capacity of component i, J/(mol.K)
C_T	Total molar concentration, mol/m^3
C_v	Valve coefficient
D_h	Channel hydraulic diameter, m
d_p	Particle diameter, m
d	Pipe diameter, m
D_x	Diffusion coefficient in x direction, m^2/s
D_z	Diffusion coefficient in z direction, m^2/s
F	Molar flow rate through the valve, L(STP)
f_1	Fitting parameter
f_2	Fitting parameter
f_D	Darcy friction factor
g_x	Gravitational acceleration component in x direction, m/ s^2
g_z	Gravitational acceleration component in z direction, m/ s^2
ΔH_i	Isosteric heat of adsorption of component *i*, J/mol
$\vec{\imath}$	Unit vector in x direction
I	Identity matrix
$\vec{\jmath}$	Unit vector in y direction
$\vec{k}$	Unit vector in z direction
K_x	Gas phase conductivity in x direction, W/m.K
K_z	Gas phase conductivity in z direction, W/m.K
K_{eff}	Effective conductivity of wall and adsorbent layer in z direction, W/m.K

k_i	LDF mass transfer coefficient of component *i*, s^{-1}
L	Length of the column, m
L	Channel length, m
l_e	Entrance region length, m
M	Average molecular weight of the gas phase
M_i	Molecular weight of component i
m'	Adsorbent mass per unit area of contactor, kg/ m^2
N	Number of components
$\vec{n}$	Outward unit normal vector
P	Pressure, kPa
P_0	Outlet pressure or pressure outside the valve, kPa
$Pout$	Channel outlet pressure, Pa
q_i	Adsorbed phase loading of component *i*, mol kg^{-1}
q_i^*	Adsorbed phase equilibrium loading of component *i*, mol kg^{-1}
$q^s_{1,i}$	Three process Langmuir model parameter for component *i*, mol kg^{-1}
$q^s_{2,i}$	Three process Langmuir model parameter for component *i*, mol kg^{-1}
$q^s_{3,i}$	Three process Langmuir model parameter for component *i*, mol kg^{-1}
$q^s_{m,i}$	Maximum possible adsorbed amount of component *i* on site m, mol/Kg
R	Universal gas constant, kPa.m^3/mol/K
Re	Reynolds number
r_p	Adsorbent particle radius, m
S_g	Gas phase specific gravity relative to air at 1 atm and 21.45 ^oC
T	Temperature, K

t	Time, s
T	Temperature, K
$\vec{u}$	Velocity vector, m/s
u	Velocity component in x direction, m/s
v	Velocity component in y direction or interstitial velocity, m/s
v_s	Superficial velocity in packed bed, m/s
V_{max}	Maximum velocity in parabolic laminar velocity distribution, m/s
V_X	Velocity component in x direction, m/s
V_y	Velocity component in y direction, m/s
w	Velocity component in z direction, m/s
w_{in}	Channel inlet velocity, m/s
x	Position in x direction, m
y	Position in y direction, m
y_i	Mole fraction of component *i*
z	Position in z direction, m
δ	Half width of the channel, m
δ_a	Coated adsorbent layer thickness, m
δ_m	Metal foil thickness, m
ε	Adsorbent layer, packed bed or corrugated structure porosity
ε_a	Adsorbent layer porosity
ε_b	Column porosity
θ	Feed throughput, L(STP) kg^{-1} hr^{-1}
μ	Gas viscosity, Pa.s

ρ	Average gas phase density, kg m^{-3}
ρ_a	Adsorbent layer density, kg m^{-3}
ρ_m	Density of the metal wall, kg/m^3
τ	Viscous stress tensor, Pa
ω_i	Mass fraction of component *i*
$\omega_{f,i}$	Mass fraction of component *i* in feed

LIST OF ABBREVIATIONS

CMB.....Component Mass Balance

CnD.....Counter- Current Depressurization

CoD.....Co-Current Depressurization

EB.....Energy Balance

Eq.....Equalization-down

Eq*.....Equalization-up

HR.....Heavy Reflux

LDF.....Linear Driving Force

LPP.....Light Product Pressurization

LR.....Light Reflux

OMB.....Overall Mass Balance

PSA.....Pressure Swing Adsorption

TGA.....Thermogravimetric Analyzer

TPL.....Three Process Langmuir

VSA.....Vacuum Swing Adsorption

CHAPTER 1

ADSORPTION EQUILIBRIUM OF N_2, O_2, AR AND CO_2 ON 13X ZEOLITE

1.1 SUMMARY

Adsorption equilibrium isotherms for N_2, O_2, Ar and CO_2 on zeolite 13X were measured at three temperatures (25, 50, 75 °C) and pressures up to 110 KPa with a volumetric method. Results were validated by obtaining adsorption isotherms using a microbalance gravimetric system at the same temperatures and pressures up to 160 KPa and comparing the volumetric and gravimetric data. Three Process Langmuir (TPL) model was applied to correlate adsorption isotherm and was able to described pure component equilibria very well for all the adsorbates. Also isosteric heats of adsorption were calculated as a function of loading based on the Clausius-Clapeyron equation by using obtained set of fitting parameters for TPL and Toth models. The experimental data, fitting parameters and heat of adsorption information presented in this work can be used for any type of adsorption processes simulation and design utilizing 13X zeolite and analyzed gases or for comparing newly developed adsorbents to commercial 13X zeolite.

1.2 INTRODUCTION

Separation and purification of gas mixtures by adsorption has become a major attraction in chemical and oil related industries. Among various processes Pressure swing adsorption (PSA) technology has gained interest due to low energy requirements and low capital investment cost.

Various types of adsorbents are used in the adsorption based gas separation and purification processes. Synthetic zeolites are widely used in adsorption separation processes as a result of their attractive adsorption properties among the adsorbents used in industry, zeolite 13X shows superior adsorbent features because of its high affinity, high selectivity and working capacity for certain components.

Gas separations by adsorption processes have found massive applications in upgrading both renewable and nonrenewable energy sources such as landfill gas (LFG) and natural gas (NG) **[1]**. These gases contain substantial amounts of methane (50+vol %) balanced by carbon dioxide, nitrogen and other impurities. Natural gas is a fuel with special advantages such as being clean burning and relatively low cost, but it contains some contaminants like carbon dioxide that have to be removed before the liquefaction process in order to satisfy pipeline grade specifications **[2]**. Since zeolite 13X has quite different affinity and capacity for components of these gaseous mixtures, it is one of the preferred adsorbents for separation of such streams.

For application regarding industrial flu gas, the removal and sequestration of CO_2 from flue gas is required to decrease GHG emissions. Because of the large flow-rates involved, as well as the relatively low CO_2 concentration and the low pressure of the flue

gas, this is a particularly difficult separation **[3]**.Absorption is currently the technology of choice for CO_2 removal from flue gas but ongoing studies are investigating the possible application of adsorption to this problem. Many works have used zeolite 13X to recover CO_2 from a binary mixture of CO_2 and N_2 **[4]**.

Air Separation, utilizing nitrogen selective molecular sieve zeolites of type A (5A) or X (13X-NaX, LiX, or LiLSX), by means of pressure swing adsorption (PSA) has remarkably increased in the past 3 decades **[5]**.

Pressure swing adsorption (PSA) or vacuum swing adsorption (VSA) has been reported in literature as an effective technology for propane/propylene separation. For the purification of propylene with polymer grade specifications, **Da Silva et al. [6]** presented a VSA cycle using a 13X commercial zeolite.

In many studies, the capacity of newly developed adsorbents is compared with activated carbons and/or zeolites, which are widely applied in present industrial fields. Furthermore, since adsorption processes are based on preferential adsorption of desired gases onto a porous adsorbent at a certain pressure, adsorption equilibrium data of each component in a mixture are the most important factors in the design of adsorption processes.

The effluent gases from power generators, coal gasifiers, coke combustors, reformers, water–gas-shift reactors and feed gases for air separation, natural and landfill gas upgrading and light hydrocarbon separation processes consist of a combination of O_2, N_2, Ar, CO_2, CO, CH_4, C_2H_4, C_2H_2, C_3H_8, C_3H_6 and H_2 after undergoing various pretreatment processes such as particle removal, sour gas removal, sulfur

removal/recovery, and/or drying. To treat such effluent gases using adsorption processes, it is necessary to measure accurate single-component adsorption equilibrium data **[7].**

To design adsorption processes, a better knowledge about how these processes work is needed. In the past, such beds were designed empirically through extensive experimentation process development units, so it was both expensive and time consuming. Modeling and simulation of such processes improves process efficiency and reduces costs and time associated with design. Adsorption isotherm data are main information that should be gathered accurately before running any kind of simulation.

As well as isotherm data, heats of adsorption are also required to calculate energy balances for adsorption processes. The isosteric heat of adsorption can be obtained by direct measurement using dosing calorimetry **[8]**, or can be estimated indirectly via adsorption equilibria with temperature dependency **[9].**

Isotherm data can be gathered by volumetric, gravimetric and chromatographic techniques. The volumetric method is considered as an advantageous way to measure adsorption isotherms as it is easy to develop and relatively cheap especially at low pressure ranges.

In this work, using volumetric method we have measured adsorption equilibrium of pure Carbon DioxideNitrogen, Oxygen, and Argon on Zeolite 13X adsorbent supplied by Grace at 25, 50 and 75 °C and in the pressure range of (0 to 110) kPa. Isotherms measured by the volumetric setup was compared to the data gathered from a gravimetric system to validate the results. The experimental data was fitted with the Three Process Langmuir model. Heats of adsorption for pure-component adsorption are obtained from the Clausius-Clayperon equation by evaluating the adsorption isotherms at different

temperatures at constant loading. Results can contribute to the design of various adsorption processes which include the aforementioned gases and zeolite 13X. In addition, they can be used for the evaluation of adsorption capacity for newly developed adsorbents.

1.3 EXPERIMENTAL

The commercial adsorbent used in this work was supplied by Grace (Sylobead grade 544 zeolite 13X 8-12 mesh sizes) and used as received. For O_2, N_2 and Ar isotherms approximately 3.5 g of 13X was used. Due to high affinity to 13X zeolite and large volume of gas needed for equilibrium for CO_2 sample size was reduced and approximately 0.5 g was utilized. Average diameter of the zeolite beads were 3 mm. All the gases in this study had purities higher than 99.99%. The gases used in this work were supplied by Airgas.

Pure component adsorption equilibrium isotherms for N_2, O_2, Ar and CO_2 on zeolite 13X were measured at three different temperatures (i.e. 25, 50 and 75 C) by using a volumetric system from micromeritics (ASAP2010, located at the University of South Carolina). A water bath connected to a chiller was used to keep the sample at a desired temperature throughout the experiment. Operation pressure range provided by this system is from 0 to 127 KPa. The molecular drag pump can create vacuums down to $1.3 * 10^{-6}$ KPa in the system.

Volumetric method involves measuring the pressure change in a known volume of sample gas exposed to an adsorbent sample. As the gas is adsorbed and allowed to come to equilibrium with the adsorbent, the measured decrease of pressure in the closed system indicates the amount of gas adsorbed under the given isothermal conditions.

Data were collected for the equilibrium pressure range of 0.001 to 110 KPa. For each isotherm system was programed to obtain 60 to 120 equilibrium points at specific pressures with logarithmic from low pressure distribution. A complete run for an isotherm takes roughly about 12 hours. For each point equilibration is reached when the pressure change per equilibration time interval (first derivative) is less than 0.01% of the average pressure during the interval. After measuring the last point the run is complete and system automatically backfills the sample tube with analysis gas.

Prior to each isotherm measurement, the zeolite 13X was regenerated at 350 C for 16 hours under a vacuum of less than 1.33×10^{-5} KPa. In order to prevent structural damage caused by desorbing water steam, sample temperature was gradually increased in 25 C steps every 30 minutes up to 150 C and then 50 C steps every 30 minutes up to the regeneration temperature of 350 C.

After regeneration the weight of the sample tube (filled with He to 104 KPa) was subtracted from the weight of the empty sample tube filled with He to calculate the weight of the regenerated sample. Free space or available volume was measured by ASAP2010 using non-adsorbing He gas then helium was evacuated from the system by applying vacuum for 1 hour.

In addition to the volumetric system, adsorption equilibrium isotherms were also measured by using a gravimetric system. Gravimetric measurements were done by using VTI Microbalance device which was located in University of South Carolina. The device mainly consists of a closed chamber of microbalance, 4 pressure transducers (MKS) for different pressure ranges (0-10 torr, 0-100 torr, 0-1000 torr, and 0-10000 torr),

thermocouples, and a molecular drag pump (adixen, drytel 1025). The sample chamber can be heated to elevated temperatures by using a band heater when the sample is being regenerated. A hot water bath (VWR) port can be replaced around sample holder for maintaining the required temperature when adsorption isotherm data is taken. Temperature, pressure and weight data can be read and recorded continuously. In order to get the equilibrium adsorption isotherms for each temperature, a small amount of analysis gas was injected which caused an increase in the pressure, temperature and weight of sample. First point of adsorption isotherm raw data was recorded once the sample weight, temperature and pressure stabilized. This procedure takes roughly 20 minutes. Same procedure was repeated for higher pressures by dosing the sample gas stepwise and waiting till the adsorbent equilibrates with the analysis gas. The raw data for all pressures were further analyzed for correction of gas buoyancy. Hence the possible error in the equilibrium gas adsorption isotherms due to buoyancy was corrected.

Pure helium measurements were carried out to correct isotherms measurements of individual gases from buoyancy effects by assuming that helium adsorption affinity onto 13X zeolite is negligible relative to that of the gasses being evaluated. Unique helium buoyancy runs were carried out at each of the temperatures considered in this study (i.e., 25, 50 and 75) for a range of pressures that were large enough to accurately determine an accurate slope of the instrument reading and the pressure of He $m_{He}(T)$. The weight gained G_i solely due to adsorption of the evaluated gas onto the adsorbent is hence given by

$$G_i(P,T) = R_i(P,T) - W_o - R_{b,g,i}(P,T) \quad (1)$$

Where R_i is instrument weight reading at the given pressure P and temperature T, W_o is the instrument reading at zero pressure and $R_{b,g,i}$ is the correction due to buoyancy given by

$$R_{b,g,i}(P,T) = m_{He}(T) * P * \frac{M_g}{M_{He}} \quad (2)$$

With M_g and M_{He} being the molecular weights for the gas being evaluated and He, respectively. The loading on a sample in moles per mass is thus finally calculated as

$$q_i(P,T) = \frac{G_i(P,T)}{W_o} * \frac{1000}{M_g} \quad (3)$$

Adsorption equilibrium data needs to be accurately correlated for later use in a specific gas separation application. In this paper, Three Process Langmuir (TPL) and Toth models have been used to correlate the experimental adsorption equilibrium data. The fitting parameters obtained by simultaneously regressing all of the experimental single-gas data measured at every temperature by minimizing $\sum_{i=1}^{n}\left(n_{i,model} - n_{i,experimental}\right)^2$ using Solver in MS Excel. It must be noted that parameters were rescaled such that their order of magnitude differing from 0.1 to 10.

The TPL model which is an extension of the Dual Process Langmuir model describes the adsorption of a gas on a heterogeneous adsorbent composed of three energetically different but homogeneous sites**.** The free energy of adsorbate-adsorbent on each site is assumed as constant. **Table 1.1** shows the main, dependent and heat of adsorption equations for TPL model, where q_j^s and b_j are respectively the saturation capacity and affinity parameter on site j, and P is the absolute pressure. E_j and $b_{j,o}$ are respectively the adsorption energy of the gas and the pre-exponential factor on site j **[10].**

The isosteric heat of adsorption is defined as the ratio of the infinitesimal change in the adsorbate enthalpy to the infinitesimal change in the amount adsorbed. In addition to equilibrium adsorption isotherms, heat of adsorption is also essential for the design and operation of the gas separation process via adsorption. Heat of adsorption is typically estimated from adsorption isotherm models by using the Clausius-Clapeyron equation:

$$q_{st,i} = RT^2 \left[\frac{\partial lnP}{\partial T}\right]_{q_i} = -R \left[\frac{\partial lnP}{\partial (1/T)}\right]_{q_i} \quad (4)$$

Where R is the universal gas constant, P is the absolute pressure, T is the absolute temperature, and n_i is the amount adsorbed of component i. **Eq. 4** assumes ideal gas behavior and that the adsorbed phase volume is negligible **[11].** The subscript n_i indicates the amount adsorbed is held constant while evaluating the partial derivative, which necessarily makes $q_{st,i} = f(n_i)$.

Eq. 4 can also be written in the following useful form using the triple chain rule:

$$q_{st,i} = -\frac{RT^2}{P}\left[\frac{\left(\frac{\partial n_i}{\partial T}\right)_P}{\left(\frac{\partial n_i}{\partial P}\right)_T}\right] \quad (5)$$

If an adsorption isotherm model is available as ni = f(P,T), then **Eq. 5** provides an analytic expression for qst,i by simple partial differentiation of the model **[12]**. All derived equations are also given in **Table 1.1.**

1.4 RESULTS AND DISCUSSION

The excess adsorption isotherms for N_2, O_2, Ar and CO_2 on zeolite 13X were obtained at temperatures of 25, 50, 75 °C and pressures up to 110 KPa with the volumetric apparatus. For data validation purposes adsorption isotherms were also measured by a microbalance gravimetric system at same temperatures and pressures up to 160 KPa. The

data gathered from all the experiments is presented in **Table 1.2 to 1.9.** Three Process Langmuir model was applied to correlate adsorption isotherm for all gases on zeolite 13X. In some cases specially the adsorbates with linear isotherms single or dual process Langmuir is accurate enough to correlate the experimental data so in order to decrease the complexity of the model one or two processes were set to zero and instead of three process Langmuir dual or single process Langmuir was utilized. **Table 1.10** shows the Three Process Langmuir models parameters fitting the experimental data in the full experimental range. Also isosteric heats of adsorption (q_{st}) were calculated based on the equations derived from models and by using obtained sets of fitting parameters.

Figures 1.1 to **1.4** show the equilibrium adsorption isotherms of N_2, O_2, Ar and CO_2 respectively. In addition to normal scale, isotherms were also reported in log-log scale to visualize the results in low pressure or Henry's law region. As shown in the log-log scale figures measured isotherm for most cases are linear with the slope of 1 as expected in Henry's law region. Measuring equilibrium points in low pressure is very sensitive, especially for gases with high affinities towards the solid and at lower temperatures, like CO_2 at 25C .Under these circumstances a small contamination or exposure to the test gas before the experiment or a not deep enough regeneration can lead to lower equilibrium loadings and a larger than one slope for linear part of the isotherm.

Points show experimental data and solid lines are Three Process Langmuir model. It can be seen from the figures that for all gases model fits the experimental data very well in the entire pressure range. All species have isotherms that fall under the typical type I isotherm shape according to BDDT classification which is consistent with zeolite's microporous structure.

According to the adsorbate–adsorbent potential theory **[13]** the potential is comprised of dispersion energy , close-range repulsion energy , induction energy , interaction energy between electric field and a permanent dipole moment, interaction energy between field gradient and a quadrupole moment . Since zeolite is a kind of adsorbent with charges on the solid surface, electrostatic interactions often dominate the adsorption at low equilibrium pressure or adsorption loadings **[13, 14, 15],** also dispersion energy and repulsion energy make little difference for all adsorption systems therefore emphases are put on electrostatic interactions in this discussion.

Electrostatic interactions are determined by 3 characteristics of the adsorbate molecules, dipole moment, quadrupole moment and polarizability. These physical properties were collected for all studied gases and listed in **Table 1.11** in order to compare the nature of different thermodynamic affinity between the adsorbate and adsorbent. **[16]** O_2 and Ar have almost overlapping isotherms but nitrogen has much greater capacity compared to O_2 and Ar and all three gases have overall low equilibrium loadings.

O_2 and Ar and N_2 are non-polar molecules thus have no dipole moments but N_2 has a permanent quadrupole moment that interacts with the cations in13X zeolite structure which explains the greater affinity of N_2 towards 13X surface. Although CO_2 molecule does not have a dipole moment, its polarizability and especially large quadruple moment are responsible for its significant equilibrium capacity.

In order to validate the volumetric system results, in **Figures 1.5** to **1.8** isotherm data points collected by volumetric set up are compared to gravimetric system measurements for N_2, O_2, Ar and CO_2. As shown in figures for all gases at different

temperatures two methods have very good agreement which confirms the accuracy of results.

Parameters obtained through fitting the models to experimental data were used in the derived isosteric heat of adsorption equations shown in **Table 1**. **Figures 1.9** to **1.12** present the Isosteric heat of adsorption versus loading for all the studied gases. For the adsorbates like N_2, O_2 and Ar that their interaction with 13X zeolite can be described by single process Langmuir isotherm, solid surface is homogenous for gas molecules therefore Isosteric heat of adsorption remains constant with loading. In cases CO_2 three process Langmuir equation should be used, for these systems qst values decreases by increasing loadings which indicates the heterogeneity of the adsorbate-adsorbent system **[9].** CO_2 needs three process Langmuir to fit the data that confirms the CO_2-13X system is more heterogeneous which causes sharper decrease of heat of adsorption with loading.

1.5 CONCLUSION

A commercial 13X zeolite from Grace was studied in this work and adsorption equilibrium isotherms for N_2, O_2, Ar and CO_2 were measured at three temperatures (25, 50, 75 °C) and pressures up to 110 kPa. A volumetric method was utilized to collect equilibrium data and its results were validated by obtaining adsorption isotherms using an in house microbalance gravimetric system at the same temperatures and pressures up to 160 kPa and by comparing the volumetric and gravimetric data. Differences in isotherms can be described by affinity difference relative to different adsorbate molecules which derives from molecule multipole moments and polarizability. Three Process Langmuir (TPL) model were applied to correlate adsorption isotherm and were able to describe pure component equilibria very well. Also isosteric heats of adsorption were calculated as a

function of loading based on the Clausius-Clapeyron equation by using obtained set of fitting parameters for TPL model. Differences in the number of TPL model parameters needed and trend of the heat of adsorption curves were related to gas-solid system homogeneity, heterogeneity.

1.6 TABLES

Table 1.1 TPL adsorption equilibrium model and derived heat of adsorption equations

Main Equation	$$q = \left(\frac{q_1^s b_1 P}{(1+b_1 P)}\right)_{site\ 1} + \left(\frac{q_2^s b_2 P}{(1+b_2 P)}\right)_{site\ 2} + \left(\frac{q_3^s b_3 P}{(1+b_3 P)}\right)_{site\ 3}$$
Dependent Equations	$$b_j = b_{j,o} exp\left(\frac{E_j}{T}\right)$$
Isosteric Heat of Adsorption Equation	$$q_{st} = \frac{\left[\frac{q_1^s b_1 E_1}{(1+b_1 P)^2} + \frac{q_2^s b_2 E_2}{(1+b_2 P)^2} + \frac{q_3^s b_3 E_3}{(1+b_3 P)^2}\right]}{\left[\frac{q_1^s b_1}{(1+b_1 P)^2} + \frac{q_2^s b_2}{(1+b_2 P)^2} + \frac{q_3^s b_3}{(1+b_3 P)^2}\right]}$$

Table 1.2 Adsorption Equilibrium Isotherm Data of Nitrogen on zeolite 13X at 25, 50, and 75 ^{o}C measured by ASAP2010

T=25 ^{o}C		**T=50 ^{o}C**		**T=75 ^{o}C**	
P	**q**	**P**	**q**	**P**	**q**
(kPa)	**(mol/kg)**	**(kPa)**	**(mol/kg)**	**(kPa)**	**(mol/kg)**
0.0916	0.0004	0.1109	0.0002	0.1231	0.0002
0.1453	0.0006	0.1709	0.0004	0.1804	0.0002
0.1673	0.0007	0.2119	0.0005	0.2045	0.0003

0.2087	0.0009	0.2683	0.0006	0.2696	0.0004
0.2653	0.0011	0.3416	0.0008	0.3409	0.0005
0.3412	0.0015	0.4311	0.0010	0.4326	0.0006
0.4303	0.0019	0.5473	0.0013	0.5483	0.0008
0.5464	0.0024	0.7238	0.0017	0.7242	0.0010
0.7222	0.0031	0.9135	0.0021	0.9037	0.0012
0.9057	0.0039	1.1416	0.0026	1.1644	0.0016
1.1509	0.0048	1.4676	0.0034	1.4568	0.0020
1.4528	0.0060	1.8451	0.0042	1.8526	0.0025
1.8400	0.0076	2.3575	0.0053	2.3608	0.0031
2.3354	0.0095	2.9590	0.0066	2.9792	0.0039
2.9642	0.0119	3.7785	0.0083	3.7808	0.0050
3.7668	0.0150	4.8152	0.0105	4.8198	0.0063
4.7976	0.0190	6.1007	0.0133	6.1088	0.0080
6.0928	0.0239	7.3829	0.0159	7.5109	0.0098
7.1756	0.0280	9.7485	0.0208	9.8386	0.0127
9.6284	0.0370	12.5605	0.0265	12.5692	0.0162

12.5480	0.0475	15.9710	0.0333	15.9791	0.0204
15.9635	0.0596	20.3334	0.0420	20.3332	0.0258
20.3150	0.0747	25.9128	0.0529	25.9049	0.0326
25.9110	0.0938	33.0686	0.0666	33.0681	0.0412
33.1279	0.1179	41.8915	0.0831	41.8834	0.0515
41.8928	0.1464	53.3574	0.1039	53.3396	0.0645
53.3523	0.1824	67.8453	0.1296	67.8784	0.0805
67.8942	0.2262	86.5016	0.1611	86.4661	0.1001
86.4757	0.2794	110.0083	0.1990	108.4670	0.1220
110.0391	0.3429				

Table 1.3 Adsorption Equilibrium Isotherm Data of Oxygen on zeolite 13X at 25, 50, and 75 ^{o}C measured by ASAP2010

T=25 ^{o}C		**T=50 ^{o}C**		**T=75 ^{o}C**	
P	**q**	**P**	**q**	**P**	**q**
(kPa)	**(mol/kg)**	**(kPa)**	**(mol/kg)**	**(kPa)**	**(mol/kg)**
2.3383	0.0027	2.3344	0.0018	2.3433	0.0013
2.9708	0.0034	2.9655	0.0023	2.9678	0.0016

3.7638	0.0043	3.7783	0.0029	3.7622	0.0020
4.7921	0.0054	4.7905	0.0036	4.7935	0.0026
6.0942	0.0068	6.0903	0.0046	6.0964	0.0032
7.4638	0.0083	7.5455	0.0056	7.6004	0.0040
9.8091	0.0109	9.8433	0.0073	9.8630	0.0052
12.5475	0.0139	12.5547	0.0092	12.5494	0.0065
15.9725	0.0175	15.9664	0.0117	15.9651	0.0082
20.3269	0.0221	20.3260	0.0147	20.3172	0.0104
25.9076	0.0280	25.8948	0.0186	25.8950	0.0130
33.0554	0.0353	32.9997	0.0234	32.9930	0.0164
41.8877	0.0442	41.8983	0.0293	41.9005	0.0204
53.3258	0.0553	53.3143	0.0365	53.3519	0.0253
67.8805	0.0690	67.8731	0.0454	67.8903	0.0312
86.4324	0.0856	86.4641	0.0560	86.4476	0.0381
110.0270	0.1057	110.0156	0.0685	110.0621	0.0459

Table 1.4 Adsorption Equilibrium Isotherm Data of Argon on zeolite 13X at 25, 50, and 75 ^{o}C measured by ASAP2010

T=25 ^{o}C		**T=50 ^{o}C**		**T=75 ^{o}C**	
P	**q**	**P**	**q**	**P**	**q**
(kPa)	**(mol/kg)**	**(kPa)**	**(mol/kg)**	**(kPa)**	**(mol/kg)**
2.1286	0.0023	2.1231	0.0016	2.3960	0.0014
2.3955	0.0026	2.3980	0.0018	2.7034	0.0015
2.6875	0.0029	2.6803	0.0020	3.0163	0.0017
3.0018	0.0033	2.9990	0.0022	3.3855	0.0019
3.3687	0.0036	3.3942	0.0025	3.7801	0.0021
3.7949	0.0041	3.7993	0.0027	4.2709	0.0023
4.2480	0.0046	4.2599	0.0031	4.7735	0.0026
4.7725	0.0051	4.7630	0.0034	5.3521	0.0029
5.3594	0.0057	5.3609	0.0038	5.9975	0.0032
6.0062	0.0064	6.0064	0.0043	6.7042	0.0036
6.6625	0.0070	6.6946	0.0047	7.5844	0.0040
7.5560	0.0080	7.5638	0.0053	8.5074	0.0045
8.4864	0.0089	8.4931	0.0060	9.5426	0.0050

9.5423	0.0100	9.5395	0.0067	10.7061	0.0056
10.7028	0.0112	10.7238	0.0075	12.0149	0.0063
12.0260	0.0125	12.0302	0.0084	13.4865	0.0070
13.5040	0.0140	13.4915	0.0094	15.1533	0.0079
15.1541	0.0157	15.1632	0.0106	17.0175	0.0088
17.0109	0.0176	17.0327	0.0118	19.1183	0.0098
19.1055	0.0197	19.1249	0.0132	21.4639	0.0110
21.4646	0.0220	21.4716	0.0148	24.1075	0.0122
24.1040	0.0246	24.1120	0.0165	27.0834	0.0137
27.0898	0.0276	27.0840	0.0185	30.4237	0.0153
30.4386	0.0308	30.4274	0.0207	34.1775	0.0170
34.2070	0.0345	34.1891	0.0231	38.3886	0.0190
38.4357	0.0386	38.4154	0.0258	43.0599	0.0211
43.0482	0.0430	43.0454	0.0287	48.3381	0.0235
48.3402	0.0480	48.3395	0.0320	54.2843	0.0261
54.2719	0.0535	54.3098	0.0357	60.9698	0.0290
60.9687	0.0597	60.9576	0.0397	68.4686	0.0322

68.4745	0.0665	68.4725	0.0442	76.9205	0.0356
76.9078	0.0741	76.9235	0.0492	86.3762	0.0394
86.3915	0.0825	86.3825	0.0545	97.0167	0.0436
97.0115	0.0917	97.0182	0.0605	108.9752	0.0480
108.9576	0.1019	108.9735	0.0670		

Table 1.5 Adsorption Equilibrium Isotherm Data of Carbon Dioxide on zeolite 13X at 25, 50, and 75 ^{o}C measured by ASAP2010

T=25 ºC		**T=50 ºC**		**T=75 ºC**	
P	**q**	**P**	**q**	**P**	**q**
(kPa)	**(mol/kg)**	**(kPa)**	**(mol/kg)**	**(kPa)**	**(mol/kg)**
0.0048	0.0324	0.0156	0.0330	0.0527	0.0324
0.0097	0.0648	0.0329	0.0660	0.1110	0.0646
0.0145	0.0972	0.0510	0.0990	0.1719	0.0966
0.0194	0.1296	0.0700	0.1320	0.2349	0.1284
0.0243	0.1619	0.0898	0.1650	0.3011	0.1599
0.0293	0.1943	0.1109	0.1980	0.3689	0.1914
0.0344	0.2267	0.1326	0.2309	0.4407	0.2225

0.0396	0.2591	0.1554	0.2638	0.5130	0.2535
0.0454	0.2914	0.1800	0.2966	0.5917	0.2852
0.0511	0.3237	0.2055	0.3294	0.6691	0.3164
0.0571	0.3561	0.2320	0.3621	0.7518	0.3459
0.0635	0.3884	0.2610	0.3947	0.8393	0.3763
0.0684	0.4218	0.2902	0.4274	0.9275	0.4063
0.0744	0.4550	0.3227	0.4599	1.0202	0.4359
0.0813	0.4883	0.3547	0.4924	1.1149	0.4653
0.0889	0.5214	0.3913	0.5248	1.2155	0.4943
0.0977	0.5545	0.4255	0.5571	1.3183	0.5239
0.1070	0.5876	0.4638	0.5893	1.4261	0.5527
0.1170	0.6207	0.5033	0.6214	1.5399	0.5811
0.1273	0.6537	0.5453	0.6534	1.6558	0.6100
0.1382	0.6868	0.5890	0.6861	1.7768	0.6389
0.1498	0.7198	0.6365	0.7184	1.9035	0.6676
0.1631	0.7528	0.6900	0.7511	2.0318	0.6962
0.1764	0.7857	0.7415	0.7829	2.1710	0.7243

0.1905	0.8187	0.7975	0.8139	2.3090	0.7524
0.2063	0.8516	0.8581	0.8456	2.4536	0.7800
0.2227	0.8845	0.9205	0.8766	2.6075	0.8071
0.2405	0.9173	0.9825	0.9073	2.7505	0.8344
0.2597	0.9501	1.0534	0.9385	2.9134	0.8609
0.2800	0.9829	1.1224	0.9699	3.0824	0.8877
0.3009	1.0156	1.1974	1.0003	3.2412	0.9142
0.3242	1.0483	1.2745	1.0303	3.4180	0.9399
0.3481	1.0809	1.3504	1.0602	3.6266	0.9705
0.3734	1.1135	1.4375	1.0896	3.8113	0.9958
0.3992	1.1461	1.5283	1.1195	3.9942	1.0216
0.4283	1.1785	1.6165	1.1498	4.2304	1.0514
0.4585	1.2109	1.7194	1.1796	4.4647	1.0815
0.4885	1.2432	1.8135	1.2095	4.7256	1.1110
0.5211	1.2754	1.9229	1.2387	4.9776	1.1410
0.5583	1.3074	2.0257	1.2680	5.2464	1.1706
0.5947	1.3401	2.1430	1.2967	5.5285	1.1995

0.6324	1.3726	2.2545	1.3254	5.8164	1.2284
0.6726	1.4047	2.3751	1.3537	6.1048	1.2573
0.7175	1.4364	2.5070	1.3822	6.4184	1.2859
0.7633	1.4683	2.6325	1.4111	6.7428	1.3142
0.8105	1.5002	2.7569	1.4392	7.0770	1.3419
0.8589	1.5313	2.9036	1.4669	7.4231	1.3697
0.9120	1.5628	3.0507	1.4937	7.7648	1.3973
0.9702	1.5943	3.1799	1.5218	8.1095	1.4250
1.0247	1.6260	3.3459	1.5487	8.4685	1.4518
1.0846	1.6566	3.4911	1.5762	8.8372	1.4781
1.1459	1.6877	3.6699	1.6022	9.2143	1.5037
1.2091	1.7190	3.8323	1.6353	9.6086	1.5291
1.2789	1.7500	3.9901	1.6621	10.0080	1.5542
1.3495	1.7800	4.1604	1.6885	10.4033	1.5791
1.4194	1.8106	4.3447	1.7141	10.8035	1.6040
1.4915	1.8413	4.5451	1.7459	11.1979	1.6288
1.5679	1.8719	4.7644	1.7771	11.6097	1.6527

1.6466	1.9023	5.0042	1.8078	16.1868	1.8772
1.7301	1.9325	5.2502	1.8383	23.2955	2.1396
1.8168	1.9624	5.4780	1.8688	29.3804	2.3159
1.9053	1.9921	5.7272	1.8992	35.6513	2.4677
2.0045	2.0213	5.9875	1.9294	39.9332	2.5569
2.0999	2.0505	6.2661	1.9586	45.7361	2.6680
2.1885	2.0808	6.5339	1.9878	51.7093	2.7674
2.2961	2.1097	6.8144	2.0169	57.2804	2.8503
2.3998	2.1392	7.1228	2.0459	63.0426	2.9292
2.5046	2.1689	7.4234	2.0747	68.8524	3.0003
2.6120	2.1977	7.7352	2.1035	74.4870	3.0645
2.7266	2.2267	8.0520	2.1326	80.2880	3.1261
2.8390	2.2552	8.3681	2.1611	86.0551	3.1811
2.9561	2.2831	8.7081	2.1886	91.6805	3.2325
3.0876	2.3111	9.0551	2.2163	97.5305	3.2812
3.2165	2.3393	9.3903	2.2436	103.2040	3.3244
3.3498	2.3664	9.7603	2.2704	108.9044	3.3665

3.4887	2.3946	10.1181	2.2973
3.6266	2.4223	10.4874	2.3235
3.7538	2.4504	10.8580	2.3492
3.9002	2.4785	11.2399	2.3752
4.0566	2.5055	11.6296	2.3997
4.2214	2.5317	16.8062	2.6833
4.3618	2.5597	23.5558	2.9493
4.5376	2.5856	29.8428	3.1357
4.6991	2.6124	36.3075	3.2916
4.8574	2.6395	39.8407	3.3642
5.0365	2.6721	45.7664	3.4730
5.2410	2.7044	51.7058	3.5645
5.4249	2.7305	57.1871	3.6422
5.6106	2.7564	63.1726	3.7151
5.8489	2.7868	68.6987	3.7780
6.0922	2.8171	74.6369	3.8364
6.3354	2.8481	80.1899	3.8878

6.5831	2.8786	86.0533	3.9370
6.8428	2.9093	91.7428	3.9804
7.1198	2.9387	97.4465	4.0222
7.4006	2.9680	103.2414	4.0616
7.6903	2.9968	108.9493	4.0977
7.9851	3.0256		
8.2889	3.0549		
8.6027	3.0837		
8.9188	3.1129		
9.2599	3.1410		
9.5989	3.1687		
9.9299	3.1967		
10.2771	3.2240		
10.6331	3.2504		
10.9999	3.2760		
11.3773	3.3017		
11.7653	3.3267		

16.0176	3.5597
24.0737	3.8579
30.4939	4.0212
37.1568	4.1522
39.6948	4.1955
45.8897	4.2858
51.5554	4.3581
57.3260	4.4231
63.1019	4.4793
68.7687	4.5292
74.5403	4.5761
80.3140	4.6178
85.9815	4.6557
91.7353	4.6922
97.5139	4.7257
103.2160	4.7559
108.9226	4.7849

Table 1.6 Adsorption Equilibrium Isotherm Data of Nitrogen on zeolite 13X at 25, 50, and 75 ^{o}C measured by Microbalance

T=25 ^{o}C		**T=50 ^{o}C**		**T=75 ^{o}C**	
P	**q**	**P**	**q**	**P**	**q**
(kPa)	**(mol/kg)**	**(kPa)**	**(mol/kg)**	**(kPa)**	**(mol/kg)**
0.7828	0.0029	0.7775	0.0015	1.0884	0.0014
1.4253	0.0049	2.0893	0.0039	2.0147	0.0025
2.0720	0.0072	4.5107	0.0085	3.4787	0.0044
3.2573	0.0115	14.0933	0.0266	7.1173	0.0088
6.1080	0.0216	67.8133	0.1259	13.3067	0.0163
13.3867	0.0467	134.6667	0.2410	27.4267	0.0334
29.2267	0.1005			71.5333	0.0850
66.5600	0.2183			147.3333	0.1697
149.6000	0.4490				

Table 1.7 Adsorption Equilibrium Isotherm Data of Oxygen on zeolite 13X at 25, 50, and 75 ^{o}C measured by Microbalance

T=25 ^{o}C		**T=50 ^{o}C**		**T=75 ^{o}C**	
P	**q**	**P**	**q**	**P**	**q**
(kPa)	**(mol/kg)**	**(kPa)**	**(mol/kg)**	**(kPa)**	**(mol/kg)**

0.6628	0.0008	0.1744	0.0001	0.7125	0.0004
1.0097	0.0012	0.2677	0.0002	1.1413	0.0007
1.8813	0.0021	0.4295	0.0003	2.1653	0.0012
2.8293	0.0030	2.2893	0.0017	5.5293	0.0029
7.1373	0.0077	5.1373	0.0038	10.4360	0.0056
16.3600	0.0174	12.6427	0.0093	13.8133	0.0074
28.8133	0.0306	28.6133	0.0209	32.0667	0.0173
69.6533	0.0735	70.4933	0.0512	66.4800	0.0363
137.7333	0.1437	132.6667	0.0945	138.8000	0.0734

Table 1.8 Adsorption Equilibrium Isotherm Data of Argon on zeolite 13X at 25, 50, and 75 ºC measured by Microbalance

T=25 ºC		**T=50 ºC**		**T=75 ºC**	
P	**q**	**P**	**q**	**P**	**q**
(kPa)	**(mol/kg)**	**(kPa)**	**(mol/kg)**	**(kPa)**	**(mol/kg)**
1.8107	0.0017	1.1559	0.0008	1.9240	0.0011
6.4320	0.0061	2.5173	0.0016	3.2720	0.0020
12.3960	0.0119	13.3067	0.0090	28.3333	0.0149

30.3067	0.0293	48.4267	0.0330	68.7333	0.0355
67.1333	0.0651	129.6000	0.0880	136.2667	0.0695
130.9333	0.1260				

Table 1.9 Adsorption Equilibrium Isotherm Data of Carbon Dioxide on zeolite 13X at 25, 50, and 75 ^{o}C measured by Microbalance

T=25 ^{o}C		**T=50 ^{o}C**		**T=75 ^{o}C**	
P	**q**	**P**	**q**	**P**	**q**
(kPa)	**(mol/kg)**	**(kPa)**	**(mol/kg)**	**(kPa)**	**(mol/kg)**
0.0092	0.0657	0.0204	0.0416	0.0460	0.0284
0.0136	0.0992	0.0416	0.0800	0.0877	0.0536
0.0259	0.1831	0.0627	0.1167	0.1533	0.0903
0.0623	0.3765	0.1148	0.1970	0.3032	0.1584
0.1075	0.5474	0.2064	0.3125	0.7784	0.3375
0.3072	0.9608	0.3724	0.4800	6.4307	1.2013
0.8672	1.4495	1.1679	0.9336	29.6800	2.2126
4.5587	2.4787	6.6240	1.8880	134.6667	3.4659
21.4400	3.6458	26.8667	2.9261		
135.2000	4.7634	136.8000	4.1460		

Table 1.10 Fitting parameters of the Three Process Langmuir model

Gas	q_1^s	b_1^o	E_1	q_2^s	b_2^o	E_2	q_3^s	b_3^o	E_3
	mol *kg^{-1}	kPa^{-1}	K	mol *kg^{-1}	kPa^{-1}	K	mol *kg^{-1}	kPa^{-1}	K
N2	1.777	7.599E-07	2370.54	0.00	0.00	0.00	0.00	0.00	0.00
O2	0.603	4.077E-06	1833.40	0.00	0.00	0.00	0.00	0.00	0.00
Ar	0.772	5.501E-06	1646.49	0.00	0.00	0.00	0.00	0.00	0.00
CO2	1.325	2.367E-8	5771.89	2.23	4.496E-8	4614.19	1.88	1.475E-08	4222.59

Table 1.11 Relevant physical properties of adsorbates

Adsorbate	Normal BP [K]	Kinetic diameter [Å]	Polarizability *10^{25} [cm^3]	Dipole moment *10^{18} [esu cm]	Quadruple moment *10^{26} [esu cm^2]
Ar	87.27	3.542	16.411	0	0
N2	77.35	3.64–3.80	17.403	0	1.52

O2	90.17	3.467	15.812	0	0.39
CO2	216.55	3.3	29.11	0	4.3

1.7 FIGURES

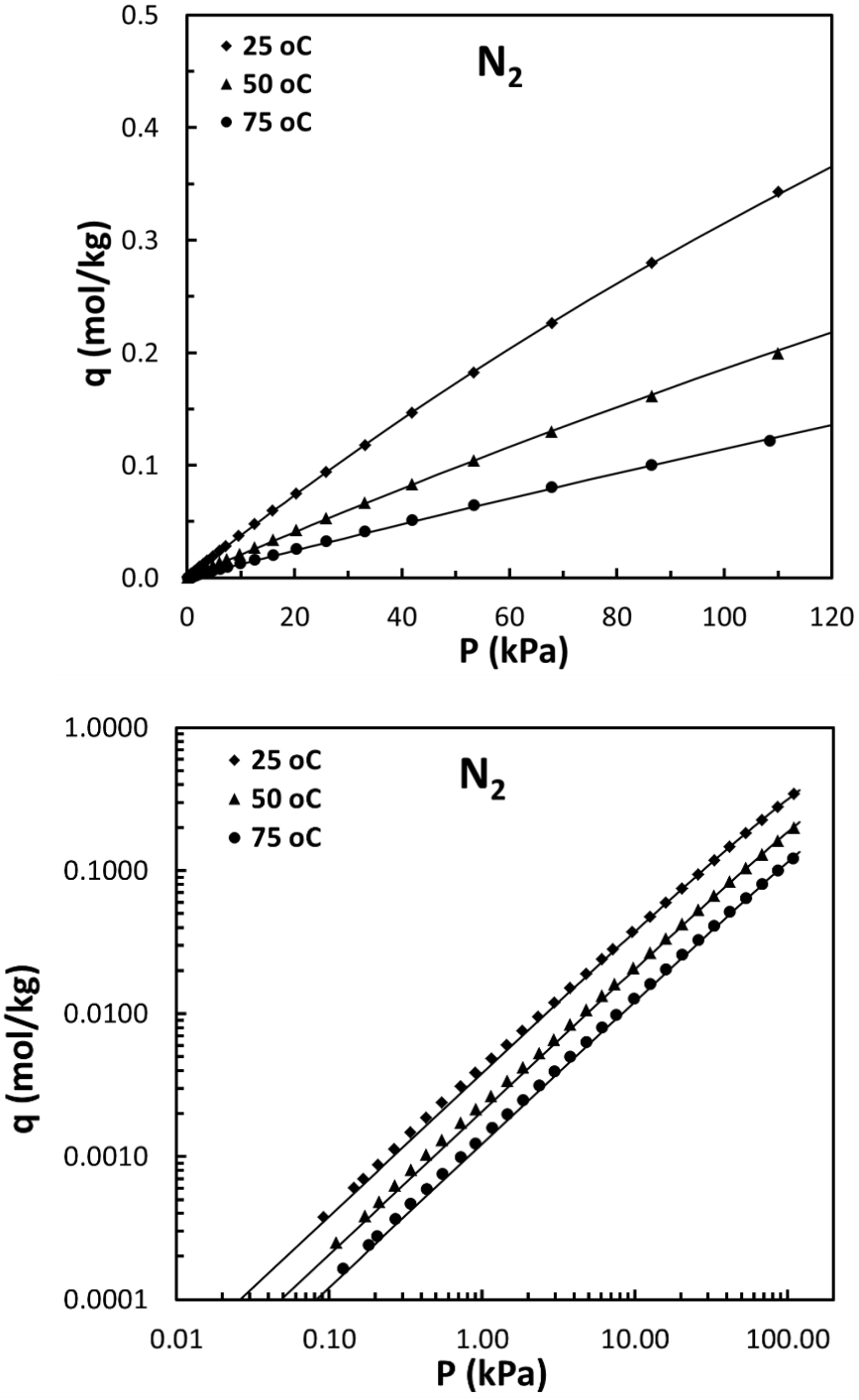

Figure 1.1 Adsorption equilibrium isotherms of Nitrogen fitted with TPL model at three different temperatures on 13X zeolite on rectangular coordinates (Top), and logarithmic scale (Bottom)

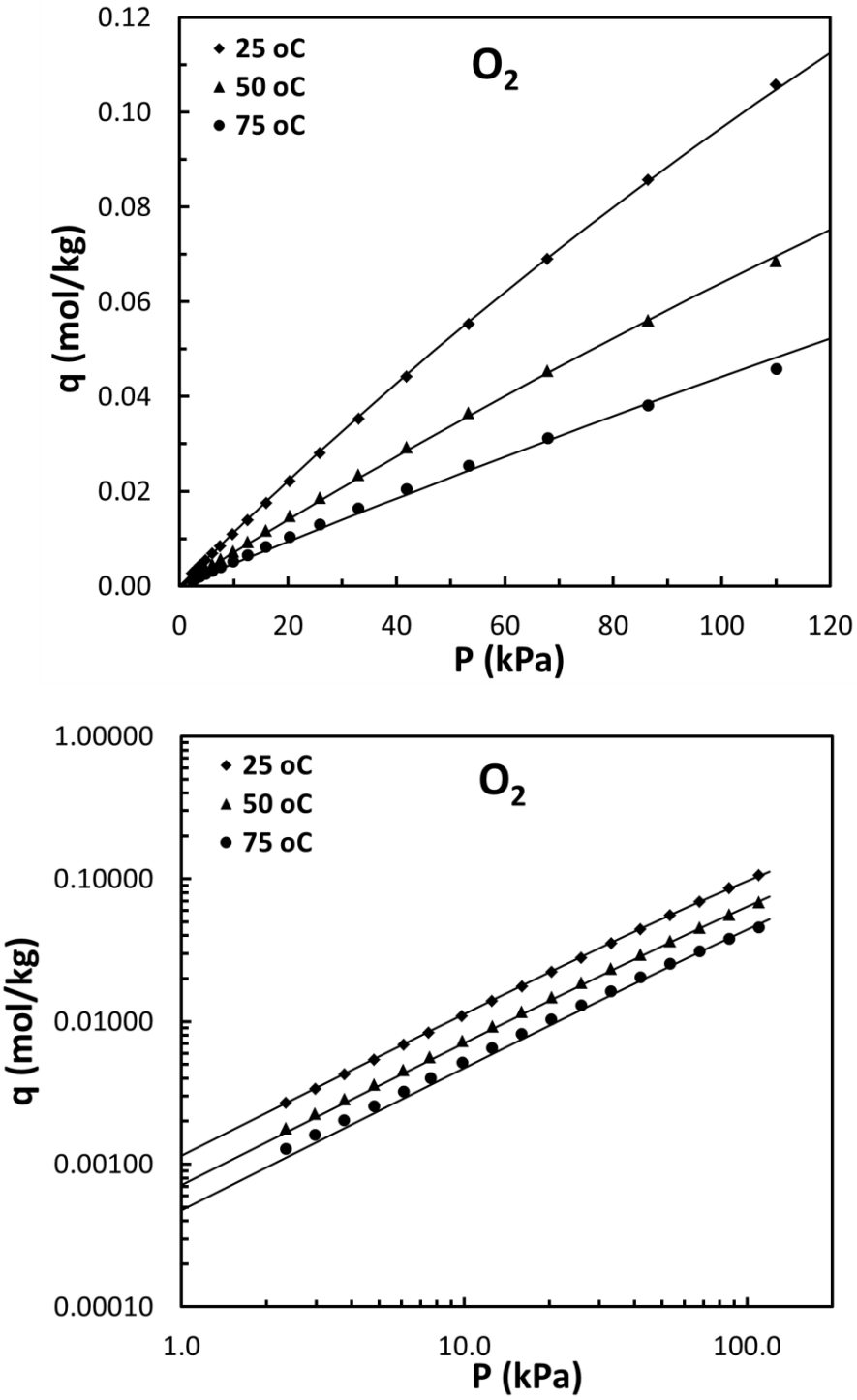

Figure 1.2 Adsorption equilibrium isotherms of Oxygen fitted with TPL model at three different temperatures on 13X zeolite on rectangular coordinates (Top), and logarithmic scale (Bottom)

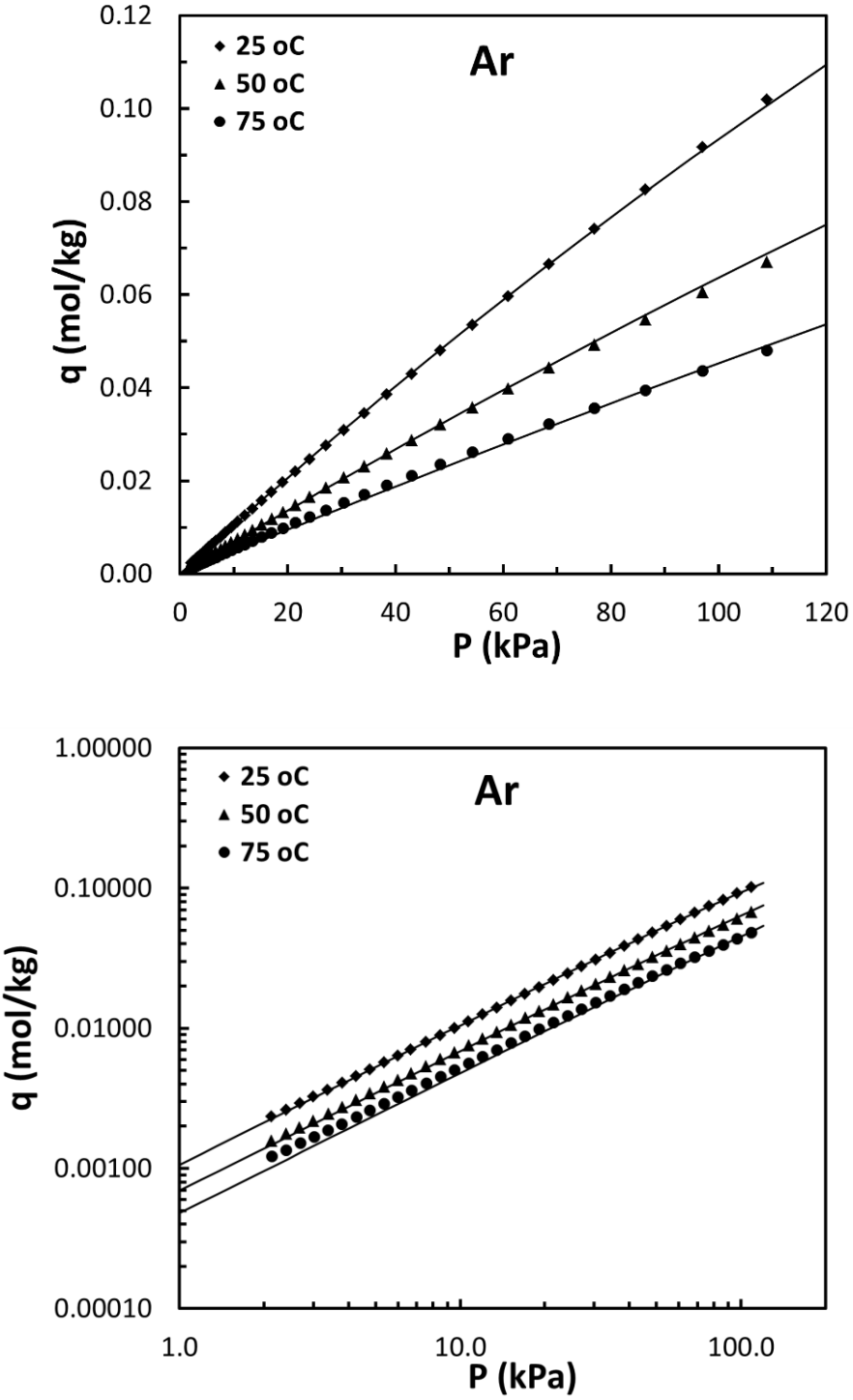

Figure 1.3 Adsorption equilibrium isotherms of Argon fitted with TPL model at three different temperatures on 13X zeolite on rectangular coordinates (Top), and logarithmic scale (Bottom)

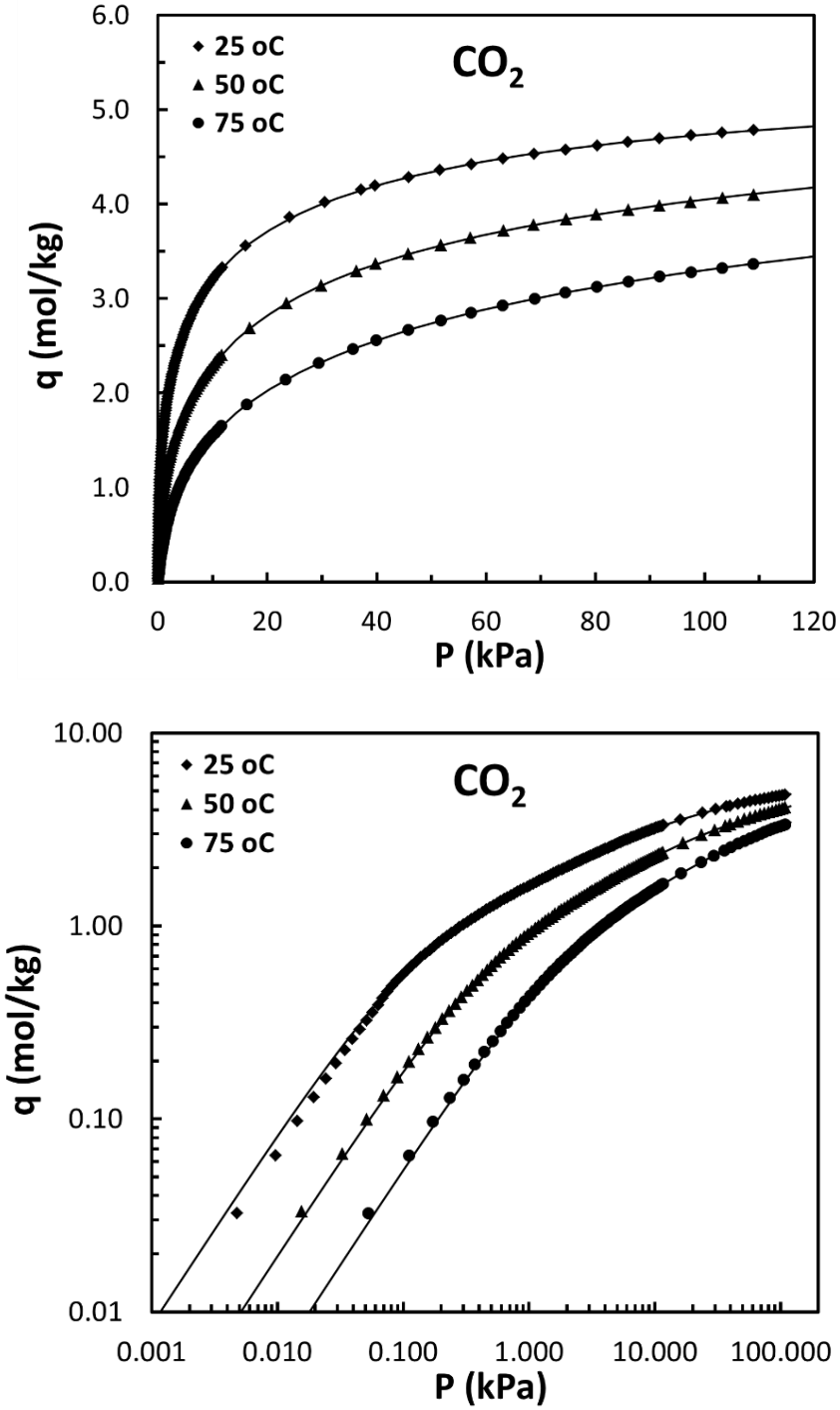

Figure 1.4 Adsorption equilibrium isotherms of Carbon dioxide fitted with TPL model at three different temperatures on 13X zeolite on rectangular coordinates (Top), and logarithmic scale (Bottom)

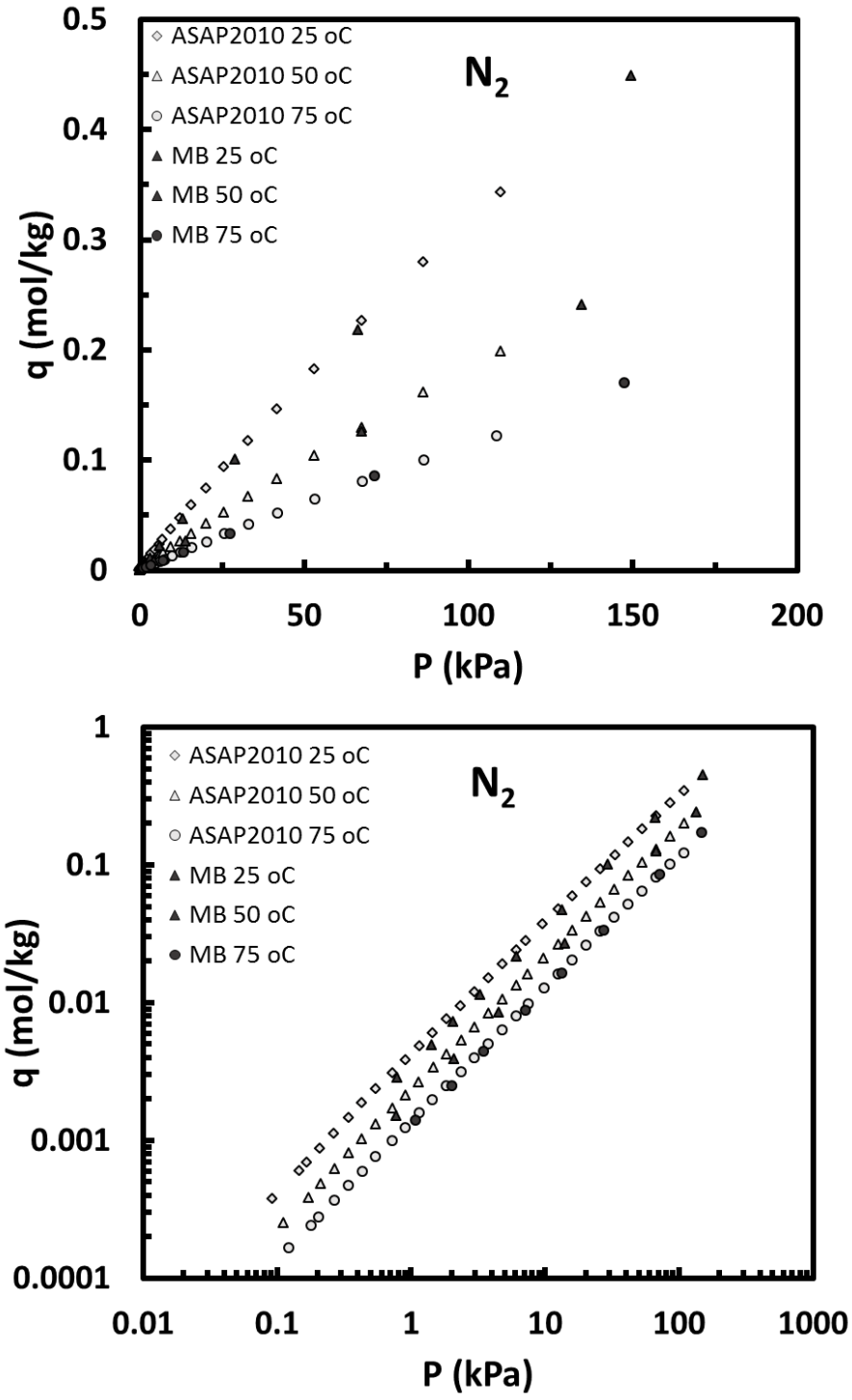

Figure 1.5 Adsorption equilibrium isotherms of Nitrogen at three different temperatures on 13X zeolite obtained by gravimetric and volumetric setups on rectangular coordinates (Top), and logarithmic scale (Bottom)

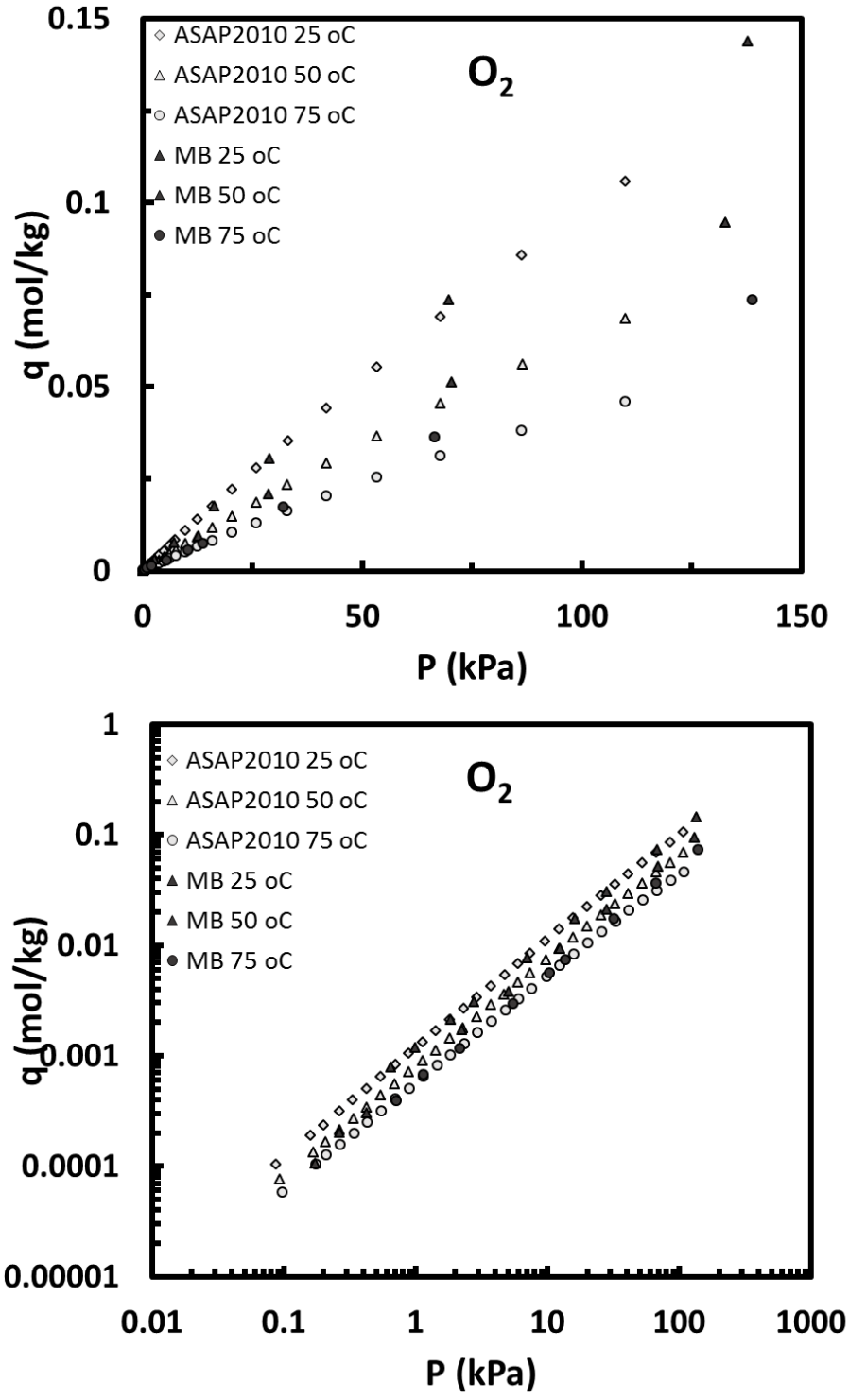

Figure 1.6 Adsorption equilibrium isotherms of Oxygen at three different temperatures on 13X zeolite obtained by gravimetric and volumetric setups on rectangular coordinates (Top), and logarithmic scale (Bottom)

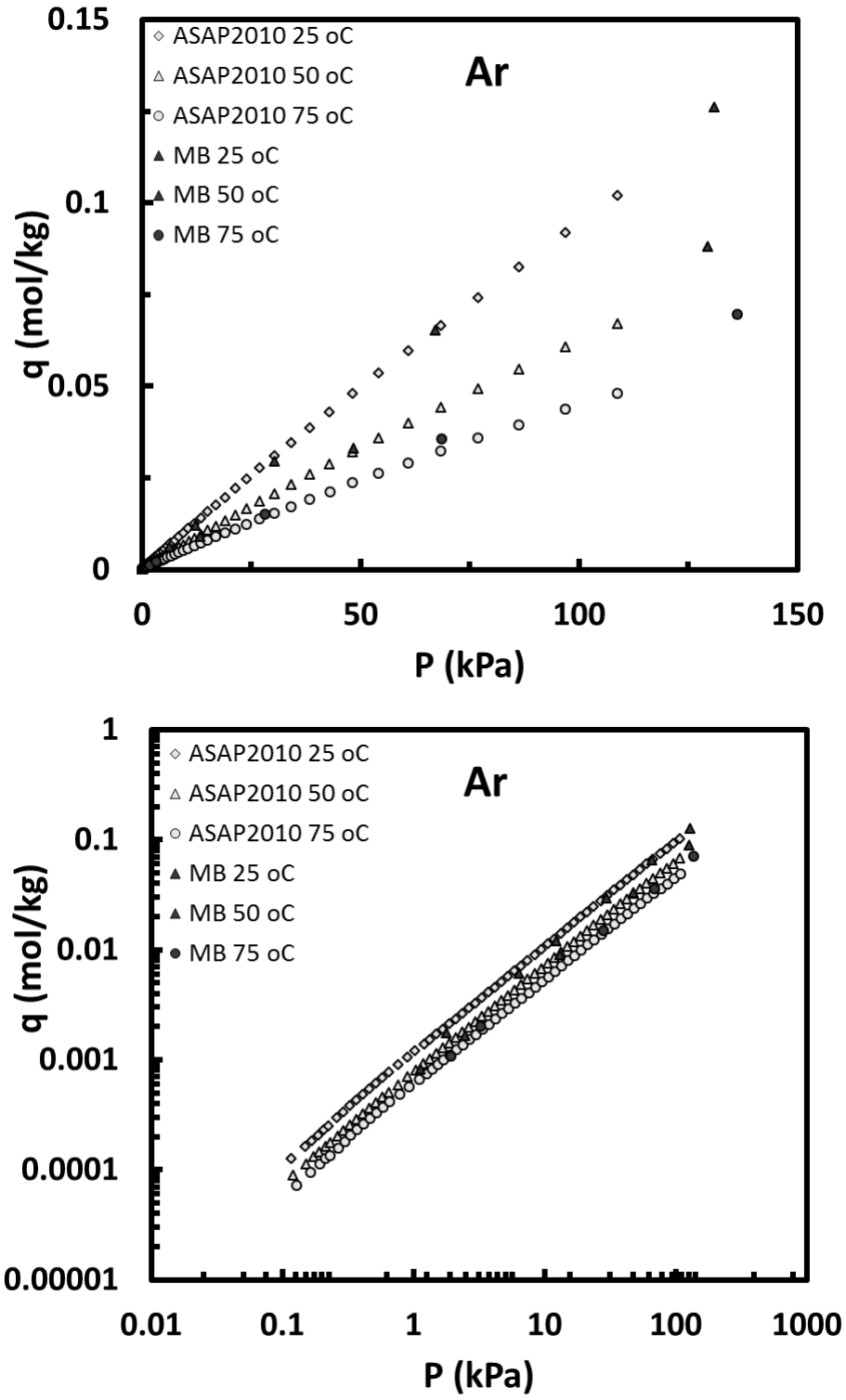

Figure 1.7 Adsorption equilibrium isotherms of Argon at three different temperatures on 13X zeolite obtained by gravimetric and volumetric setups on rectangular coordinates (Top), and logarithmic scale (Bottom)

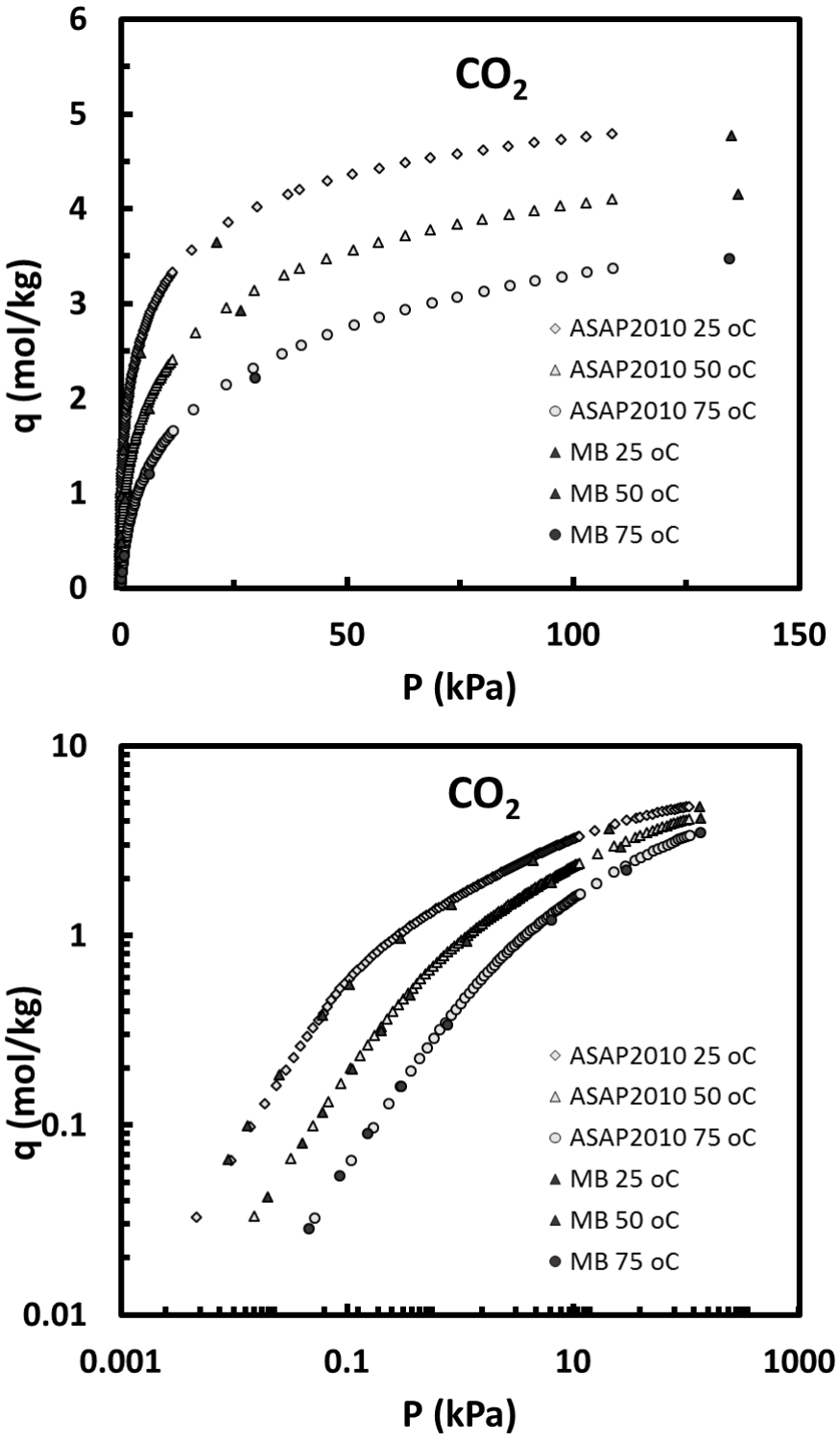

Figure 1.8 Adsorption equilibrium isotherms of Carbon dioxide at three different temperatures on 13X zeolite obtained by gravimetric and volumetric setups on rectangular coordinates (Top), and logarithmic scale (Bottom)

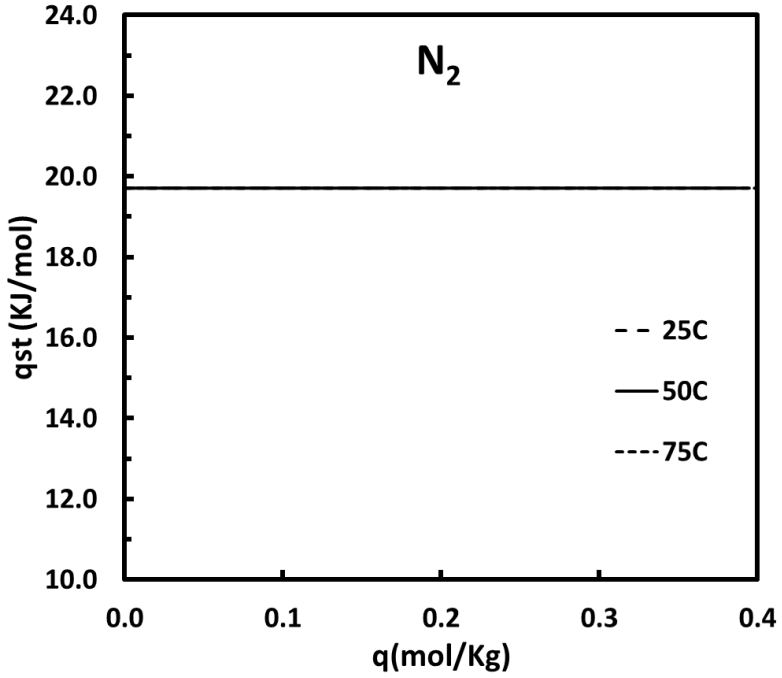

Figure 1.9. Isosteric heat of adsorption for N_2 with respect to loadings for three different temperatures (Isosteric heat of adsorption equation derived from TPL model)

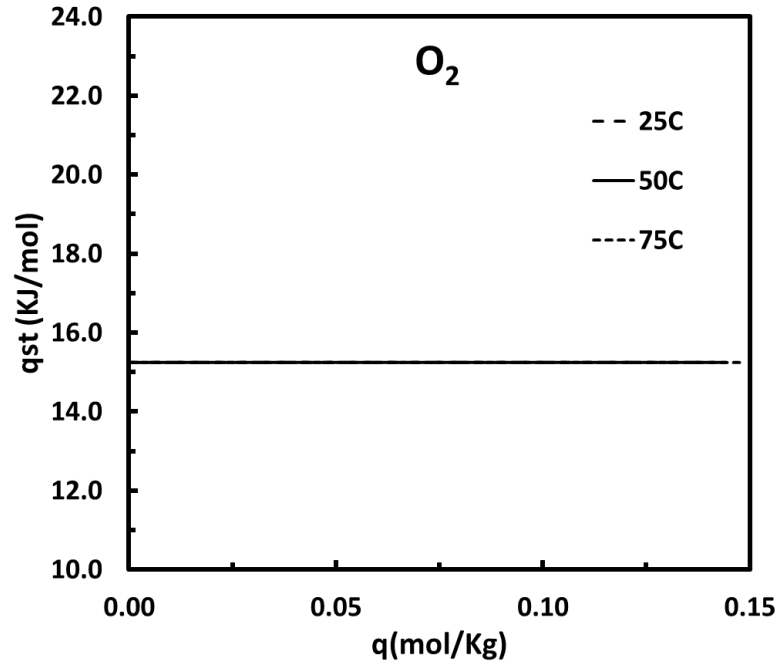

Figure 1.10 Isosteric heat of adsorption for O_2 with respect to loadings for three different temperatures (Isosteric heat of adsorption equation derived from TPL model)

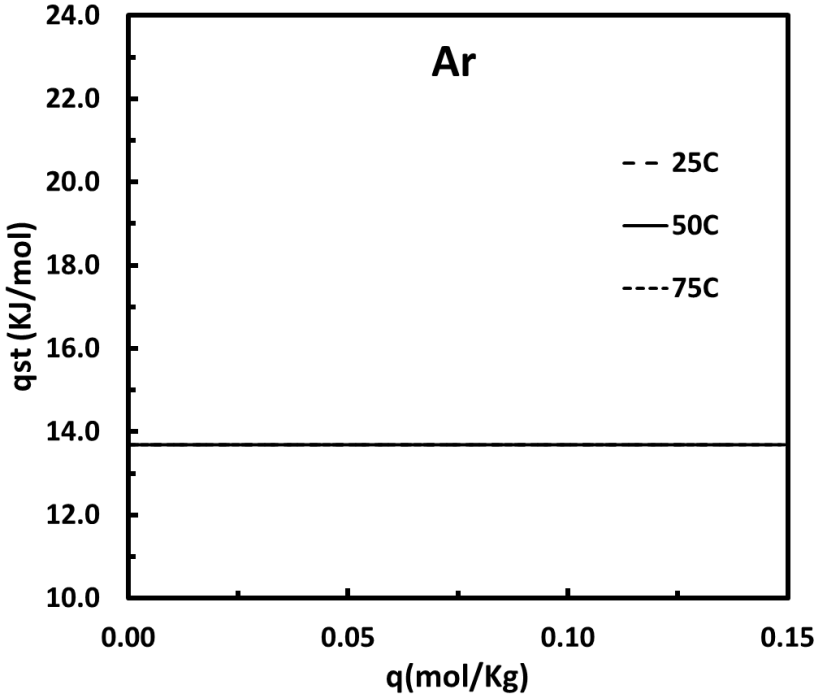

Figure 1.11 Isosteric heat of adsorption for Ar with respect to loadings for three different temperatures (Isosteric heat of adsorption equation derived from TPL model)

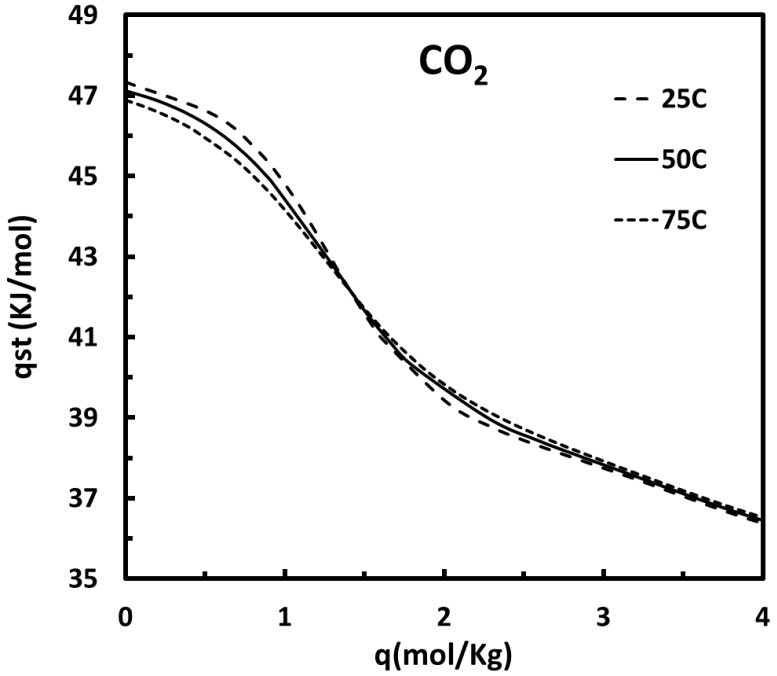

Figure 1.12 Isosteric heat of adsorption for CO_2 with respect to loadings for three different temperatures (Isosteric heat of adsorption equation derived from TPL model)

CHAPTER 2

UNDERSTANDING PARALLEL CHANNEL ADSORBENT STRUCTURES USING CFD MODELING

2.1 SUMMARY

A comprehensive 2-D mathematical model with minimum assumptions and simplifications was developed to study the fundamentals of adsorption processes in parallel channel structured adsorbent contactors. The resulting rigorous model, which includes mass, momentum and energy balances and appropriate boundary conditions was used to investigate the adsorption and desorption dynamics of CO_2 capture from flue gas (CO_2/ N_2 mixture) in a parallel passage adsorbent contactor covered with zeolite 13X under different conditions.

The behavior of the system in terms of break through curves, loading, pressure, velocity, concentration and temperature profiles needed to understand the fundamentals of the structured bed adsorbent contactor were studied.

The simulation results of adsorption within a parallel channel adsorbent structure clearly indicated that under studied circumstances the plug flow condition can be assumed and therefore the system is not subject to premature breakthrough. More importantly, the simulation results showed that the plug flow condition can be maintained even at very high velocities (e.g., $V_{z,o}$ = 10.0 m/s), far exceeding the velocity a particle, pellet or bead can withstand in a packed bed and at low mass transfer coefficients (K_{CO2} = 0.4 1/s) which are

anticipated to be much higher than pelleted systems due to decrease in particle size and macropore diffusion resistance.

Therefore, it was shown that under present conditions a parallel channel adsorbent structure can be modeled with comparatively simple 1-D models used for packed beds with significantly less computational effort compared to a full 2-D model.

2.2 INTRODUCTION

A randomly packed bed of adsorbent particles is the traditional mass transfer device for adsorption processes. Packed beds are cheap and versatile, but, in terms of the tradeoff between mass transfer resistance and pressure drop, it is rather inefficient. Such considerations become important when flow rates are high and the 'added value' of the process is low (e.g. CO_2 capture, desiccant cooling and VOC removal applications) **[17]**. Although the manufacturing cost of structured adsorbents is higher, from simple theoretical considerations it can be shown that a structured contactor in which the gas passes in laminar flow through channels covered with adsorbent shows a significant improvement in the mass transfer/pressure drop characteristics in comparison with a traditional packed bed.

Recently, there has been significant interest in the intensification of separation processes. In processes with cyclic nature such as PSA, VSA, and TSA (pressure, vacuum and temperature- swing adsorption, respectively) the primary way of increasing production from a given amount of adsorbent is by reducing the cycle time. However, reducing the cycle time as mentioned before usually leads to problems such as decreased working capacity per cycle for the component of interest, decreasing the product recovery and increasing the pressure drop. The extent to which the cycle time reduces the working capacity and recovery and increases the pressure drop is dependent on the structure of the

adsorbent **[18]**. Parallel channel monolithic structures with controllable shape, cell density and wall thickness have been reported for their use in adsorptive gas-separation systems **[19, 20, 21, 22, 23-26].** The primary advantage of these configurations is their lower pressure drop and higher mass-transfer rates.

In most, if not all, commercial PSA processes the rate of adsorption into and desorption out of the adsorbent particle, bead or pellet is limited by macropore diffusion. Clearly, any reduction in the size of the adsorbent particle would result in faster mass transfer, thereby providing better bed regeneration and better working capacity of the more strongly adsorbed (heavy) component(s). Faster mass transfer rates or kinetics would improve the PSA process performance in terms of the purity and recovery of the desired component(s) and it would increase the feed throughput. Equivalently, faster kinetics would allow for the possibility of designing new PSA processes with shorter cycle times and higher feed throughputs or productivities with reduced bed sizes and thus capital costs. As trivial as this may seem, it is not possible to simply reduce the size of a commercial adsorbent particle, pellet or bead in a large scale PSA process. Doing so would have two major consequences. First, the higher pressure drop would diminish the separation performance possibly counteracting any benefit of the improved kinetics, and second, the smaller particles would be subjected to inertial conditions (gas phase velocities) that might cause bed fluidization and particle attrition. In other words, to significantly improve the productivity of a large scale PSA process by decreasing the cycle time and reducing the bed size, it is not feasible to use a randomly packed bed of adsorbent particles, pellets or beads. However, it might be feasible to use a parallel channel adsorbent structure, as

recently demonstrated by the QuestAir rapid PSA system. Not only are pressure drop and attrition issues eliminated, but also the mass transfer rates can be exceedingly high.

Rutheven and Thaeron [17] in an experimental and theoretical study derived and verified an expression for the HETP (height equivalent to a theoretical plate) for a parallel passage contactor, analogous to the van Deemter equation for the packed bed. For the adsorption of several light gases from a helium carrier in an adsorber consisting of parallel sheets of activated carbon fiber adsorbent they confirmed that such a parallel-sided duct coated with ACF sheets would be well suited to a dual piston rapid pressure swing adsorption system for large throughput and low value added applications such as CO_2 removal from stack gas.

Farooq et al.[27] developed a theoretical one dimensional model to simulate the operation of a dual-piston pressure swing adsorption (PSA) system. They assumed negligible frictional pressure drop, linear or single process Langmuir isotherm and isothermal condition. The predictions of the simulation were compared with experimental results. The model provides a good qualitative prediction of the system behavior, although the experimental pressure profiles are generally somewhat attenuated relative to the predicted profiles.

Ahn and Brandani [28] studied separation performance of individual rectangular channels for development of small-scale analytical devices. The breakthrough dynamics in a rectangular channel of arbitrary aspect ratio were investigated and a new simple analytical equation is proposed for the prediction of the HETP of a chromatographic column, which has been validated against a 3-D isothermal numerical model.

In a review paper **Rezaei and Webley [29]**, discussed the use of different adsorbent structures with improved performance as a competitive alternate to conventional packed beds of pellets/beads. General requirements were elucidated and illustrated with respect to specific structures such as monoliths, foams, laminates, and fabric structures and geometrical parameters of adsorbents which affect the system performance were identified and discussed. They concluded that improvement and optimization of adsorptive gas separation processes clearly includes the development of improved structured adsorbents and that these novel structures can fulfill many of the requirements of advanced gas separation processes such as enhanced mass transfer, reduced pressure drop, and improved thermal management.

2.3 MATHEMATICAL MODEL

The system that was studied in this work is a 2D parallel channel adsorbent contactor. This configuration consists of two infinite parallel plates covered with a layer of adsorbent on the inner surface of the plates. Since the system is symmetrical around the centerline calculations can be reduced to half, **Figure 2.1** shows a schematic of such a half cell.

The differential and algebraic equations, along with the assumptions made in writing the individual equations, describing parallel channel adsorption system, are detailed below. The following assumptions are imposed: the ideal gas law, Newtonian fluid and the mass transfer between solid and gas defined by the linear driving force (LDF) approach.

In order to be consistent, all equations have been considered in mass base form using mass average velocities.

Mass Balance Equations

For an N-component, 2D and compressible system, the overall and component mass balances over a differential volume element respectively yield (**Figure 2.1**):

$$\frac{\partial \rho}{\partial t} + \frac{\partial \rho V_X}{\partial x} + \frac{\partial \rho V_Z}{\partial z} = 0 \qquad (1)$$

$$\rho \frac{\partial \omega_i}{\partial t} + \rho V_x \frac{\partial \omega_i}{\partial x} + \rho V_z \frac{\partial \omega_i}{\partial z} - D_x \frac{\partial}{\partial x}\left(\rho \frac{\partial \omega_i}{\partial x}\right) - D_z \frac{\partial}{\partial z}\left(\rho \frac{\partial \omega_i}{\partial z}\right) = 0 \qquad i = 1 \; to \; N-1 \; (2a)$$

$$\omega_N = 1 - \sum_{i=1}^{N-1} \omega_i \qquad (2b)$$

With

$$\rho = \frac{PM}{RT};\; M = \sum_{i=1}^{N} y_i M_i;\; y_i = \frac{\frac{\omega_i}{M_i}}{\sum_{j=1}^{N} \frac{\omega_j}{M_j}}$$

where ρ is the density of gas mixture, V_x and V_Z are the mass averaged velocities of the gas phase, ω_i is the mass fraction of species i in the gas phase, D_x and D_z are respectively diffusion coefficients of species i in x and z directions, P is pressure, T is temperature, M is gas phase average molecular weight, M_i and y_i are the molecular weight and the mole fraction of species i.

Boundary Conditions

Boundary condition at the interface of adsorbent and gas is obtained from writing component mass balance on the adsorbent layer.

At x = δ (gas-solid interface)

$$\rho\omega_i v_x - D_x \rho v_x \frac{\partial \omega_i}{\partial x} = m' M_i k_i (q_i^* - q_i) + \frac{\varepsilon m'}{\rho_a} \frac{\partial \rho \omega_i}{\partial t} \qquad i = 1 \; to \; N \qquad (3a)$$

At x = 0 (symmetry line)

$$\frac{\partial \omega_i}{\partial x} = 0 \qquad i = 1 \; to \; N \qquad (3b)$$

At z = 0 (inlet)

$$\omega_i = \omega_{f,i} \qquad i = 1 \; to \; N \qquad (3c)$$

At z = L (outlet)

$$\frac{\partial \omega_i}{\partial z} = 0 \qquad i = 1 \; to \; N \qquad (3d)$$

Where m' is the mass of adsorbent per unit area of the gas-solid interface in one layer, k_i is the mass transfer coefficient for species i, ε and ρ_a are the porosity and density of the adsorbent respectively. $\omega_{i,f}$ is the mass fraction of species i in feed. q_i^* is the equilibrium loading of the adsorbent while q_i shows the instantaneous loading of the adsorbent and is obtained by solving the linear driving force (LDF) equation that represents the mass transfer of species *i* between the solid and gas phase:

$$\frac{\partial q_i}{\partial t} = k_i (q_i^* - q_i) \qquad i = 1 \; to \; N \qquad (4)$$

The equilibrium loading of component *i*, q_i^* is calculated from the three process Langmuir isotherm in perfect positive mode ($b_{1,i} > b_{2,i} > b_{3,i}$ for $i = 1 \; to \; N$):

$$q_i^* = q_{1,i}^s \frac{b_{1,i} P y_i}{\left[1 + \sum_{j=1}^{N} b_{1,j} P y_j\right]} + q_{2,i}^s \frac{b_{2,i} P y_i}{\left[1 + \sum_{j=1}^{N} b_{2,j} P y_j\right]} + q_{3,i}^s \frac{b_{3,i} P y_i}{\left[1 + \sum_{j=1}^{N} b_{3,j} P y_j\right]} \quad i = 1 \; to \; N \qquad (5)$$

Where the temperature dependence of parameters $b_{1,i}$,$b_{2,i}$ and $b_{3,i}$ in the TPL isotherm can be expressed by equation 6.

$$b_{m,i} = b_{m,i}^{0} exp\left(\frac{B_{m,i}}{T}\right) \qquad i = 1\ to\ N \text{ and m = 1 to 3} \qquad (6)$$

Momentum Balances

Equations 7 and 8 show the momentum balance equations for a Newtonian compressible fluid in a 2-D system.

X direction:

$$\rho\left[\frac{\partial V_x}{\partial t} + V_x\frac{\partial V_x}{\partial x} + V_z\frac{\partial V_x}{\partial z}\right] = \rho g_x - \frac{\partial P}{\partial x} + \mu\left[\left(\frac{\partial^2 V_x}{\partial x^2} + \frac{\partial^2 V_x}{\partial z^2}\right) + \frac{1}{3}\left(\frac{\partial^2 V_x}{\partial x^2} + \frac{\partial^2 V_z}{\partial x \partial z}\right)\right] \quad (7)$$

Z direction:

$$\rho\left[\frac{\partial V_z}{\partial t} + V_x\frac{\partial V_z}{\partial x} + V_z\frac{\partial V_z}{\partial z}\right] = \rho g_z - \frac{\partial P}{\partial z} + \mu\left[\left(\frac{\partial^2 V_z}{\partial x^2} + \frac{\partial^2 V_z}{\partial z^2}\right) + \frac{1}{3}\left(\frac{\partial^2 V_z}{\partial z^2} + \frac{\partial^2 V_x}{\partial z \partial x}\right)\right] \quad (8)$$

Where μ is the viscosity of the gas mixture, which for simplicity is assumed to be a fixed and arbitrary value, and g_x and g_z are the components of gravitational acceleration in x and z directions respectively.

Boundary Conditions

Boundary condition for velocity at x direction at the interface of adsorbent and gas is derived from writing the overall mass balance on the adsorbent layer and for velocity at z direction, no slip condition is used. For inlet, laminar flow profile is set as boundary condition and pressure is fixed at the exit end of the channel.

At x = δ (gas-solid interface)

$$\rho v_x = m' \sum_{j=1}^{N} M_j \, k_j \left(q_j^* - q_j\right) + \frac{\varepsilon m'}{\rho_a} \frac{\partial \rho}{\partial t} \tag{9a}$$

$$V_Z = 0$$

At x = 0 (symmetry line)

$$\frac{\partial V_x}{\partial x} = 0, \frac{\partial V_z}{\partial x} = 0, \frac{\partial P}{\partial x} = 0 \tag{9b}$$

At z = 0 (inlet)

$$V_x = 0 \tag{9c}$$

$$V_z = V_{max}\left(1 - \left(\frac{x}{\delta}\right)^2\right)$$

At z = L (outlet)

$$\frac{\partial V_x}{\partial z} = 0, \ \frac{\partial V_z}{\partial z} = 0, \ P = P_0 \tag{9d}$$

Energy Balance

Energy balance for a compressible fluid at low Mach numbers is expressed as :

$$\rho C_p \left(\frac{\partial T}{\partial t} + V_x \frac{\partial T}{\partial x} + V_z \frac{\partial T}{\partial z}\right) = K_x \frac{\partial^2 T}{\partial x^2} + K_z \frac{\partial^2 T}{\partial z^2} + \frac{\partial P}{\partial t} \tag{10}$$

With

$$Cp = \sum_{j=1}^{n} \left(y_j Cp_j\right) \tag{11}$$

Where K_x and K_z are the thermal conductivity of the gas in x and z directions, C_{pj} and C_p are the molar heat capacities of species *i* and gas mixture respectively.

Boundary Conditions

By writing the energy balance on adsorbent layer, the boundary condition for temperature on the gas/solid interface is derived.

At x = δ (gas-solid interface)

$$\rho_a \sum \left(\Delta H_i \frac{\partial q_i}{\partial t} + q_i C_{p,i,a} \frac{\partial T}{\partial t} \right) + \rho_a C_{p,a} \frac{\partial T}{\partial t} + \rho_m C_{p,m} \frac{\delta_m}{\delta} \frac{\partial T}{\partial t} + \varepsilon \left(C_T C_p \frac{\partial T}{\partial t} - \frac{\partial P}{\partial t} \right) =$$

$$K_{eff} \frac{\partial^2 T}{\partial z^2} - \frac{K_x}{\delta_a} \frac{\partial T}{\partial x} \quad (12a)$$

At x = 0 (symmetry line)

$$\frac{\partial T}{\partial x} = 0 \quad (12b)$$

At z = 0 (inlet)

$$T = T_f \quad (12c)$$

At z = L (outlet)

$$\frac{\partial T}{\partial z} = 0 \quad (12d)$$

Where ρ_a and ρ_m are the density of the adsorbed layer and the metal wall respectively, ΔH_i is the heat of adsorption of species i, $C_{p,i,a}$, $C_{p,a}$ and $C_{p,m}$ are the molar heat capacity of species i in the adsorbed phase, molar heat capacity of the adsorbent layer and the metal wall respectively. δ_a and δ_m are the thickness of adsorbent layer and wall respectively and C_T is the molar concentration of gas inside the adsorbent layer .K_{eff} is the effective thermal conductivity of wall and adsorbent layer together in z direction.

The equations described above constitute a complete mathematical model for multi-component adsorption process in a parallel passage adsorbent contactor, once the initial conditions are specified. For a system containing N components, there are a total of 2N+4 variables (i.e. N mole fractions, N loadings, pressure, temperature and 2 velocity components) and equations that have to be solved at each node.

As mentioned before in this work the developed model is used to study the dried binary flue gas mixture typical to coal fired power plants. Initial conditions for CO_2- N_2 flue gas mixture simulations are summarized in **Table 2.1.**

Solving the derived set of equations was carried out using COMSOL Multiphysics 4.3b that uses the finite element analysis.

2.4 CHANNEL AND ADSORBENT CHARACTERISTICS

An overview of the parallel passage channel, adsorbent and process characteristics used as input parameters in the simulations is presented in **Table 2.2** Gas phase species and adsorbent transport and thermodynamic properties are summarized in **Table 2.3.** The adsorbent used is a commercial 13X molecular sieve zeolite (Grade 544 10A 8*12), produced by Grace Davison chemical and material company.

Equilibrium adsorption isotherm parameters for CO_2 and N_2 were obtained by fitting Three Process Langmuir isotherm to experimental data, obtained by an in house volumetric system (ASAP2010) modified to particularly measure the adsorption isotherms in low and medium pressure ranges with high accuracy. The resulting equilibrium adsorption isotherms and experimental data for CO_2 and N_2 are shown in **Figure 2.2** and **Figure 2.3** respectively for three different temperatures.

2.5 RESULTS AND DISCUSSION

In the simulations the varied conditions include CO_2 mass transfer coefficients and feed velocity. Also the system have been studied isothermally and non-isothermally in order to investigate the effects of heat of adsorption on the process.

Unlike conventional packed bed adsorbent columns in channel adsorbents the adsorbent particles are not directly in front of the flow and there is an open space for the gas flow to pass, therefore main concern in the monolith adsorbent contactors is to ensure the near plug flow conditions for concentration and prevent fast breakthrough of the heavy gas. In order for this to happen, diffusion of the adsorbate towards channel walls caused by

adsorption on the adsorbent layer should be dominant in comparison with the convection of the heavy gas along the channel. In all the simulations N_2 mass transfer coefficient and outlet pressure are set to 1.0 1/s and 120 KPa respectively. In isothermal study the bed is assumed to be uniformly at 75 degree Celcius.

Figure 2.4 shows the CO_2 breakthrough curves at z=1 m for 3 different CO_2 mass transfer coefficients (10, 1 and 0.4 s^{-1}) at the midway point between the plates in an isothermal condition. V_{avg} which its value is half of the V_{max} , defines the initial and inlet laminar parabolic velocity field is set to 4.715 m/s. Coefficients are chosen in a way that shows the effect of mass transfer coefficient change while remaining close to the actual values.

As shown in the figure, mass transfer coefficient has a considerable effect on the breakthrough curve. In high mass transfer coefficients concentration profile in the channel is almost flat and breakthrough has an almost vertical shape which means that the adsorbent in contact with gas reaches equilibrium loadings very fast and become saturated but as mass transfer coefficient is decreased, adsorbents approach to equilibrium loadings becomes slower and a longer portion of the bed length is required to fully adsorb the heavy gas therefore concentration profile deviates from vertical form which leads to earlier and wider breakthrough curve.

With no adsorption heavy gas should break through in a fraction of a second and the breakthrough time between 25 and 35 seconds confirms that the adsorption is the dominant phenomena. The gas has the highest velocity and concentration on the midway point therefore investigating the worst case gives us confidence that breakthrough will happen later in other points along the bed exit but in order to determine if the system

satisfies the near plug flow condition, breakthrough curves other than the ones at the midway point between the plates are required.

Figure 2.5 shows breakthrough curves of the gas phase concentration at z = 1 m evaluated at the midway point between the plates and 10 microns away from one of the plates for three different LDF mass transfer coefficients of CO_2 for V_{avg} = 4.715 m/s and isothermal condition. It is clear from these simulations that despite the parabolic flow, gas phase diffusion of CO_2 to the wall and then into the adsorbent is fast enough in the relatively small channel (298 micron) to maintain a plug flow condition. This is realized by the breakthrough curves at the two different points being barely different and their center of gravity (point of intersection) remaining very close.

Figure 2.6 illustrates the Effect of feed velocity on the break through curve for 3 different CO_2 mass transfer coefficients in isothermal condition. New simulations were carried out with V_{avg} = 10.0 m/s. As shown in the figure, feed velocity doesn't affect the shape of the curve and it only decreases the breakthrough time. This means that still diffusion in x direction is the dominant and faster mechanism compared to the convection in z direction even at higher velocities and lower mass transfer coefficients.

Similar to **Figure 2.5**, breakthrough curves of the gas phase concentration at z = 1 m evaluated at the midway point between the plates and 10 microns away from one of the plates for three different LDF mass transfer coefficients of CO_2 for V_{avg} = 10.0 m/s and isothermal condition are shown in **Figure 2.7**. With the same argument it is concluded that even with more than twice the value of velocity, plug flow condition is maintained. It also can be seen that the difference between breakthrough curves of two points in V_{avg} = 10.0 m/s is similar to V_{avg} = 4.715 m/s which indicates that the concentration front at each z is

determined by mass transfer properties of the system and in this range is independent of the velocity.

Figure 2.8 shows CO_2 mole fraction at midway point, CO_2 loading and N_2 loading profiles along the bed at 4 different times for V_{avg} = 4.715 m/s, K_{CO2} = 1.0 1/s and isothermal condition. **Figure 2.9** presents the velocity and pressure profiles at midway points for the same condition. As previous discussions anticipate, the loading profiles totally follow the mole fraction profiles which again confirm the fast and dominant diffusion and adsorption mechanism. Small decrease in maximum amount of loading as we proceed along the bed is related to pressure drop and therefore lower adsorption capacity.

Figure 2.10 shows the CO_2 concentration and velocity profiles in the axial direction at different times along a line perpendicular to the two planes from the midway point to the wall at an axial location z/L = 0.1 (i.e., 10% into the channel). The same LDF mass transfer coefficients as in **Figure 2.5** were used. These results confirm the results in **Figure 2.5**. Even though the velocities in the axial direction exhibit a parabolic profile, the CO_2 profiles are nearly horizontal with only a slight deviation from plug flow for the largest LDF mass transfer coefficient (10 s^{-1}). As time progresses, more CO_2 is taken up by the adsorbent at this axial location in the channel. Eventually the first 10% of the channel is in equilibrium with the feed concentrations of CO_2 and N_2, adsorption stops there and the local velocity increases to the feed values. Of course, past this axial location the CO_2 wave front continues to progress down the channel and eventually exits the channel as shown in **Figure 2.5**, as the entire channel begins to equilibrate with the feed. At the end of breakthrough, the entire channel is in equilibrium with the feed at 75 ^oC.

Heat effects are of considerable importance in adsorption processes especially when the interaction between gas and solid is strong, which leads to high heats of adsorption.

In **Figure 2.11** isothermal breakthrough curve is compared with the breakthrough curve when the energy balance equation is also included in the model for Vavg = 4.715 m/s and KCO_2= 10 1/s.as shown heat of adsorption has a significant effect on the breakthrough curve and leads to an earlier and a two stage breakthrough curve.

This can be explained by **Figure 2.12** that presents temperature and loading profiles on the adsorbent layer and mole fraction profiles on the midway line along the bed at 3 different times (i.e. 1 s, 5 s and 20 s) for Vavg = 4.715 m/s and KCO_2 = 10.0 1/s.

As seen in **Figure 2.12a** in the mass transfer zone, adsorption of CO_2 causes temperature rise, as we move forward in time the mass transfer zone moves towards the end of the channel so the temperature front also moves forward, on the other side of the temperature front closer to the channel entrance because the channel is considered adiabatic only fresh feed with lower temperature cools down the hot adsorbent layer. In this case the rate of heat generation is more than cooling so temperature profiles become wider as time goes by.

Equilibrium loading of CO_2 is a strong function of temperature so as seen in **Figure 2.12b** loading profile reversely follows the temperature profiles and the adsorbent has lower loadings in higher temperatures and finally lower loadings mean less adsorption of the heavy gas and higher concentrations in gas phase as shown in **Figure 2.12c**.

Figure 2.13 shows breakthrough curves of the gas phase concentration at z = 1 m evaluated at the midway point between the plates and 10 microns away from one of the plates for K_{CO2} = 10 1/s, V_{avg} = 4.715 m/s and non-isothermal condition. Two curves almost

overlap and as discussed before in **Figure 2.5,** this indicates that the plug flow condition is also satisfied in the non-isothermal system.

2.6 CONCLUSION

These results show very clearly that plug flow conditions can be reasonably assumed when simulating adsorption dynamics within a parallel channel adsorbent structure and therefore the system is not subject to premature breakthrough. More importantly, results indicate that this assumption can be maintained even at very high velocities (e.g., $V_{z,o}$ = 10.0 m/s), far exceeding the velocity a particle, pellet or bead can withstand in a packed bed and low mass transfer coefficients (K_{CO2} = 0.4 1/s) which are expected to be much higher than pelleted systems due to decrease in particle size and macropore diffusion resistance. Hence, conditions exist in which a parallel channel adsorbent structure can be modeled with relatively simple 1-D plug flow models developed for packed beds that have significantly less computational demand compared to implementing a computationally prohibitive full 2-D model. However the momentum balance in packed bed simulators needs to be modified to predict the pressure drop through a parallel channel adsorbent structure, this will be the subject of future studies.

2.7 TABLES

Table 2.1 Initial conditions for CO_2 capture from the flue gas simulations

Variable	P[KPa]	T[K]	V_x[m/s]	V_z[m/s]	y_{CO2}	y_{N2}	q_{CO2}	q_{N2}
Initial Value	120	348.15	0	Vmax*(1-(z/δ)^2)	0	1	0	TPL

Table 2.2 Properties of the Channel, adsorbent, wall and process

Channel Characteristics	
Channel width (m)	298e-6
Channel length (m)	1.00
Adsorbent characteristics	
Adsorbent	13X
Adsorbent layer thickness (m)	100E-6
Adsorbent density (kg/m^3)	1093.0
Adsorbent layer porosity	0.54
Adsorbent layer heat capacity (J/kg/K)	1100.0
Adsorbent layer conductivity(W/m/K)	0.157
Adsorbent mass per unit area(kg/ m^2)	0.1093
Wall characteristics	
Wall thickness (m)	25.0E-6
Wall conductivity(W/m/K)	205.0
Wall mass per unit area(kg/ m^2)	0.0675
Wall heat capacity (J/kg/K)	897.0
Process characteristics	
Feed mole fraction: CO_2, N_2	0.1592, 0.8408
Feed temperature (K)`	348.15
Outlet pressure (kPa)	120.0

Table 2.3 Adsorbent and gas phase species thermodynamic and transport properties

Equilibrium and kinetic information	
$B_{1,i}$ for CO_2 and N_2 (K)	5757.03, 2370.32
$B_{2,i}$ for CO_2 and N_2 (K)	4606.08, 2370.32
$B_{3,i}$ for CO_2 and N_2 (K)	4224.86, 2370.32
$b^0_{1,i}$ for CO_2 and N_2 (Pa^{-1})	2.4419e-11, 7.5950e-10
$b^0_{2,i}$ for CO_2 and N_2 (Pa^{-1})	4.5204e-11, 7.5950e-10
$b^0_{3,i}$ for CO_2 and N_2 (Pa^{-1})	1.3737e-11, 7.5950e-10
$q^s_{1,i}$ for CO_2 and N_2 (mol/kg)	1.512, 0.495
$q^s_{2,i}$ for CO_2 and N_2 (mol/kg)	2.530, 0.829
$q^s_{3,i}$ for CO_2 and N_2 (mol/kg)	2.095, 0.686
μ (Pa.s)	1.78e-5
D_x and D_z (m^2/s)	1.67e-5, 1.67e-5
K_x and K_z (W/m/K)	0.026, 0.026
ΔH_i for CO_2 and N_2 (J/mol)	-39576.54, -19544.66
Cp_i for CO_2 and N_2 (J/mol/K)	39.38, 14.57
$Cp_{i,a}$ for CO_2 and N_2 (J/mol/K)	39.38, 14.57

2.8 FIGURES

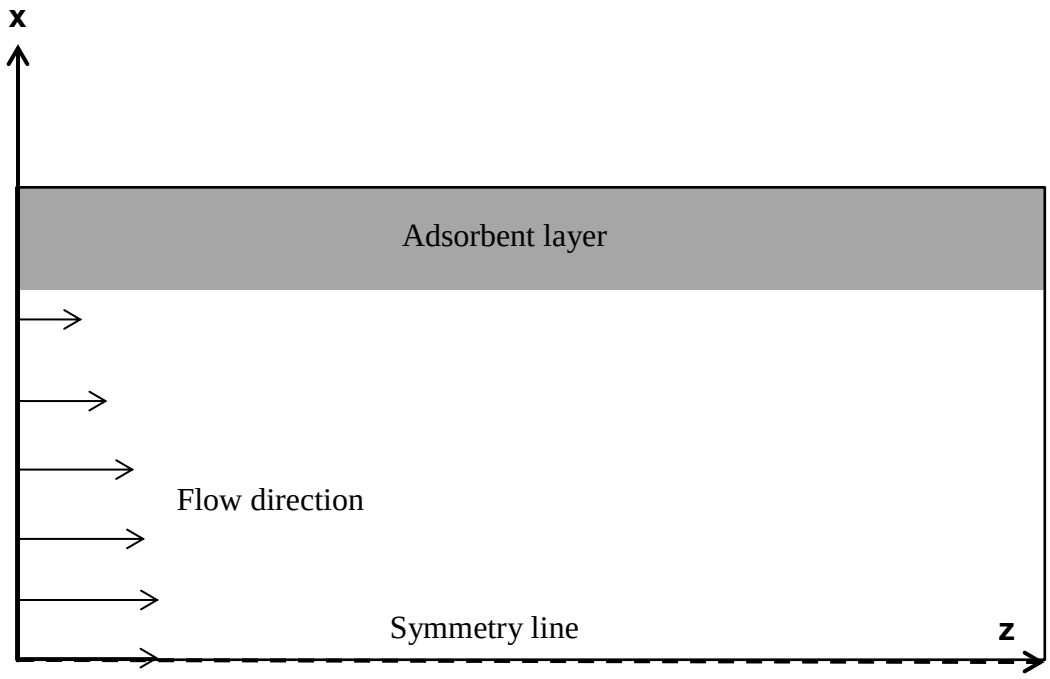

Figure 2.1 Schematic of half-cell of parallel channel adsorbent contactor

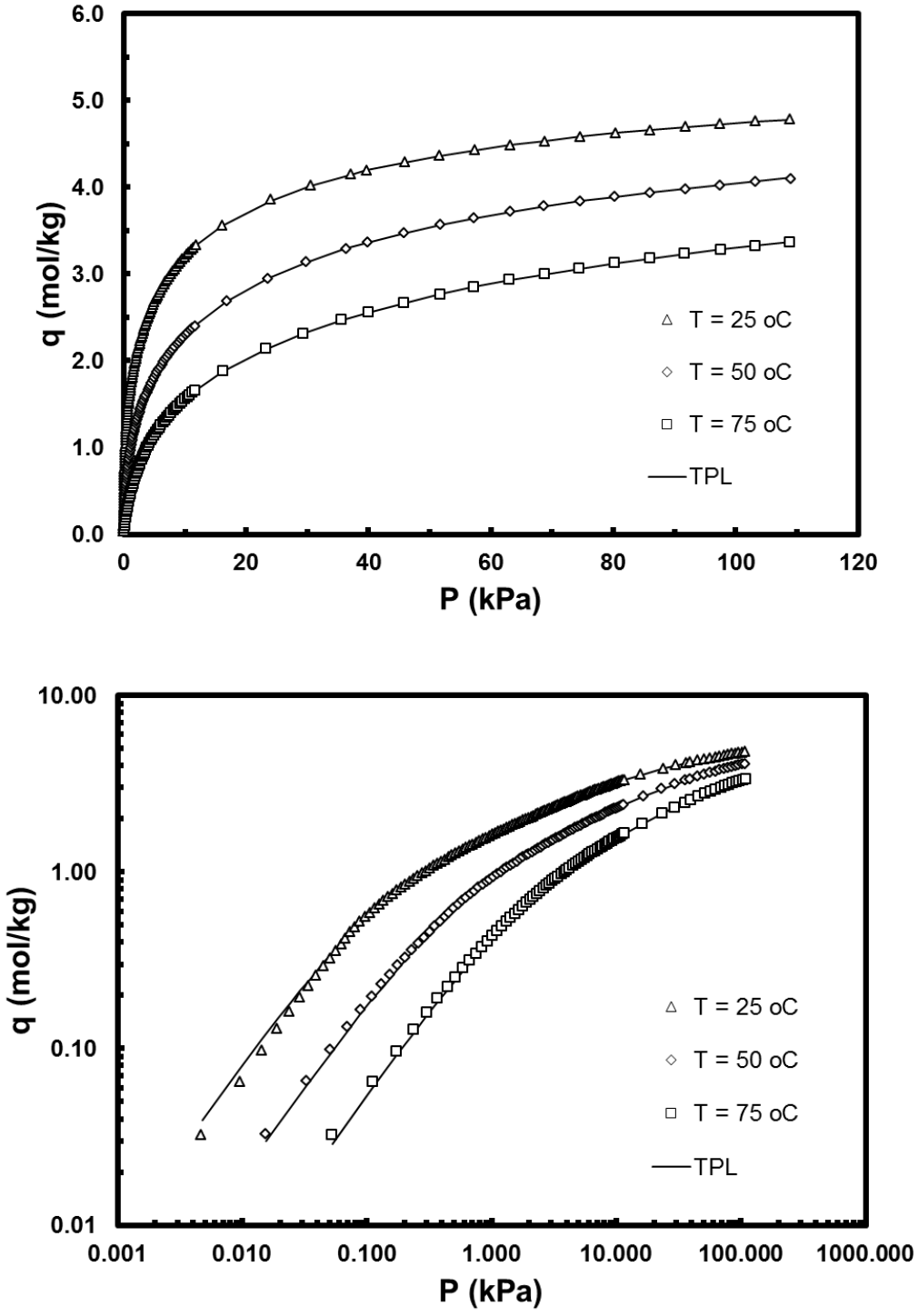

Figure 2.2 Equilibrium adsorption isotherms of CO_2 on 13X zeolite at 25, 50, and 75 Celcius. The isotherms were created by fitting Three Process Langmuir to data obtained experimentally.

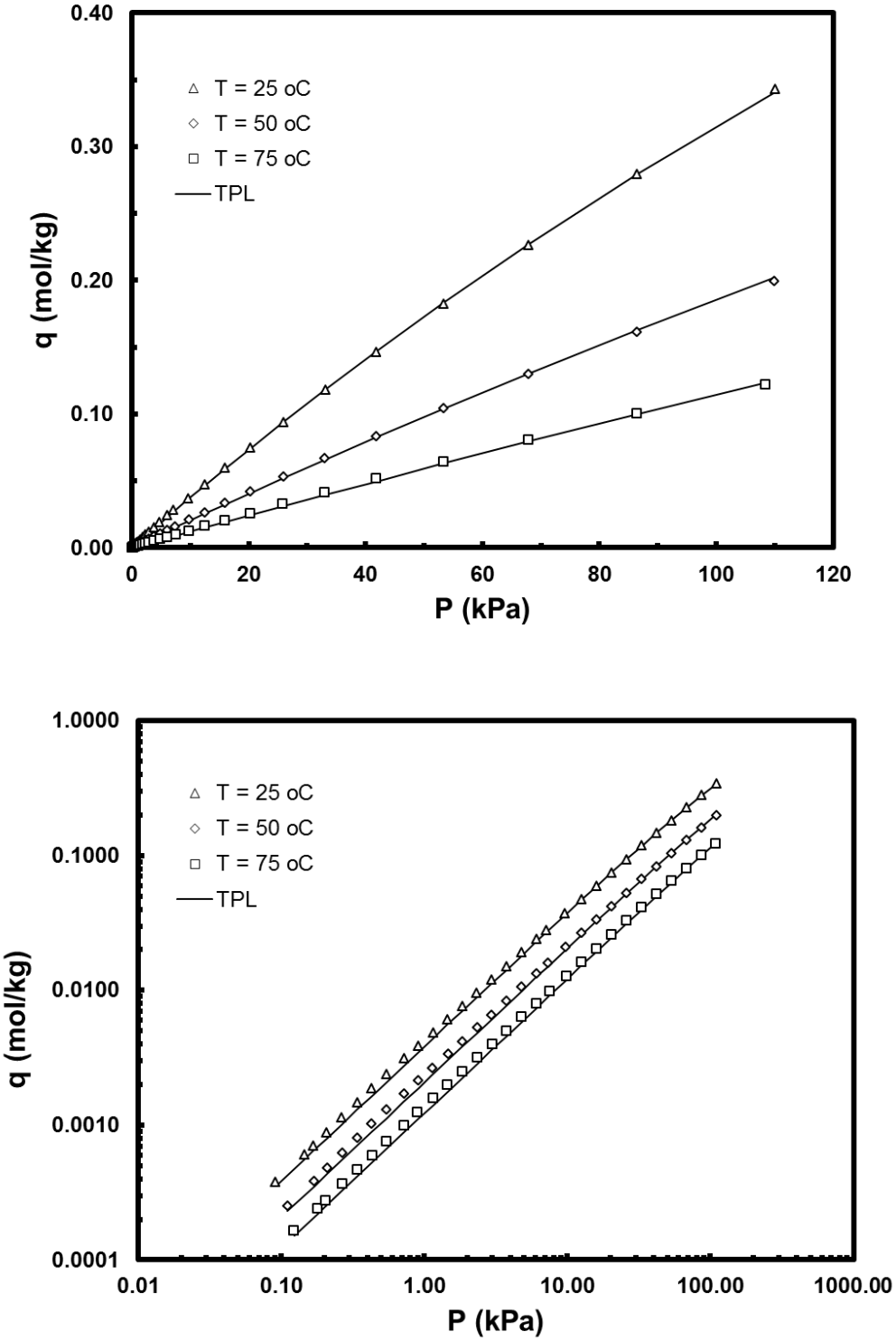

Figure 2.3 Equilibrium adsorption isotherms of N_2 on 13X zeolite at 25, 50, and 75 Celcius. The isotherms were created by fitting Three Process Langmuir to data obtained experimentally.

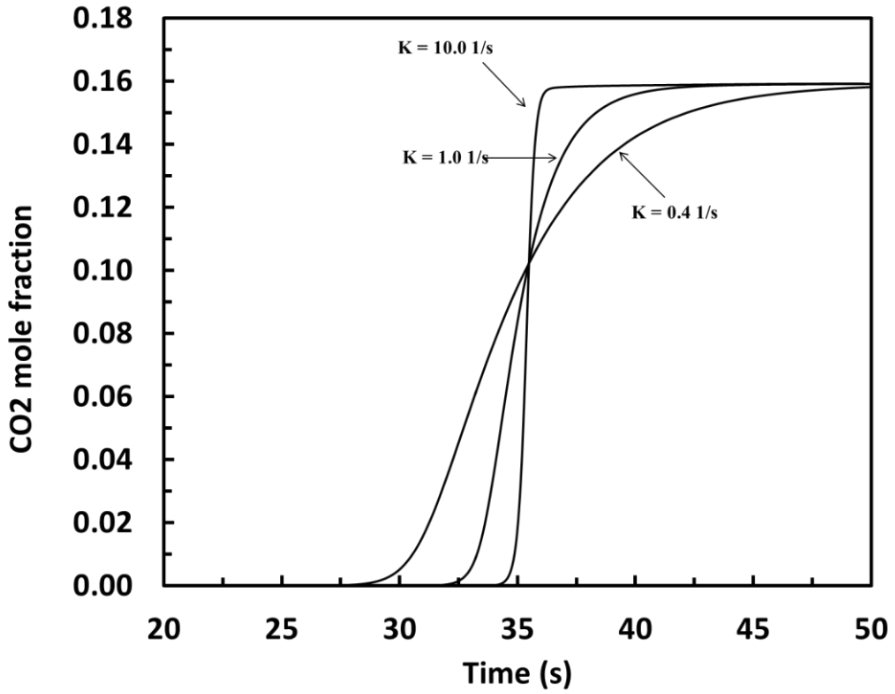

Figure 2.4 Effect of mass transfer coefficient on breakthrough curves of CO_2 at the midway point for V_{avg} = 4.715 m/s and isothermal condition

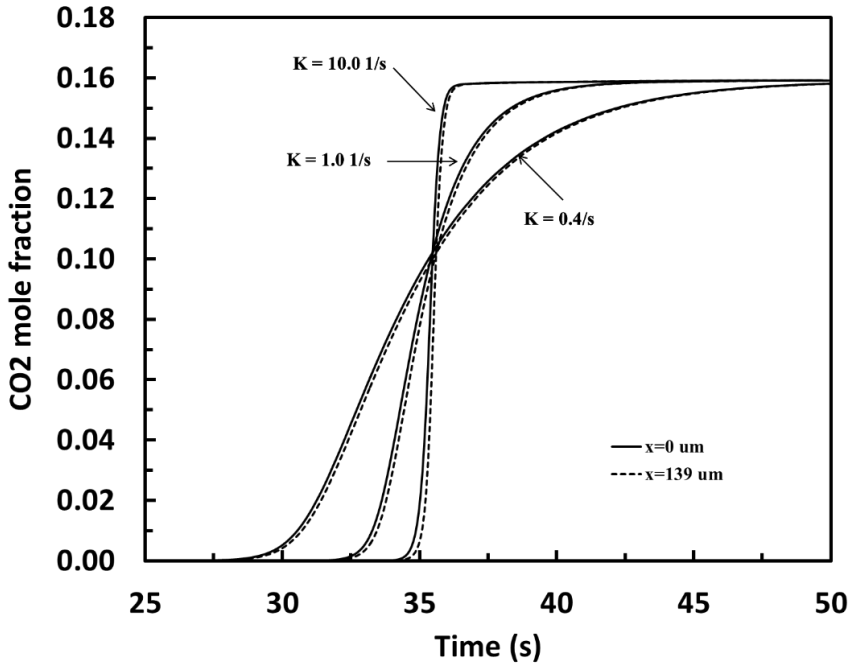

Figure 2.5 Breakthrough curves of CO_2 at the midway point and 10 µm away from the adsorbent layer for V_{avg} = 4.715 m/s and isothermal condition

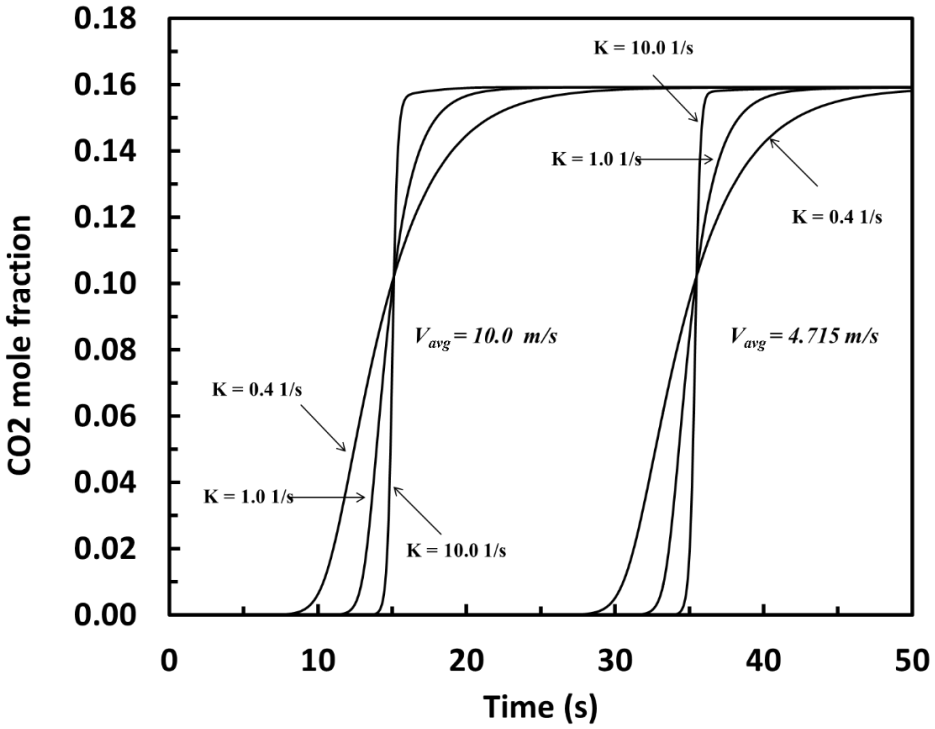

Figure 2.6 Effect of feed velocity on breakthrough curves of CO_2 at the midway point for 3 different mass transfer coefficients

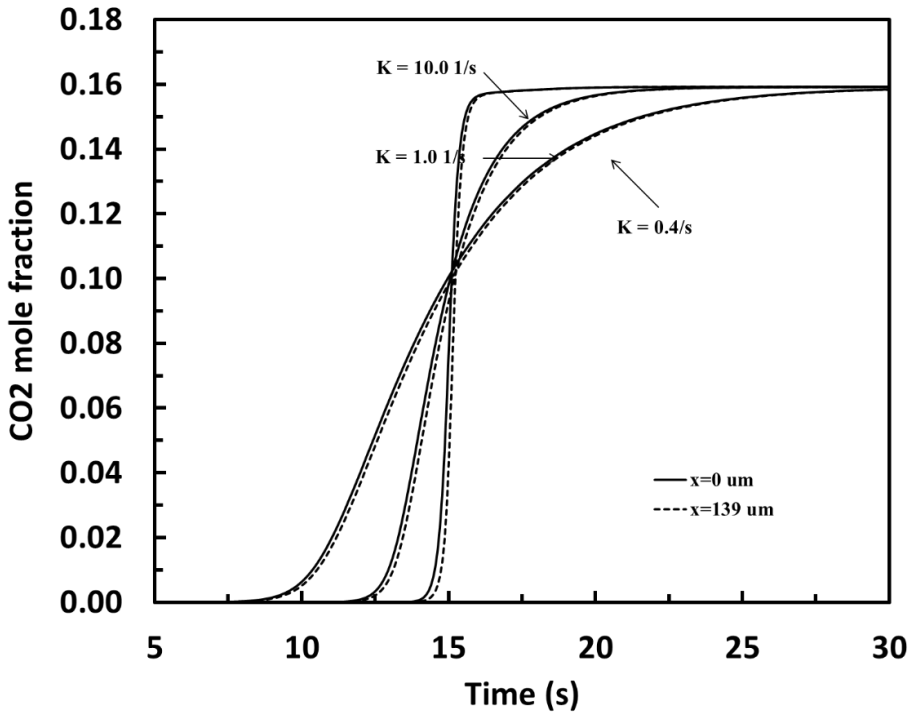

Figure 2.7 Breakthrough curves of CO_2 at the midway point and 10 μm away from the adsorbent layer for V_{avg} = 10.0 m/s and isothermal condition

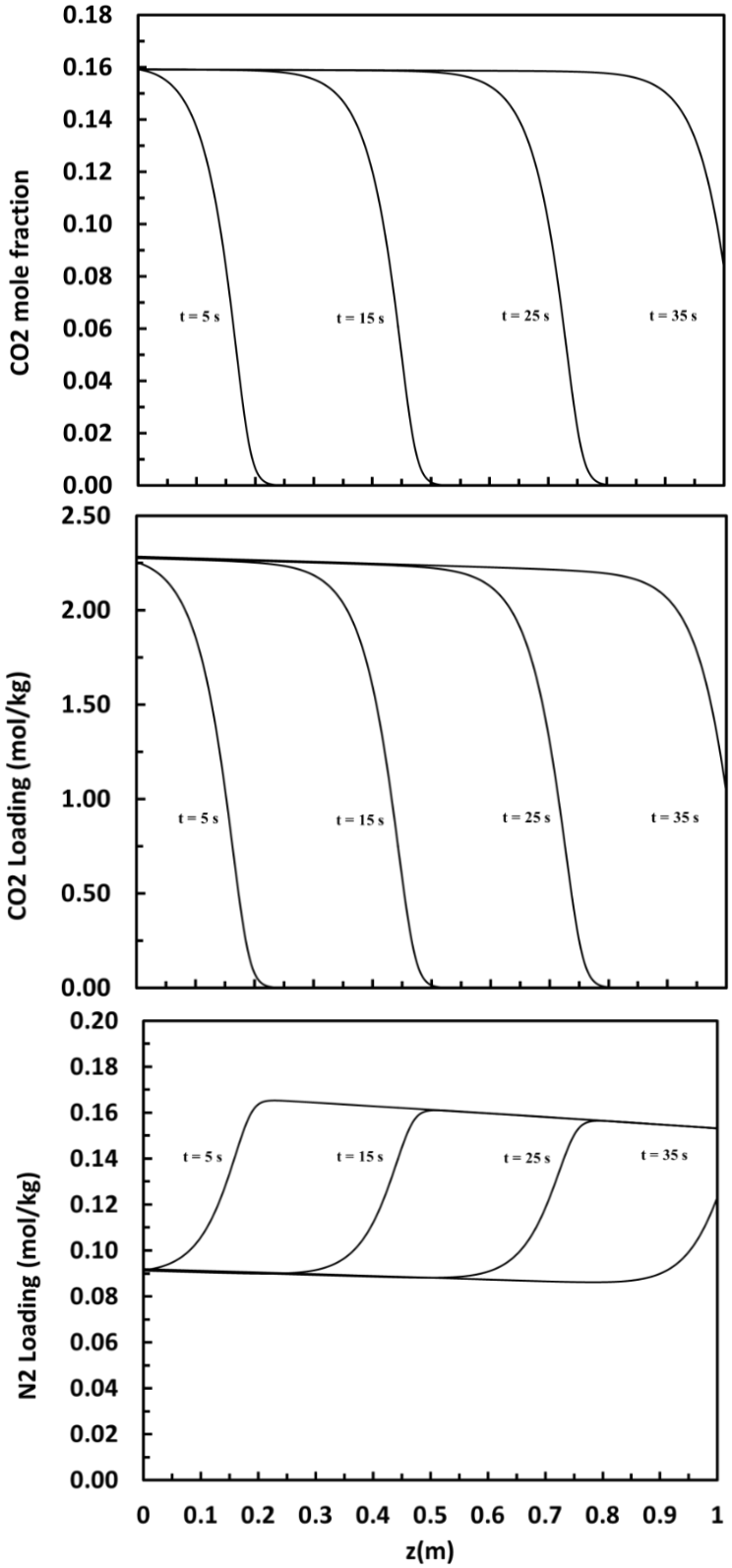

Figure 2.8 CO_2 mole fraction at midway point, CO_2 loading and N_2 loading profiles along the bed at 4 different times for V_{avg} = 4.715 m/s, K_{CO2} = 1.0 1/s and isothermal condition

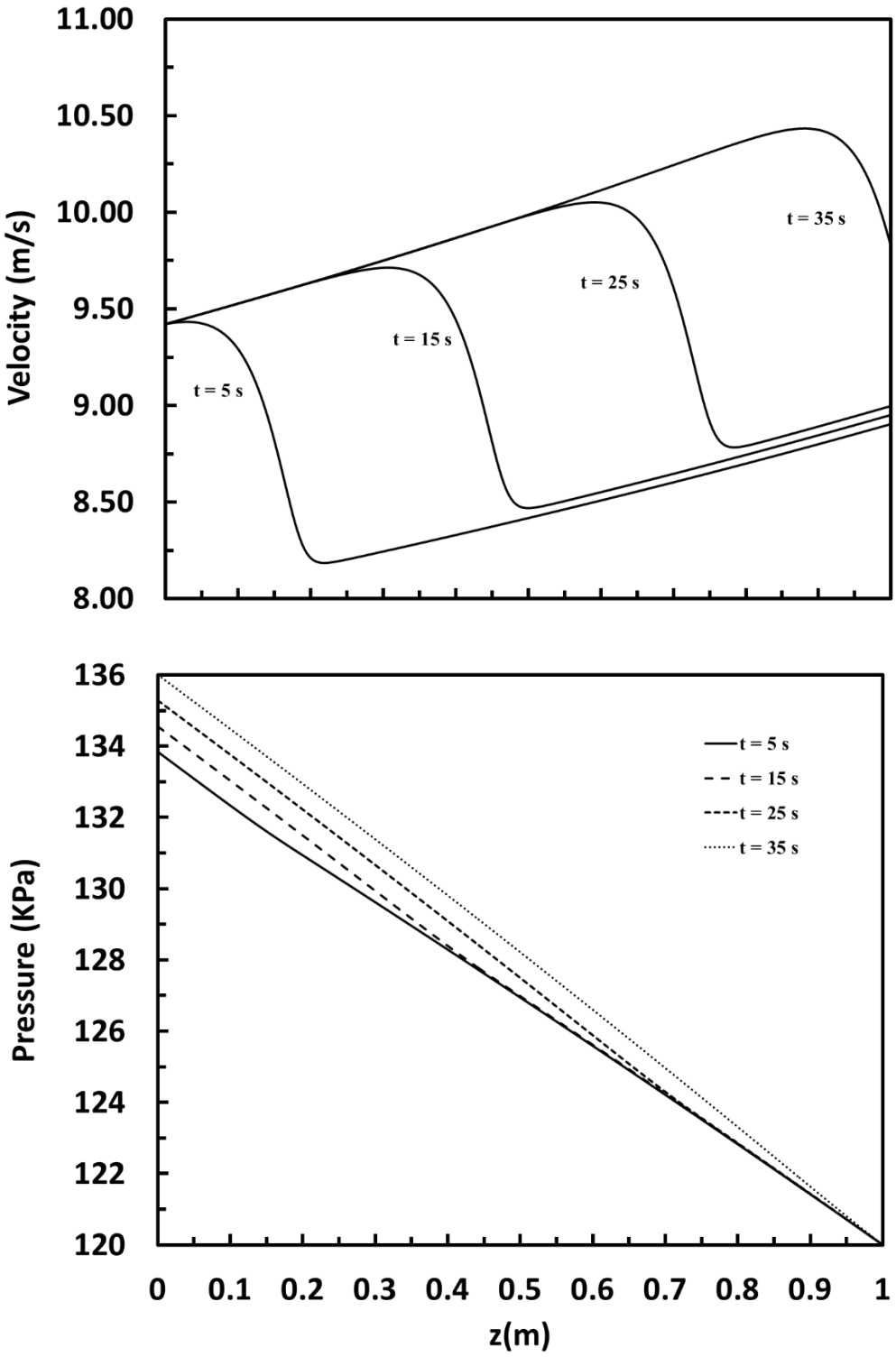

Figure 2.9 Velocity and pressure profiles at midway point along the bed at 4 different times for V_{avg} = 4.715 m/s, K_{CO2} = 1.0 1/s and isothermal condition

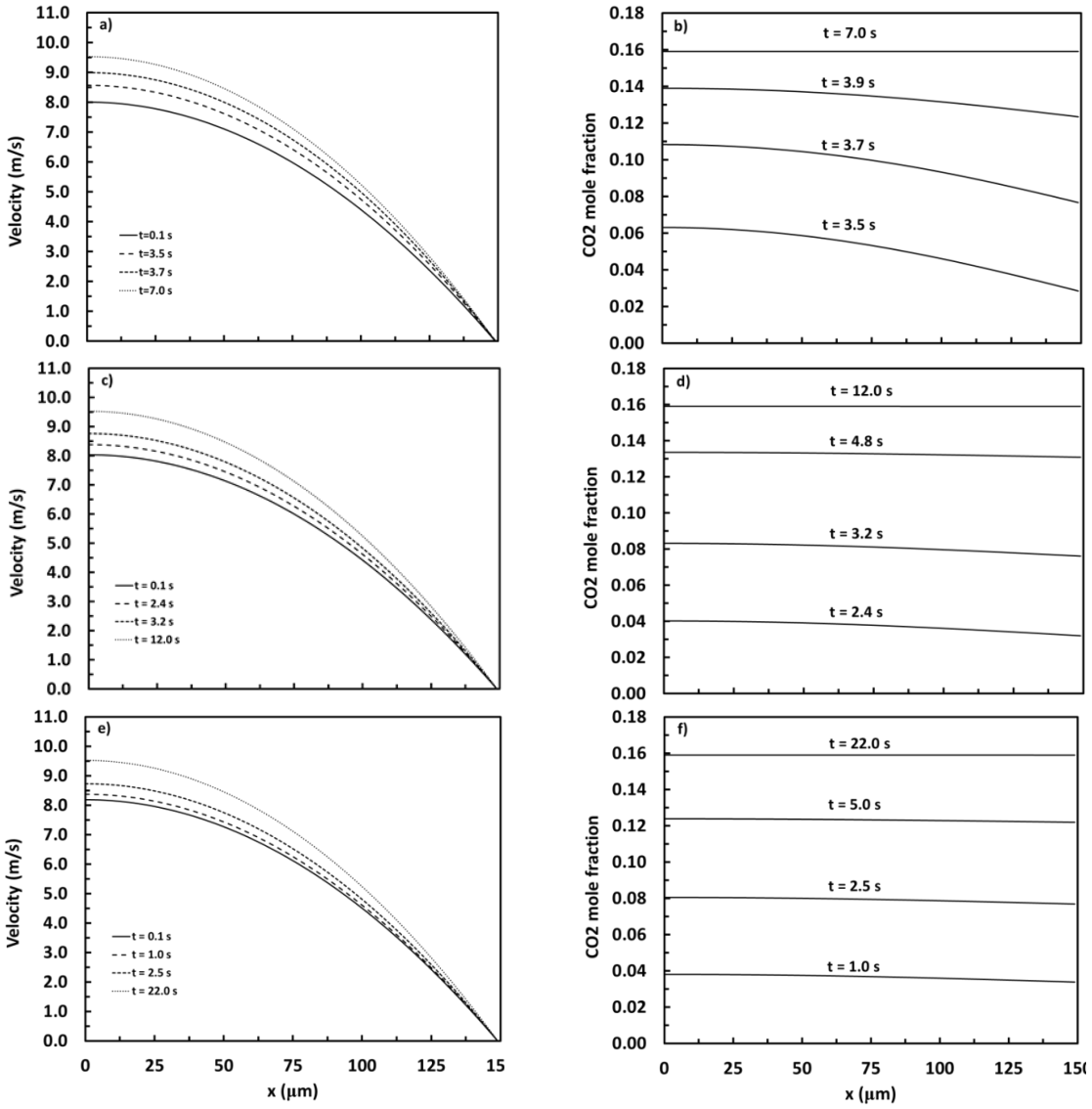

Figure 2.10 Velocity and CO_2 concentration profiles along a perpendicular direction to the axial flow at a location 10% into the channel (z/L = 0.1) and V_{avg} = 4.7 m/s (Pe = $6.25x10^{-3}$) for three different CO_2 LDF mass transfer coefficients: 10 s^{-1} for panels a and b, 1.0 s^{-1} for panels c and d, and 0.4 s^{-1} for panels e and f.

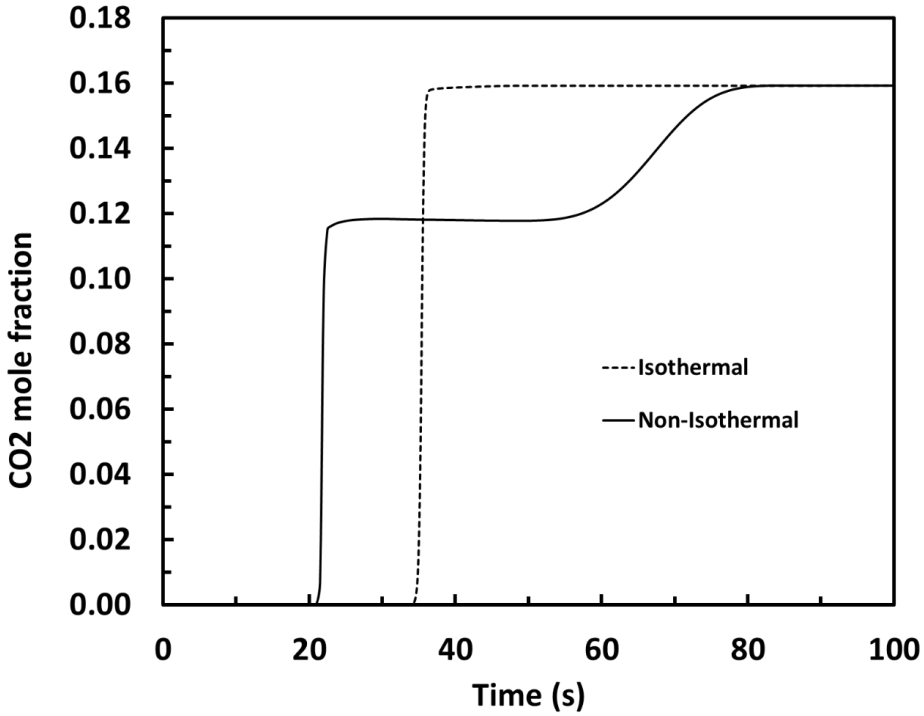

Figure 2.11 Breakthrough curves of CO_2 for isothermal (without energy balance) and non-isothermal (with energy balance) conditions at the midway point for V_{avg} = 4.715 m/s and K_{CO2}= 10 1/s.

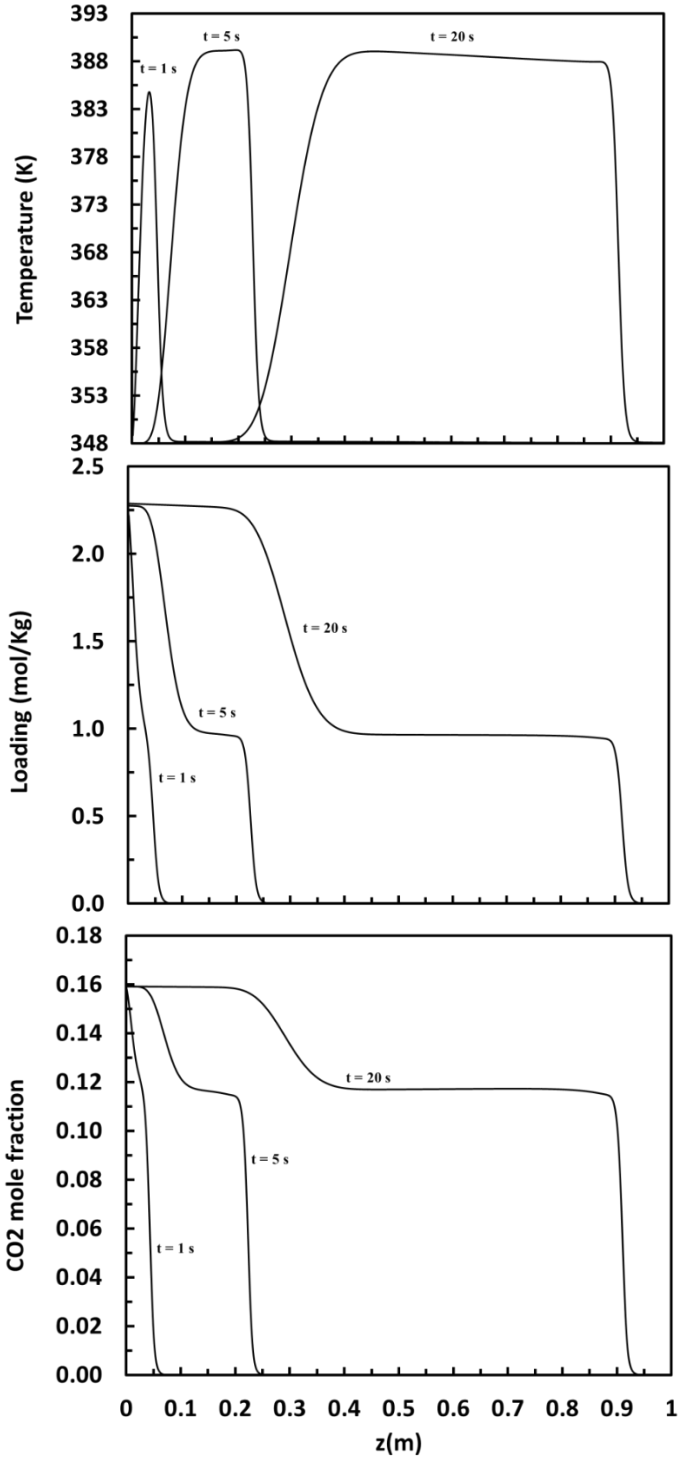

Figure 2.12 Temperature, loading and CO_2 mole fraction profiles along the bed at 3 different times for V_{avg} = 4.715 m/s and K_{CO2} = 10.0 1/s

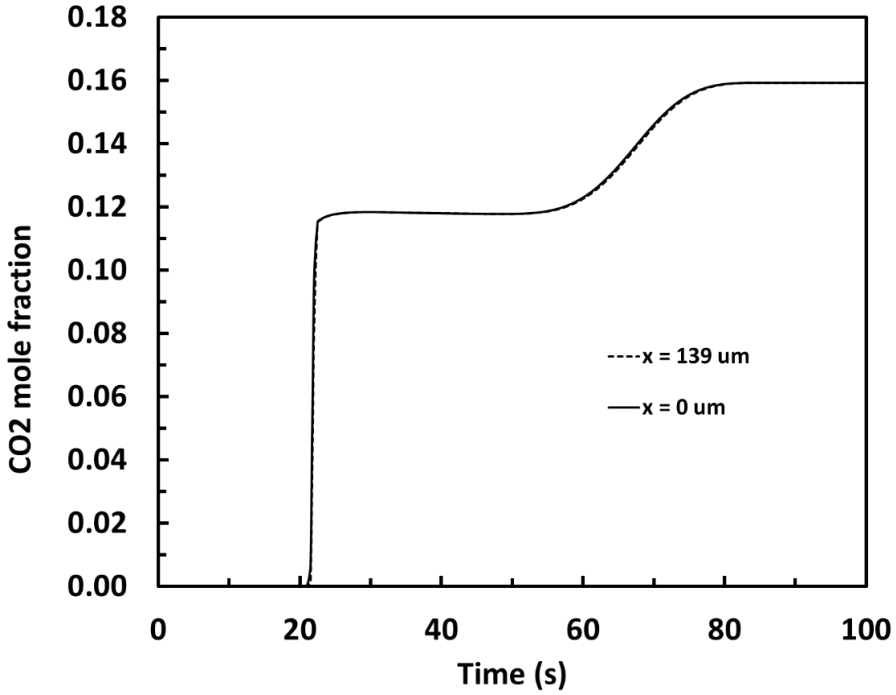

Figure 2.13 Breakthrough curves of CO_2 at the midway point and 10 μm away from the adsorbent layer for V_{avg} = 4.715 m/s, K_{CO2}= 10 1/s and non-isothermal condition

CHAPTER 3

EXPERIMENTAL AND NUMERICAL STUDY OF PRESSURE DROP IN STRUCTURED ADSORBENTS WITH NARROW TRIANGULAR CHANNELS

3.1 SUMMARY

The pressure drop of corrugated structured adsorbents with narrow triangular channels was investigated both experimentally and numerically. First a rigorous 3-D compressible Navier-Stokes model was set up and used as a base to develop a 1-D pressure drop correlation for triangular channels with the side length of 0.4 to 1.6 mm (hydraulic diameters of 0.23 to 0.92 mm). 1-D model parameters were obtained by fitting the Darcy-Weisbach equation with a special form of Darcy friction factor to the 3-D model results for air flow at atmospheric pressure. The developed pressure drop correlation was then tested for different components (i.e. CO_2 and He) and at low pressure (i.e. 5 kPa) separately and was verified by matching the 3-D Navier-Stokes model pressure drop in all cases with excellent agreement. Finally corrugated structures with different triangular channel sizes in the range of 2.18 to 1.22 mm for the side length (hydraulic diameters of 1.26 to 0.7 mm) were tested by an in-house pressure drop apparatus in 0-20 m/s range for air velocity and the model was validated by accurately predicting the experimental results. Presented pressure drop correlation can replace Ergun equation in packed bed adsorption simulators to study processes using structured adsorbents or it can be used independently for

evaluating pressure drop in triangular channels by replacing the Navier-Stokes equation and significantly reducing the computational effort and complexity.

3.2 INTRODUCTION

A randomly packed bed of adsorbent particles is the traditional mass transfer device for adsorption processes. Packed beds are cheap and versatile, but, in terms of the trade of between mass transfer resistance and pressure drop, it is rather inefficient. Such considerations become important when flow rates are high and the 'added value' of the process is low (e.g. CO_2 capture, desiccant cooling and VOC removal applications) **[30]** or when very high rates of mass transfer are required, as in rapid cycle pressure swing adsorption. Although the capital cost is substantially greater, from simple theoretical considerations it can be shown that a structured contactor in which the gas passes in laminar flow through channels covered with adsorbent shows a significant improvement in the mass transfer/pressure drop characteristics in comparison with a traditional packed bed.

Recently, there has been significant interest in the intensification of separation processes. In processes with cyclic nature such as PSA, VSA, and TSA (pressure-, vacuum-, and temperature- swing adsorption, respectively) the primary way of increasing production from a given amount of adsorbent is by reducing the cycle time. However, reducing the cycle time as mentioned before usually leads to problems such as decreased working capacity per cycle for the component of interest, decreasing the product recovery and increasing the pressure drop. The extent to which the cycle time reduces the working capacity and recovery and increases the pressure drop is dependent on the structure of the adsorbent **[31]**. Parallel channel monolithic structures with controllable shape, cell density and wall thickness have been reported for their use in adsorptive gas-separation systems

[32, 33, 34, 35, 36-39]. The primary advantage of these configurations is their lower pressure drop and higher mass-transfer rates.

Increased interest in structured adsorbents has led to attempts to develop models describing the transport phenomena in these systems. Mathematical models and simulation codes are an essential tool in process design, development and optimization nowadays. Rigorous models have been developed and used for years for packed bed adsorbents, most of these models can be used for structured adsorbents with minor changes. Mass and heat transfer models used in packed beds can describe the structured adsorbent with slight adjustments and change in parameters. The significant mathematical difference between structured and packed beds is in their pressure drop behavior. Pressure drop in packed beds is usually described by Ergun equation that cannot predict the pressure drop in channels of structured adsorbents.

Some studies claimed that the pressure drop and the flow characteristic in a microchannel cannot be correctly predicted using existing models and classical correlations for large channels. Therefore new correlations were invented to describe the fluid phenomena with better accuracy. Others found that it is usually measurement accuracy that is at the heart of these discrepancies. It should be pointed out, however, that several effects, which are normally neglected in macroscale may become significant at the microscale.

Celata et. all [40] evaluated the frictional pressure drop in micro-conduits. Experiments took place at three different institutions and results were confronted with classical theory, using a simulation model where necessary. Excellent agreement was verified between experimental friction factor data and the Hagen-Poiseuille and Blasius

equations for all conditions and diameters. It was also found that the difference in behavior between circular and rectangular channels is minimal within the aspect ratios considered.

The adiabatic flow characteristics of water flowing through stainless steel and fused silica microtubes with hydraulic diameters ranging from 0.050 to 0.254 mm were presented by **Mala and Li [41]**. Their experimental results indicate significant departure from data predicted with classical theory, more pronounced for high Reynolds number flows. These deviations increased as the diameters of microtubes decreased. Two possible reasons were assumed for these effects, either the early transition from laminar to turbulent flow or some effects due to the surface roughness. Therefore the authors also proposed a roughness-viscosity model to describe the experimental data. Good agreement was achieved.

The experimental results for water flowing through rectangular microchannels with hydraulic diameters from 0.133 to 0.343 mm have been shown by **Peng et al. [42]**. They found that friction behavior for both laminar and turbulent flow deviates from classical theory. Authors found that hydraulic diameter and aspect ratio were the most important parameters and had influences on fluid flow phenomena.

Qu et al. [43] presented pressure drop data for water through trapezoidal silicon microchannels with hydraulic diameters from 0.051 to 0.169 mm. The experimental results were compared with classical theory and found to be unpredicted. Using the roughness-viscosity model **[41]** good agreement between experimental and calculated data was found. There are many publications which describe the fluid flow phenomena with good accuracy using the classical theory. One of the first were **Flockhart and Dhariwal [44].** They presented experimental data for distilled water through trapezoidal microchannels with

hydraulic diameters ranging from 0.050 to 0.120 mm. they found that for laminar flow with Re>600 conventional fluid mechanics predict the water flow characteristics well enough.

The adiabatic experimental data for channels with diameters ranging from 0.015 to 0.15 mm and for Reynolds numbers from 8 to 2300 were presented by **Judy et al.[45]**. Distinguishable deviations from Stokes flow theory were not observed for circular and square channels made of two different materials (stainless steel and fused silica) and for three different fluids (water, methanol and isopropanol).

Wu and Cheng [46] presented the experimental study on laminar flow friction factor of de-ionized water in trapezoidal silicon microchannels with hydraulic diameters in the range of 0.026 to 0.291 mm. the results confirmed the validity of the Navier-Stokes equations.

Yang et al. [47] studied the friction characteristics for air, water and liquid refrigerant R-134a in tubes with inside diameters from 0.173 to 4.010 mm. the results showed that conventional pressure drop correlations for large tubes may be adequately used for water, refrigerant and low-speed air flow in tubes. The test friction factor for water and refrigerant R-134a agree well with Blasius and Poiseuille equations in turbulent and laminar flow regime: however, for air flow in small tubes at high Reynolds numbers, flow entered the high subsonic flow regime and the Blasius equation is no longer appropriate.

A comprehensive literature review is presented by **Hetsroni et al. [48]**. It was claimed that the behavior of the flow in microchannels, at least down to 50 μm diameter, shows no difference with macro-scale flow and that the comparison with experimental results to those obtained by conventional theory is correct when experimental conditions were consistent with the theoretical ones.

Perry and Green [49] warn that the Hagen–Poiseuille equation should not be employed in conjunction with a mean hydraulic diameter ($d_h=4A_c/P$) for the case of laminar flow in pipes of non-circular cross-section, as the mean hydraulic diameter does not accurately express how the channel shape affects the flow .

Shah and Bhatti [50] for hydro-dynamically developed flow suggested to use Darcy-Weisbach equation and provided equations to calculate friction factor in different geometries **[50, 51].** Data for hexagonal channels are provided by **Sadasivam et al. [52].**

The aim of this study is to develop a 1-D pressure drop correlation in the form of the Darcy-Weisbach equation that can predict the pressure drop in structured adsorbents with narrow triangular channels in a wide range of velocities and pressures encountered in adsorptive processes. First a rigorous 3-D compressible Navier-Stokes model is developed and used as a base to develop a 1-D correlation that can predict the pressure drop with accuracy but with much less computational cost and complexity. The 1-D correlation is then tested and verified by matching the 3-D Navier-Stokes model results for different components and under different pressure conditions with excellent agreement. Finally air flow pressure drop in corrugated structures with triangular channels of different size is measured with an in house pressure drop apparatus, and the model is validated by accurately predicting the experimental results.

Suggested pressure drop correlation can replace Ergun equation in adsorption simulators used for packed beds to study processes utilizing structured adsorbents or it can be used independently for evaluating pressure drop in triangular channels with much less computational requirements and complexity than Navier-Stokes model.

3.3 EXPERIMENTAL

Apparatus

Fig. 3.1 shows schematic of the apparatus that was constructed to study pressure drop in structured adsorbents. A building-supply compressor provides the flow by pressurizing the air to 90 PSI.A globe valve is used to regulate the air inflow to the system then flow is accurately measured by passing through a Brooks Mass flow Sensor model 5863i. Before the main runs in order to calibrate the digital flowmeter, flow was directed to a Dwyer rotameter with the maximum flow capacity of 1800 SCFH. For pressure drop experiments flow is passed through the corrugated structure. An Omegadyne inc. pressure transducers with the range of 0-30 inches of water measures the pressure drop caused by the passage of the flow through narrow channels of structured adsorbent.

Corrugated structure with triangular channels

As shown in **Fig. 3.2** structures provided by Catacel that were used in this study are constructed by wrapping a thin corrugated layer of metal foil around a central rod resulting in cylindrical structures with numerous triangular channels. Metal foil thickness is 52 μm. These cylinders were manufactured 6 in long with 1 or 1.5 in diameter and varying cell density per square inch of cross section. Higher density of cells results in smaller triangles and narrower channels. Cross section of each channel is assumed to be an equilateral triangle. Triangular cells side length a and the effective adsorbent density in bed ρ_b were calculated using the following equations:

$$a = \frac{2 * 0.0254}{\sqrt{\sqrt{3}C_D}} - \sqrt{3}(\delta_m + 2\delta_a) \quad (1)$$

$$\rho_b = \left[\frac{\left(a + 2\sqrt{3}\delta_a\right)^2 - a^2}{\left(a + 2\sqrt{3}\delta_a + \sqrt{3}\delta_m\right)^2}\right]\rho_a \quad (2)$$

Where C_D is cell density representing cells per unit area of cross section, δ_m and δ_a are metal foil and coated adsorbent layer thickness respectively and ρ_a is the density of the adsorbent layer coating.

Both uncoated and coated with zeolite structures were investigated with the pressure drop apparatus. Properties of the different corrugated structures tested in this study is presented in **Table 3.1**.

Data acquisition

During tests air flow through structured adsorbent was gradually increased up to 900 SLPM. This flow was then converted to actual velocity of flow inside channels based on the air temperature and porosity of the structure and covers a wide range of 0 to 20 m/s. Flow, pressure and temperature data was recorded during the experiment and used for further analysis. Properties of corrugated structures for each run are summarized in **Table 3.1**.

3.4 MATHEMATICAL MODEL

A single channel of corrugated structured adsorbent is chosen to perform the numerical analysis which is represented by a channel with equilateral triangle cross section as shown in **Fig. 3.3 (a)**. Symmetry allows to reduce the simulation domain and therefore computational time and effort. Analyzed domain and the corresponding coordinate system are presented separately in **Fig. 3.3 (b)** CFEB plane is the metal wall, ADEB and CADF planes are symmetry planes and the flow is considered to be in z direction.

The following assumptions are imposed in establishing the governing equations: steady flow, laminar flow, isothermal flow and ideal gas. Laminar flow is assumed because the range of the Reynolds number in the studied conditions is below critical Re of 2300, for instance one of the largest Reynolds numbers encountered in this study is for air flow at 20 m/s inlet velocity through a channel with side length of 1600 μm with atmospheric outlet pressure, in this case the calculated Re based on **Eq. 16** is 1179 which is well below the critical Re. The flow is considered isothermal due to having no heat source or sink and negligible frictional heat generation and at the studied pressures and temperatures it can safely be assumed for gas to have ideal behavior.

For a single phase, steady state and compressible flow conservation of mass or continuity and conservation of momentum for Newtonian fluids or Navier-Stokes equations in vector form are as follows:

$$\nabla.(\rho\vec{u}) = 0 \tag{3}$$

$$\rho(\vec{u}.\nabla)\vec{u} = \nabla.\left[-p\vec{I} + \mu(\nabla\vec{u} + (\nabla\vec{u})^T) - \frac{2}{3}\mu(\nabla.\vec{u})\vec{I}\right] \tag{4}$$

Where ρ, μ and p are fluid density, dynamic viscosity and pressure respectively. $\vec{u}$ is the velocity vector and in 3-D Cartesian coordinate is expressed as:

$$\vec{u} = u\vec{\imath} + v\vec{\jmath} + w\vec{k} \tag{5}$$

Density is related to pressure using the Ideal gas law:

$$\rho = \frac{pM}{RT} \tag{6}$$

The Boundary conditions to solve the governing equations according to the corresponding coordinate system shown in **Fig. 3.3** are specified as follows.

First a uniform velocity is applied at the channel inlet:

$$u = 0\ m/s, \quad v = 0\ m/s, \quad w = w_{in}\ m/s \qquad for\ z = 0\ m\ and\ all\ x, y \tag{7}$$

At the channel outlet no viscous stress boundary condition is applied and the pressure is set to the outlet pressure value:

$$\tau.\vec{k} = 0, \qquad \tau = \left[\mu(\nabla\vec{u} + (\nabla\vec{u})^T) - \frac{2}{3}\mu(\nabla.\vec{u})I\right] \quad for\ z = L\ m\ and\ all\ x, y \tag{8}$$

$$p = p_{out}\ Pa \qquad for\ z = L\ m\ and\ all\ x, y \tag{9}$$

Where τ is the viscous stress tensor for Newtonian compressible fluid, L is the length of the channel and p_{out} is the pressure at the outlet of the channel.

No-slip condition is imposed on the solid boundary and the velocity is set to zero.

$$u = 0\ m/s, \quad v = 0\ m/s, \quad w = 0\ m/s \qquad for\ x = 0\ m\ and\ all\ y, z \tag{10}$$

On the symmetry planes the symmetry boundary condition prescribes no penetration and vanishing shear stresses:

$$\vec{u}.\vec{n} = 0 \tag{11}$$

$$\vec{K} - (\vec{K}.\vec{n})\vec{n} = 0, \qquad \vec{K} = \left[\mu(\nabla\vec{u} + (\nabla\vec{u})^T) - \tfrac{2}{3}\mu(\nabla.\vec{u})I\right].\vec{n} \tag{12}$$

Expressing that there is no flow across the boundary and no viscous stress in the tangential direction.

The equations described above constitute a complete mathematical model for steady state flow. There are a total of 4 variables (u, v, w and p) and 4 equations (N-S eq. in x, y and z directions and Continuity eq.) that have to be solved at each node.

The 1-D pressure drop correlation for structured adsorbents with triangular channels that is developed in this work based on the 3-D N-S model has the general form of the Darcy-Weisbach equation which relates the pressure loss due to friction along the length of a pipe or channel to the average velocity of the fluid flow. The pressure drop correlation along with the continuity equation form the full 1-D model:

$$\frac{\partial(\rho w)}{\partial z} = 0 \tag{13}$$

$$\frac{\partial p}{\partial z} = -f_D(Re).\rho\frac{w^2}{2D_h} \tag{14}$$

f_D is the Darcy friction factor and it is usually calculated using Hagen–Poiseuille eq. for laminar flow or Blasius eq. for turbulent flow but in this study friction factor is assumed to have the following form including both viscous and inertial effects similar to Darcy-Forchheimer equation for flow in porous media:

$$f_D(Re) = f_1 + \frac{f_2}{Re} \tag{15}$$

The Reynolds number and hydraulic diameter for equilateral triangular channels are expressed as:

$$Re = \frac{\rho w D_h}{\mu} \tag{16}$$

$$D_h = \frac{\sqrt{3}a}{3} \tag{17}$$

Where f_1 and f_2 are fitting parameters.

The Boundary conditions required to solve the 1-D model are defined as:

At the channel inlet:

$$w = w_{in}\ m/s \qquad for\ z = 0\ m \tag{18}$$

At the channel outlet:

$$p = p_{out}\ Pa \qquad for\ z = L\ m \tag{19}$$

The governing equations and boundary conditions were set up and solved in COMSOL Multiphysics 5.2 which uses finite element analysis. Sensitivity of the numerical results to mesh size was also tested with different mesh sizes and an appropriate size was chosen to ensure accuracy with minimum computational effort and time.

3.5 RESULTS AND DISCUSSION

Solving a 3-D N-S model is complicated and requires considerable time and computational resources, also in adsorption processes usually the gradient of variables only in the flow direction is significant and changes in other directions can be neglected, therefore adsorption simulators often use 1-D models. In packed bed models, momentum equation is replaced by Ergun equation but this equation cannot be used for structured adsorbents so it seems appropriate to develop a 1-D pressure drop correlation able to predict the pressure drop with good accuracy that can replace the N-S equation for structured adsorbents.

In order to develop a pressure drop correlation replacing the N-S equation that can match the 3-D model results over a wide range of channel sizes and velocities; first the 3-D N-S model was used to generate numerical results in the range of interest for channel size and velocity. To eliminate the undeveloped entrance region effects a minimum channel length for 3-D N-S simulations should be determined in which the entrance effects are negligible and flow can be considered fully developed throughout the channel. **Fig. 3.4** shows that for short channels at high velocities entrance region effects the overall pressure drop. It can be observed that for the largest channel in this study with 1600 μm side length (D_h = 0.92 mm), a minimum channel length of 18 inches can ensure length independent, fully developed results. According to **Eq.20** that estimates the entrance length in laminar flow through pipes, this length decreases by reducing the diameter and therefore minimum channel length of 18 inches provides appropriate results for smaller channels too.

$$\frac{l_e}{d} = 0.06Re \tag{20}$$

Where l_e is the length of the entrance region and d is the pipe diameter.

Next the general 1-D D-W form correlation was fitted to the 3-D model results and the correlation parameters were obtained. Preliminary studies showed that channels with triangle sides less than 400 μm create high pressure drop and eliminate the advantage of structured adsorbents over packed beds. On the other hand according to **Table 3.3** effective adsorbent density of the bed for channels with sides larger than 1600 μm is too low which limits the performance of the adsorption column and negatively affects the purity of the heavy product. Therefore in the development of the pressure drop correlation, channels with triangle sides in the range of 400 to 1600 μm were considered. Gas velocities were selected to be in the range of 0-20 m/s that includes all relevant applications of structured adsorbents.

3-D results show that the pressure drop of the channel with1600 μm side length is relatively small even at high velocities and therefore air density can be assumed constant throughout the channel, also according to continuity equation (**Eq.13**) in 1-D model, constant density leads to constant velocity in the channel. With constant values for density (air density in atmospheric pressure and 25 C) and velocity (inlet velocity) and initially guessed friction factor parameters f_1 and f_2, **Eq.14** was easily integrated for each velocity and calculated overall pressure drop from the 1-D correlation was then compared to the 3-D model results for 1600 μm channel and an error was calculated for each velocity. The final fitting parameters were obtained by simultaneously regressing all the data for different velocities by minimizing the sum of errors $\sum\left[\log\left(\frac{(\frac{\Delta p}{L})_{N-S}}{(\frac{\Delta p}{L})_{D-W}}\right)\right]^2$ using Solver in MS Excel. It must be noted that Solver was used on rescaled parameters with the range of 0.1 to 10. Two set of parameters were obtained for two separate cases, first in **Eq. 15** f_1 was set to zero and a single parameter form for friction factor was considered. In the second case both

f_1 and f_2 were varied to achieve the best fit possible. Dimensionless parameters f_1 and f_2 and coefficient of determination for both cases are given in **Table 3.2**.

Subsequently a full 1-D model including the pressure drop correlation with determined parameters (**Eq.14**) along with continuity equation (**Eq.13**) was set up in COMSOL Multiphysics 5.2. With proper boundary conditions (**Eqs.18** and **19**) the model was solved and pressure drop was predicted for channels with side length of 800 and 400 μm based on the parameters obtained for 1600 μm channel. **Fig. 3.5** and **Fig. 3.6** show the 3-D Navier-Stokes model results for air flow through three different channel sizes of 400, 800 and 1600 μm (i.e. hydraulic diameters of 0.23, 0.46 and 0.92 mm) at 25C with 1 atm outlet pressure and over 0 to 20 m/s range for inlet velocity. 1600 μm channel results are plotted against the fitted 1-D correlation with one parameter in **Fig. 3.5** and with two parameters in **Fig. 3.6**. For 800 and 400 μm channels, predicted pressure drop using the full 1-D model is compared to the N-S model results. As displayed in the figures, in both cases the 1-D correlation not only fits the 3-D Navier-Stokes data very well for 1600 μm but also predicts the pressure drop in 800 and 400 μm channels over the whole range of velocities with excellent agreement. However, coefficients of determination show that the friction factor model with two parameter fits and predicts the 3-D model results better than a single parameter model (f_1=0), therefore in the rest of this study a two parameter friction factor equation was used to ensure better results.

Next the developed pressure drop correlation needs to be tested and verified against 3-D model results for other components and a wide range of density and viscosity. In order to cover a wide range for density in addition to air a heavier gas (i.e. CO_2) and a lighter gas (i.e. He) were chosen. Different range of viscosities for the selected components also

provides a chance to test the 1-D model in case of a change in viscosity. First the compressible 3-D Navier-Stokes model was utilized to calculate the pressure drop of CO_2 or He at 25C and atmospheric outlet pressure. Then the full 1-D model with parameter obtained in the last step was independently solved for each gas to predict the pressure drop under the above mentioned conditions. **Fig. 3.7** and **Fig. 3.8** compare the 3-D Navier-stokes model results with the 1-D pressure correlation model for CO_2 and He. Although the 1-D model uses pressure drop correlation with parameters obtained from air flow, as shown in **Fig. 3.7** and **Fig. 3.8** there is an excellent agreement between 1-D model prediction and 3-D models results for both components over the whole range of velocities and channel sizes. In order to test the correlation under different pressure conditions the 1-D pressure drop correlation was tested for air flow with 5kPa outlet pressure, **Fig. 3.9** shows that even under vacuum conditions the 1-D correlation is able to predict the 3-D model results with precision.

These results show that the 1-D correlation is able to match the 3-D N-S results with accuracy under a wide range of density, viscosity, velocity and channel sizes and verify that the 1-D Darcy-Weisbach correlation can replace the 3-D Navier-Stokes equation to predict the pressure drop in structured adsorbents and reduce the complexity of the model and the computational effort required to solve it.

Last step is to validate the developed 3-D Navier-Stokes model and hence the 1-D pressure drop correlation with experimental data for structures with different properties and in a wide range of operational velocities. All experiments and conditions for each run are summarized in **Table 3.1**. **Fig. 3.10** compares the experimentally measured pressure drop in runs 1 and 2 with the CFD model prediction for air flow with velocities ranging

from 0 to 20 m/s. Two corrugated structures with diameters of 1 and 1.5 and the length of 6 inches with the lowest cell density of 290 cells per square inch (CPSI) that corresponds to the largest channels (i.e. 2.18 mm triangle side or 1.26 mm hydraulic diameter) were tested with the pressure drop apparatus. As shown in the figure and as expected pressure drop was not affected by the corrugated structure diameter and it is only a function of the channel size. The 3-D model was able to predict the experimental results with excellent agreement.

Next a 6 inch long core with diameter of 1 inch and cell density of 360 CPSI that corresponds to triangle side of 1.94 mm or hydraulic diameter of 1.12 mm was tested in run 3. **Fig. 3.11** presents experimentally measured and numerically predicted pressure drop per unit length vs. interstitial velocity. As observed in the figure CFD model almost overlaps the experimental data in the whole range.

Subsequently in run 4 the experimentally obtained results for a core coated with 31 μm of 13X zeolite with highest cell density i.e.740 CPSI and smallest channel size i.e. 1.22 mm side length or 0.7 mm hydraulic diameter, was compared to the numerical model. As seen in **Fig. 3.12** once again the model precisely matches the experimental results.

Fig. 3.13 summarizes the experimental results for different corrugated structures and compares the pressure drop in structured adsorbent with a typical packed bed over a wide range of superficial velocities. The considered packed bed in this part is filled with 4.32 mm glass beads and has the bed void fraction of 0.41. Pressure drop in packed beds is evaluated by Ergun equation:

$$\frac{\partial p}{\partial z} = \frac{150\mu v_s}{{d_p}^2}\frac{(1-\varepsilon)^2}{\varepsilon^3} + \frac{1.75\rho {v_s}^2}{d_p}\frac{(1-\varepsilon)}{\varepsilon^3} \qquad (21)$$

Where d_p is the particle diameter, ε is the packed bed porosity and v_s is the local superficial velocity in the bed.

It is seen that even for structures with narrow channels, structured adsorbents offer much less resistance and pressure drop when compared to conventional packed beds. Above mentioned findings illustrate that the 3-D Navier-Stokes model is able to predict the experimental data with great accuracy for different size channels and over a wide range of velocities and since it was shown that the 1-D correlation can be an accurate replacement for 3-D Navier-Stokes model, the 1-D pressure drop correlation is validated against the experimental results.

3.6 CONCLUSION

Pressure drop characteristics of corrugated structured adsorbents with narrow triangular channels were studied both experimentally and numerically. A 1-D pressure drop correlation was developed by fitting the Darcy-Weisbach equation with special form of Darcy friction factor to the results obtained from a rigorous 3-D compressible Navier-Stokes model for air flow at atmospheric pressure. The 1-D pressure drop correlation was then tested for two different components (i.e. CO_2 and He) and at low pressure (i.e. 5 kPa) separately and was validated by matching the 3-D N-S model results in all cases with excellent agreement. Finally the 3-D model was shown to be able to accurately predict the experimental results obtained from an in house apparatus in 0-20 m/s range for air velocity and 2.18 to 1.22 mm range for triangular channel side length (hydraulic diameters of 1.26 to 0.7 mm). Experimental and numerical results indicated that for shorter channels at high velocities, length of the entrance region where the flow is not yet fully developed can be comparable to channel length and the overall pressure drop can increase. Simulations

showed that a minimum length of 18 inches for the channel ensures negligible entrance region effect on the results for the largest channel with 1600 μm side length (D_h = 0.92 mm) and consequently narrower channels.

3.7 TABLES

Table 3.1 Properties of corrugated structures for each experimental run.

Experiment	Structure diameter[m]	C_D [CPSI]	δ_a [m]	a [m]	D_h [m]	ε
1	0.0254	290	0	2.18E-3	1.26E-3	0.92
2	0.0381	290	0	2.18E-3	1.26E-3	0.92
3	0.0254	360	0	1.94E-3	1.12E-3	0.91
4	0.0254	740	31E-6	1.22E-3	7.0E-4	0.74

Table 3.2 Parameters obtained by fitting the 1-D D-W to 3-D N-S results for air flow through a 18 in long channel with 1600 μm side length at atmospheric pressure and 25C over 0-20 m/s range for inlet velocity.

	f_1	f_2	R^2
1-Parameter	0	53.88647	0.9982
2-Parameter	$5.00646*10^{-3}$	50.83876	0.9996

Coefficients of determination are calculated based on how well the model simultaneously fits 1600 μm and predicts 800 μm and 400 μm side length channels.

Table 3.3 Range of cell density and effective adsorbent density for channels with smallest and largest side lengths used in the pressure correlation development with different adsorbent coating thicknesses.

a [m]	δ_a [m]	C_D [CPSI]	ρ_b [kg/m^3]
4.0E-4	0.0	6204	0.0
	3.0E-5	4223	292.9
	5.0E-5	3387	421.5
	1.0E-4	2129	624.3
1.6E-3	0.0	522	0.0
	3.0E-5	463	117.4
	5.0E-5	429	185.1
	1.0E-4	359	325.8

Results are obtained by assuming δ_m = 5.2E-5 m and ρ_a= 1100 kg/m^3 and calculated from **Eqs. (1)** and **(2)**

3.8 FIGURES

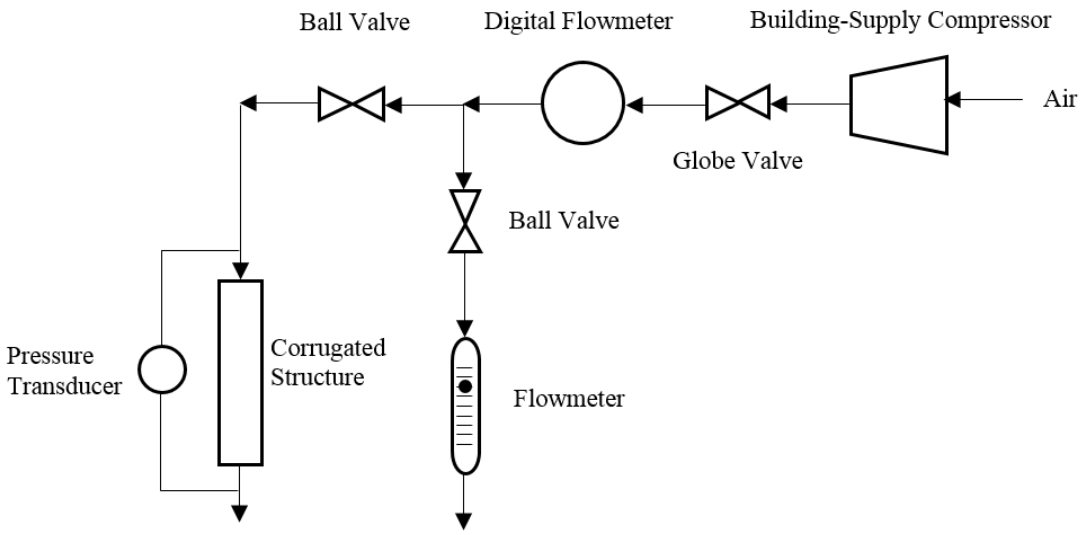

Figure 3.1 Schematic of the experimental pressure drop apparatus

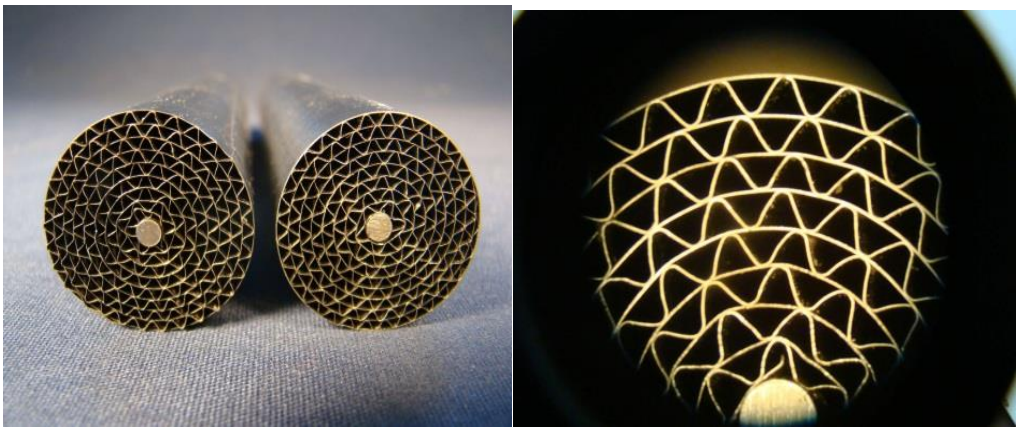

Figure 3.2 Catacel corrugated structures with triangular channels

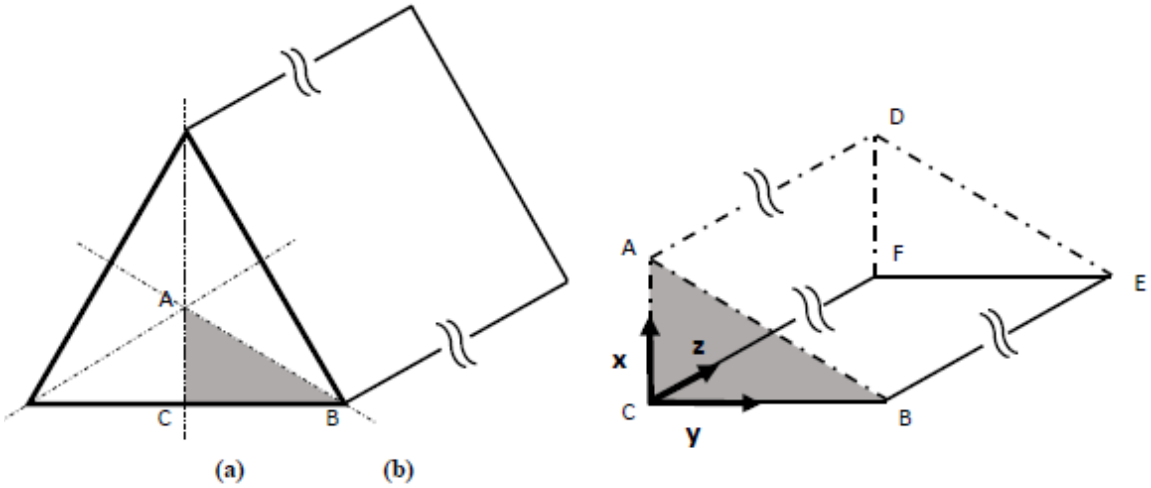

Figure 3.3 (a) A prism with equilateral triangle cross section representing a single channel of corrugated structure **(b)** reduced computational domain due to symmetry along with corresponding coordinate system.

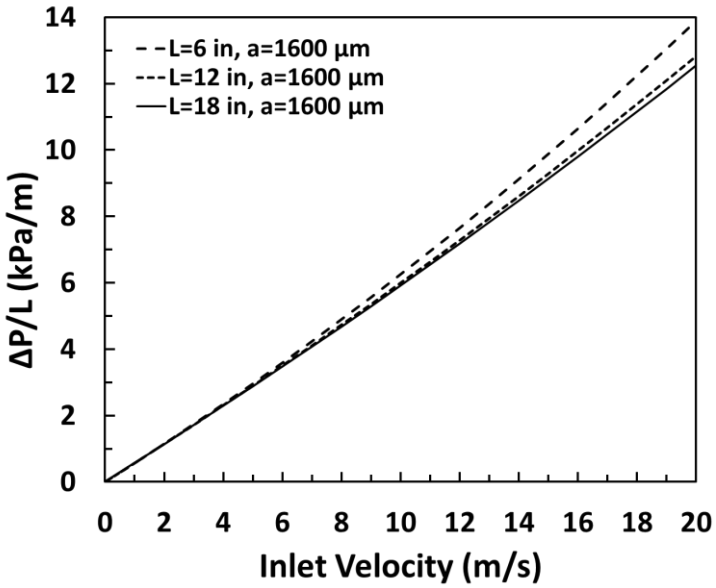

Figure 3.4 Overall air flow pressure drop per unit length vs. inlet velocity of simulation results for three different channel lengths at 25C and atmospheric outlet pressure.

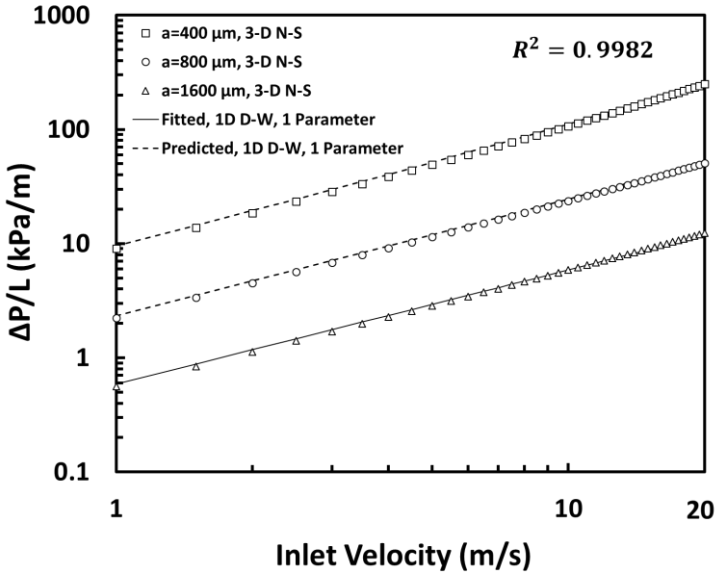

Figure 3.5 3-D N-S model results of air flow at 25C and atmospheric outlet pressure for channels with three different triangle sides and 18 inches in length in a wide range of operational velocity fitted and predicted with 1-D D-W model with 1 parameter friction factor.

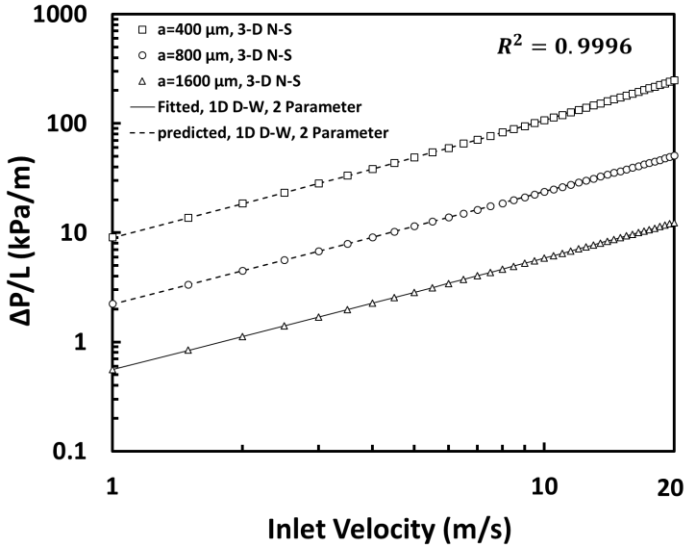

Figure 3.6 3-D N-S model results of air flow at 25C and atmospheric outlet pressure for channels with three different triangle sides and 18 inches in length in a wide range of operational velocity fitted and predicted with 1-D D-W model with 2 parameter friction factor.

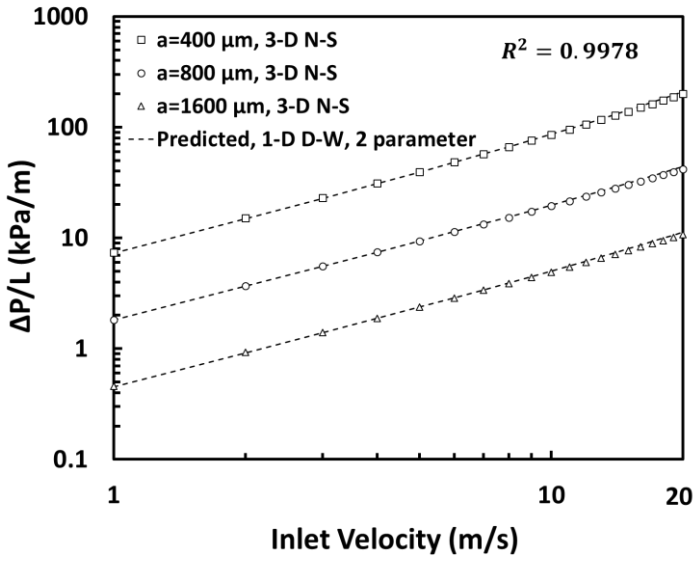

Figure 3.7 3-D N-S model results of CO_2 flow at 25C and atmospheric outlet pressure for channels with three different triangle sides and 18 inches in length in a wide range of operational velocity predicted with 1-D D-W model with 2 parameter friction factor.

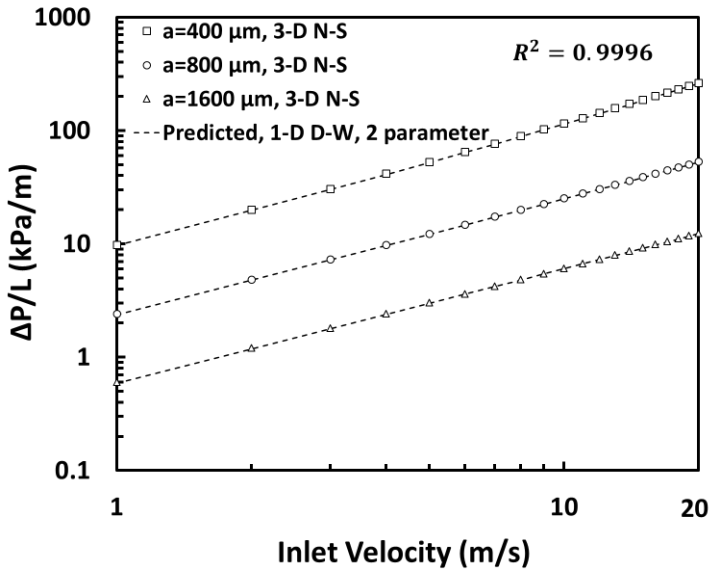

Figure 3.8 3-D N-S model results of He flow at 25C and atmospheric outlet pressure for channels with three different triangle sides and 18 inches in length in a wide range of operational velocity predicted with 1-D D-W model with 2 parameter friction factor.

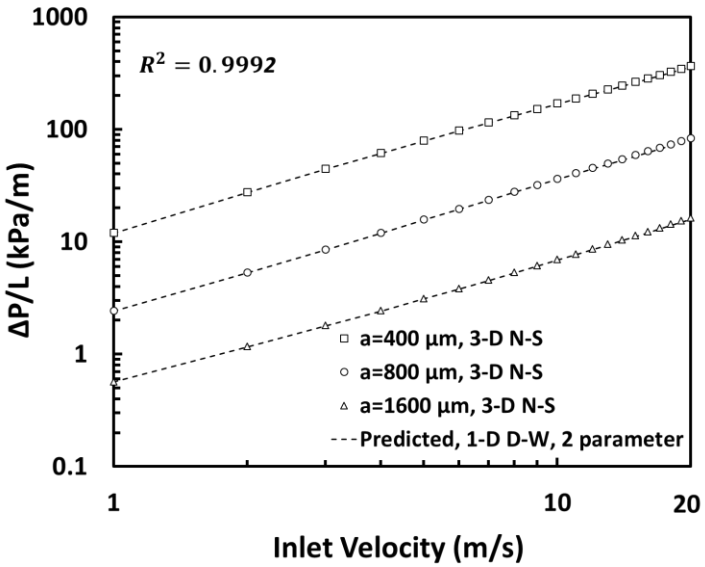

Figure 3.9 3-D N-S model results of air flow at 25C and 5kPa outlet pressure for channels with three different triangle sides and 18 inches in length in a wide range of operational velocity predicted with 1-D D-W model with 2 parameter friction factor.

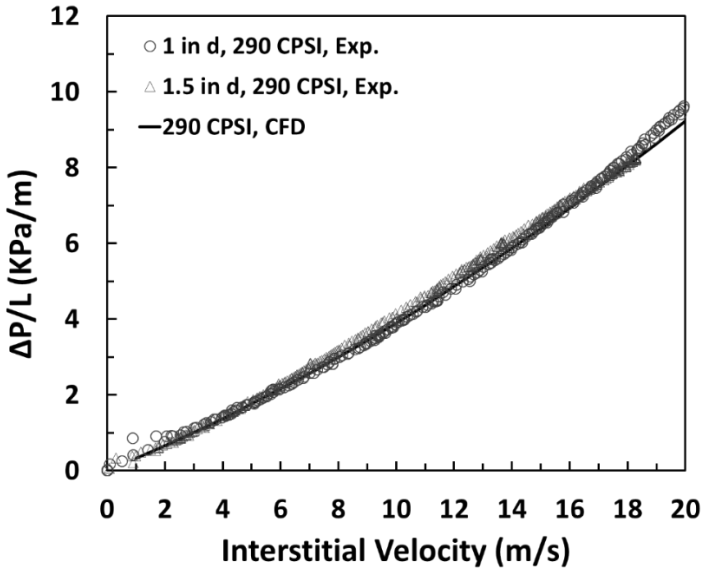

Figure 3.10 Pressure drop per unit length vs. interstitial velocity, comparing experimental results with CFD model prediction for two different diameters of corrugated structures with cell density of 290 CPSI.

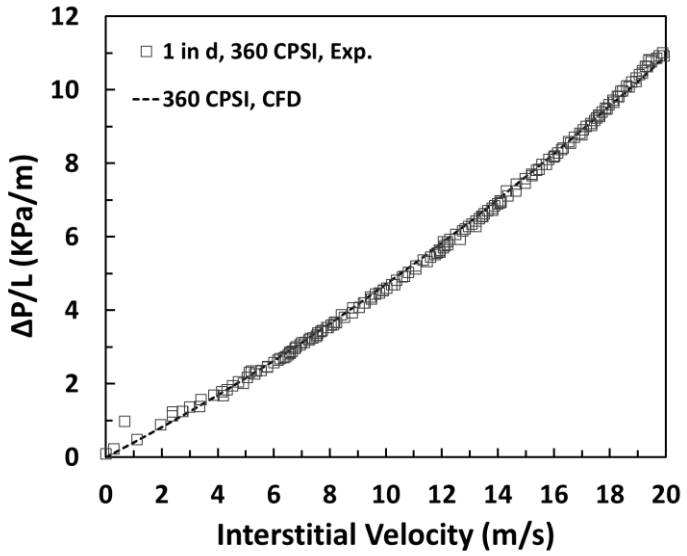

Figure 3.11 Pressure drop per unit length vs. interstitial velocity, Comparing experimental results with CFD model prediction for a 1in diameter corrugated structure with cell density of 360 CPSI.

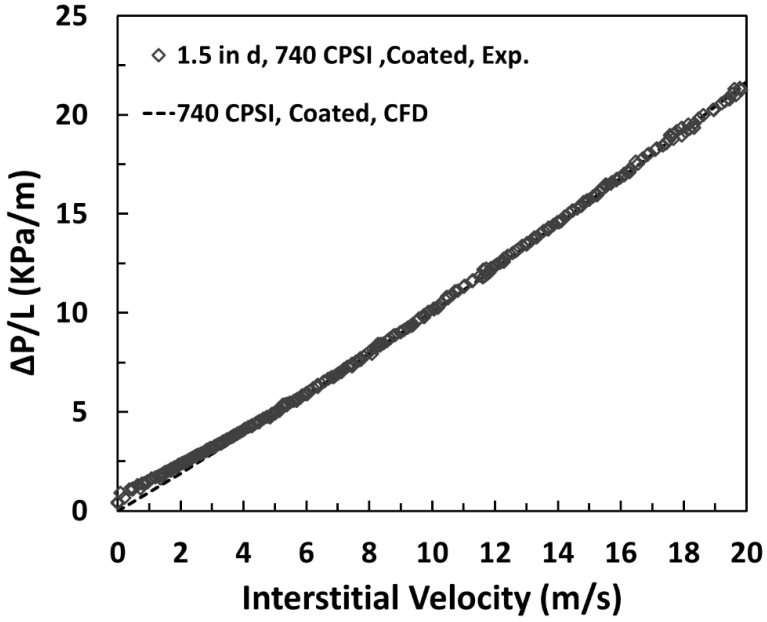

Figure 3.12 Pressure drop per unit length vs. interstitial velocity, comparing experimental results with CFD model prediction for a 1.5 in diameter corrugated structures with cell density of 740 CPSI coated with 31μm of 13X zeolite

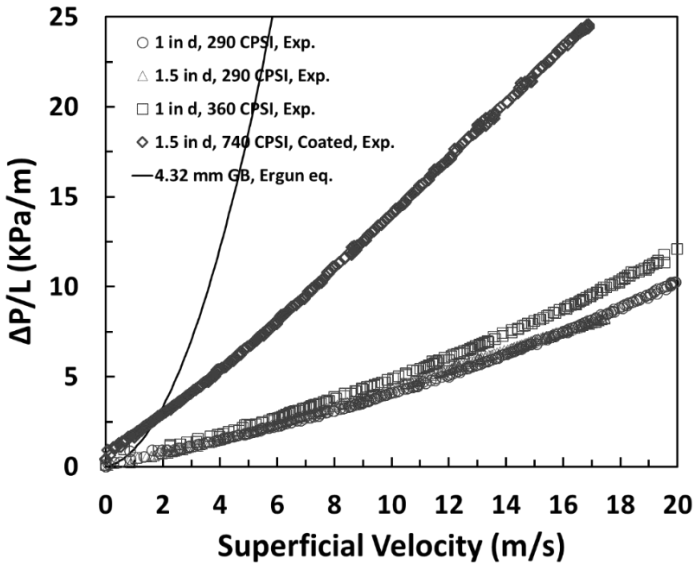

Figure 3.13 Pressure drop per unit length vs. superficial velocity, comparing experimental results for different corrugated structures with Ergun eq. prediction for a bed packed with 4.32mm diameter glass beads.

CHAPTER 4

CO_2 CAPTURE FROM FLUE GAS BY A PSA PROCESS USING A NOVEL STRUCTURED ADSORBENT

4.1 SUMMARY

A novel structured adsorbent was developed and studied experimentally and numerically for CO_2 capture from flue gas. A 3-bed 7-step continuous feed pressure swing adsorption (PSA) cycle schedule was devised for producing CO_2 with desired purity ($\geq$ 90 vol%) and recovery($\geq$ 90 vol%) using 13X zeolite adsorbent. A corrugated structured adsorbent with triangular channels coated with a layer of 13X zeolite offering low pressure drop was manufactured for this specific study. DAPS equipped with Darcy-Forchheimer pressure drop expression specially tuned for the structured adsorbent was used in preliminary studies and it was shown that the structured adsorbents was able to achieve the desired performance with as low as 241.79 kg/m^3 adsorbent bulk density. A complex single bed setup enable of mimicking all the steps of a multi bed cycle was then equipped with the structured adsorbents. Breakthrough experiments were carried out to study the dynamic behavior of the cores and to find out the adsorbent bulk density to be 151.08 kg/m^3. A set of experiments tested the designed PSA cycle with the newly developed adsorbent. Promising results for recovery ($\geq$ 93.0 vol% in all cases except one) was obtained but in spite of efforts to increase the purity the highest value achieved was 91.31 vol%. Experimental results were validated with accuracy using DAPS concluding that the

adsorbent bulk density was too low to produce high purity CO_2 and that by increasing the adsorbent layer thickness this issue can be resolved. A step by step scale up procedure was followed and the scaled up system was investigated using validated DAPS. In spite of low pressure drop (<20 kPa) during the feed step the scaled up system achieved 90.05 vol% purity and 70.02 vol% recovery which are surprisingly low specially for recovery, further study showed that since the pressure drop is dominantly viscous in structured adsorbents and in packed beds at low pressures, smaller characteristic channel size of structured cores compared to packed beds leads to higher pressure drop during regeneration steps i.e. CnD and LR, which in turn results in lower performance. These results indicated that although structured adsorbents are an excellent choice for high pressure applications, they encounter inherent limitations under vacuum conditions. It was shown that reducing the bed size by increasing the number of units along with increasing the regeneration time by increasing the total cycle time resolved the problem and the desired performance was achieved.

4.2 INTRODUCTION

The production and subsequent release of carbon dioxide into the atmosphere, no matter the source, is becoming an increasingly serious issue with respect to its effect on global warming (**White et al. 2003**). As one of the more familiar greenhouse gases, carbon dioxide has the ability to warm the planet by trapping energy radiated from the surface of the earth that would otherwise be released to space. One of the major sources of carbon dioxide release into the atmosphere is through the burning of fossil fuels for energy, which unfortunately makes it ubiquitous (**Reynolds et al. 2008**).

One possible way is to completely substitute fossil fuels with renewable sources of energy. However, it has been estimated that coal will still supply 28% of the world's energy

demands in 2030 (**Haszeldine 2009**). Therefore, the interim measure advocated for reducing CO_2 emissions is its capture and storage.

A considerable effort is underway worldwide to curb CO_2 emissions from coal fired and other fossil fuel based power plants, because these plants are responsible for over 40% of the carbon dioxide emissions in the USA alone (**Ebner and Ritter 2009**).

Post-combustion flue gas from coal-fired power plants contains 12–15 mol % CO_2 at atmospheric pressure. The capture units are expected to concentrate the CO_2 from flue gas with purity and recovery exceeding 95 and 90%, respectively. The current leading separation process to perform CO_2 capture from post-combustion flue gases is amine scrubbing. Monoethanolamine (MEA) is the most common chemical solvent employed to capture CO_2. MEA scrubbing technology has already started its scale-up, although still is a technology with high energy penalties. Amine scrubbing for CO_2 capture presents a series of important drawbacks as the degradation of the solvent in the presence of oxygen, high energy demand for solvent regeneration, solvent loss by evaporation, equipment corrosion and formation of potentially carcinogenic nitrosamines (**Ribeiro et al. 2013, Krishnamurthy et al. 2014**).

Various capture approaches are being considered as an alternative to amine scrubbing such as membranes, cryogenic, adsorption and others, among these CO_2 capture by vacuum pressure swing adsorption (VPSA) is a promising option for separating CO_2 from flue gas since it has a number of advantages, such as possible low energy requirement, low capital investment cost and easy to achieve automated operation.

Table 4.1 provides an extensive summary of the performances of various PSA cycles investigated for removing and concentrating CO_2 from flue gas. A comprehensive

review of relevant studies that deal with CO_2 capture from flue and stack gases by PSA processes has been given by **Ritter and co-workers (2006, 2009).**

In recent years**, Xiao et al. (2008)** in an experimental study of a three-bed VSA achieved a CO_2 recovery of 90% and purity of 80% from dry flue gas containing 12% CO_2 using zeolite 13X as the adsorbent.

Furthermore, a CO_2 recovery of 70% with more than 90% purity and low power cost (4–10 kW/TPDc) was reported by **Zhang and Webley(2008)** when dealing with 40 C flue gas by nine- step three-bed VPSA pilot-scale plant under a relatively deep vacuum of 5 kPa for desorption of adsorbents.

Liu et al.(2012) used zeolite 5A to study the capture and concentration of CO_2 from a dry flue gas using a three-bed, seven-step PVSA process. The major steps involved in their process were pressurization, high pressure adsorption, concurrent depressurization, heavy product rinse, blowdown, purge, and pressure equalization. With this cycle configuration, 79% of the CO_2 was captured with 85% purity. The overall energy consumption of this process was 2.37 MJ kg^{-1} of CO_2 captured (656 kWh $tonne^{-1}$ CO_2 captured).

Activated carbon and zeolites have been the main commercial adsorbents used for CO_2 capture studies. The capacity of zeolites for CO_2 is higher than that of activated carbon. However, it should be noted that zeolites are highly sensitive to water in the flue gas, which is strongly adsorbed and difficult to remove. To simplify laboratory-scale experiments and simulation works, mixture streams of CO_2 and N_2 and/or O_2 have usually been employed to mimic actual flue gas.

The objective of this work is to devise a large scale PSA system for CO_2 capture from flue gas. In order to overcome the pressure drop issues faced in this high throughput application a novel structured adsorbent was developed and studied experimentally and numerically. First a 3-bed 7-step PSA cycle schedule was devised to produce CO_2 with more than 95 vol% purity and more than 90 vol% recovery using 13X zeolite adsorbent. A corrugated structured adsorbent coated with a layer of 13X zeolite was manufactured for this specific work and then DAPS equipped with Darcy-Forchheimer pressure drop expression was used in preliminary studies to show that the desired performance could be achieved even with low bulk densities. A complex single bed setup was then equipped with the structured adsorbent bed and breakthrough experiments were carried out to study the dynamic behavior of the cores and to find out the effective adsorbent bulk density. A set of experiments tested the designed PSA cycle with the newly developed adsorbent achieving promising results for recovery with lower than desired purity. Experimental results were validated with DAPS concluding that the bulk density was too low and the void fraction too high resulting in low purity. Considering the preliminary study this issue can be resolved by increasing the adsorbent layer thickness. The system was then scaled up and investigated using validated DAPS. Results were surprisingly low for recovery, further study showed that the pressure drop during regeneration steps leads to the low performance and that the structured adsorbents should be used with cautious under vacuum conditions. It was then proven that reducing the bed size by increasing the number of units along with increasing the regeneration time by increasing the total cycle time can resolve the problem and the desired performance could be achieved.

4.3 PSA CYCLE SCHEDULE

Figure 4.1 (a) displays the 3-bed 7-step PSA cycle schedules in terms of the bed interconnects and **Figure 4.1 (b)** presents the corresponding PSA cycle schedule in terms of relative cycle step durations.

The cycle step sequence for the 3-bed 7-step PSA processes includes Feed (F), HR, EqD, CnD, LR, EqU and light product pressurization (LPP) steps. To ensure a continues feed cycle the F step time is one third of the total cycle time.

During the F step, a bed is fed at the high pressure with the feed mixture. During the F step the heavy component (i.e., CO_2) which has higher affinity towards the adsorbent and larger equilibrium loading is retained in the adsorbed phase in the bed, principally at the feed (or heavy) end, while a stream enriched with the lighter component (i.e., N_2) leaves the other end of the bed and is recovered as the light product.

HR step which is coupled with LR step, recycles the heavy-product gas obtained from LR back to the high-pressure column. This gas, which already is enriched in the heavy component, displaces the light component from the adsorbed phase near the heavy product or feed end of the column and flushes it downstream toward the light-product end of the column, effectively filling both the adsorbed and gas phases in the column specially the region close to the heavy end, with the heavy component, while continuing to produce a pure light product. Much, if not all, of this heavy reflux gas is recovered during the subsequent CnD step resulting in a heavy product that is more enriched in the heavy component.

During the Eq step two beds are connected through their light ends with their heavy ends closed and allowed to equalize in pressure, any Eq step is thus a coupled cycle step.

The purpose of a Eq step is to remove the lighter component from the void spaces near the light end of the bed while filling the void spaces with the heavy component due to desorption, which, in turn, increases the purity of the heavy species during the subsequent CnD step. An additional role of any Eq step is to recycle gas that is not suitable to take as product, while also partially pressurizing another bed. The CnD step is carried out by depressurizing g the bed to the low pressure countercurrently through the heavy end while keeping the other end of the bed closed. The CnD step is a regeneration step, where the heavier species, now enriched relative to its feed concentration, is removed from the bed as the heavy product.

LR step utilizes a portion of the light-product gas produced during F step to purge a column at low-pressure after the CnD step. This gas, which mostly consist of light component, enters the column at its light end and displaces the remaining heavy component from the adsorbed phase and flushes it downstream towards the heavy end, producing a gas rich in heavy component which is then sent to a column undergoing the HR step. LR step effectively removes the heavy component from both the gas and adsorbed phase in much of the column. Since a part of the F step product is used in LR, these two steps are coupled.

The EqU step is carried out with the bed undergoing the EqD step, with both beds connected through their light ends. The purpose of the EqU step is to flush some of the heavy component toward the heavy end of the bed due to the pressure being low at first, while also allowing some of the light component to become adsorbed near the light end of the bed, all while partially pressurizing the bed.

The LPP step is the final step in this PSA cycle step sequence. It is carried out by using a fraction of light product gas produced in the last fraction of F step to pressurize a bed just finishing the EqU step up to the high (feed) pressure through its light end with its heavy end closed. The purpose of the LPP step is similar to the EqU step. Moreover, to avoid the use of a feed surge tank and from a PSA cycle schedule point of view, it is prudent to use a LPP step instead of the FP step practiced exclusively in the literature **(11-14)**. The F and LPP steps are also coupled cycle steps. The bed just finishing the LPP step is now ready to begin a new cycle with the F step.

4.4 EXPERIMENTAL SETUP

The schematic diagram of the 1-bed PSA apparatus is shown in **Figure 4.2**. At its heart lies a single bed equipped with three six inch long 13X zeolite coated cores. Two sections filled with 3mm glass beads at the top and bottom entrance of the column act as flow distributor. Three exposed tip k-type thermocouples were set up to touch the outer metallic wall of the structured adsorbent at three different points along the bed and record the temperature during the process. Six heating bands connected to six separate variacs were used to set the bed temperature during the PSA process or overnight regeneration steps. Column and heating bands were wrapped with insulating fiber to reduce the heat loss. Column pressure was measured with two pressure transducer with different ranges placed at the bottom of the bed, one for medium to high pressures (Swagelok 0-25 bar) and a low range transducer (Omegadyne Inc. 0-15 psia) specifically for vacuum pressures.

Four mass flow controllers (Brooks 5850E for low N_2 flow, Tylan FC-280S for high N_2 flow, Tylan FC-280S for CO_2 flow and Tylan FC-280S for He flow) each connected to the designated high purity (>99.99%) gas cylinder obtained from Praxair,

provided the system with flows required in different cycle or regeneration steps. Using the appropriate ratios, streams of CO_2 and N_2 from different flow controllers were mixed together to create certain gas compositions for feed, heavy and light reflux streams. For instance for feed flow, CO_2/ N_2 ratios were chosen in a way that the mixed stream composition resembles the composition of flu gas from a typical coal fired power plant. In addition to mass flow controllers, two mass flow meters (Hasting model 201 for light product and Tylan FC-280S for heavy product) were used to measure e the flow of the heavy and light products obtained from the process.

Three equalization tanks were used to mimic the bed-to-bed pressure equalization step. During equalization step pressure of the bed is reduced (for equalization down) or increased (for equalization up) in three stages by equalizing with each tank separately. To monitor the pressure, each tank is equipped with a pressure transducer.

Two product tanks were installed to collect the products, one for the light product and the other for the heavy product. The system is capable of analyzing both average and instantaneous concentration of the products. The average concentration of the product can be determined by analyzing the gas from the light or heavy product tank whereas the instantaneous concentration can be obtained by bypassing the product tanks. Increase or decrease in the product tank pressure by adding or withdrawing product can be followed by a pressure transducer designated to each tank.

Three GAST (DAA series) vacuum pumps connected in parallel can generate a deep vacuum whenever it is required in the process enabling the set up to run VPSA cycles in addition to PSA cycles. The composition of different streams were analyzed instantaneously using SRS RGA200 mass spectrometer.

The sections described here along with a network of connecting lines equipped with several automated solenoid valves, manual three way and needle valves give the system the flexibility to mimic multi bed systems and run any possible combinations of complex PSA cycle steps carried out in multi bed set ups.

4.5 STRUCTURED CORE AND ADSORBENT CHARACTERISTICS

As shown in **Figure 4.3** structures provided by Catacel that were used in this study are constructed by wrapping a thin corrugated layer of metal foil around a central rod resulting in cylindrical structures with numerous triangular channels. Cross section of each channel is assumed to be an equilateral triangle. Structured cores were coated with a thin layer of 13X zeolite adsorbent. The thickness of the coated layer was verified by running breakthrough experiments and then matching the experimental results with simulation using different adsorbent layer thicknesses. **Figure 4.4** shows the experimental breakthrough curve compared to DAPS simulation results. . In order to match the breakthrough time the adsorbent layer thickness was set to 31 microns resulting in adsorbent mass that was in good agreement with values reported by manufacturer considering the water capacity of the zeolites. The shoulders observed in the experimental curve are due to gaps between the core and bed wall and imperfections in the core structure that leads to early breakthrough of CO_2. The reason for breakthrough curve's spread shape is the heterogeneity of the channels, channels have differences in size, shape and adsorbent loading that has an effect similar to dispersion which spreads the breakthrough curve, to account for this, in breakthrough simulation the mass transfer coefficient was artificially decreased to values much lower than real mass transfer coefficient that have been confirmed with both other techniques such as frequency response and also simulations

matching experimental results discussed in later sections. It was also observed that simulating PSA cycles using the artificial mass transfer coefficient resulted in very low performances which is in contradiction with experimental results for the same cycles. Characteristics of bed, corrugated structure and the breakthrough experiment parameters are summarized in **Table 4.2** and **Table 4.3** respectively.

The commercial adsorbent used for coating the structured core was supplied by Grace (Sylobead grade 544 zeolite).Pure component adsorption equilibrium isotherms for CO_2, N_2, and O_2 on zeolite 13X were measured at three different temperatures (25, 50, 75 °C) by using a volumetric system from micromeritics (ASAP2010, located at the University of South Carolina). The equilibrium adsorption isotherm parameters for CO_2, N_2, and O_2 on zeolite 13X were obtained by fitting the Three Process Langmuir model simultaneously at all three temperatures to the experimental data. **(Mohammadi et all 2016)**

The LDF mass transfer coefficients for CO_2, N_2, and O_2 in zeolite 13X were measured in-house using a volumetric frequency response (VFR) apparatus over a wide range of frequencies from 10^{-5} to 10 Hz and at four different temperatures, i.e. 20, 30, 40 and 50 ^oC.[ref] The VFR results were fitted to **Equation 4** .

The adsorbent characteristics along with the adsorbate equilibrium and kinetic properties are listed in **Table 4.2**.

4.6 MATHEMATICAL MODEL

The performance of each PSA cycle was determined via simulation using a dynamic adsorption process simulator (DAPS) (**Reynolds et al. 2006**). DAPS is written in FORTRAN and uses finite differences along with the time adaptive DAE solver called

DASPK (**Brown et al., 1994**). The following assumptions are imposed in DAPS: ideal gas, isothermal operation, 1-D plug flow (i.e., no radial concentration), no axial dispersion, the gas phase concentration in the pores of the adsorbent is equal to that in the pores of the column, axial pressure drop along the column is described by Darcy-Forchheimer equation with friction factor specifically developed for structured adsorbents with triangular channels and the mass transfer between the gas and solid phases is described by the linear driving force (LDF) approximation.

For an N-component system, the overall and component mass balances over a differential volume element respectively yields

$$\left(\varepsilon_b + \left(1-\varepsilon_b\right)\varepsilon_a\right)C_T\left(\frac{1}{P}\frac{\partial P}{\partial t}\right) + \varepsilon_b \frac{\partial v C_T}{\partial z} + \sum_{j=1}^{n} S_j = 0 \tag{1}$$

$$\left(\varepsilon_b + \left(1-\varepsilon_b\right)\varepsilon_a\right)C_T \frac{\partial y_i}{\partial t} + \varepsilon_b C_T v \frac{\partial y_i}{\partial z} - y_i \sum_{j=1}^{n} S_j + S_i = 0 \qquad i = 1 \text{ to } N\text{-}1 \tag{2a}$$

$$y_i + \sum_{j=1, j\neq i}^{n} y_j = 1 \qquad i = N \tag{2b}$$

with

$$C_T = \frac{P}{RT};\ S_i = (1-\varepsilon_b)\rho_a \frac{\partial q_i}{\partial t}$$

ε_a and ρ_a are the adsorbent layer porosity and density, ε_b is the bed porosity, v is the interstitial velocity, y_i is the mole fraction of component i in the gas phase, T is the temperature, P is the pressure and q_i is adsorbed phase loading of component i.

Bed porosity in the studied corrugated adsorbents with equilateral triangular channels was calculated using following equation

$$\varepsilon_b = \frac{a^2}{(a + \sqrt{3}(\delta_m + 2\delta_a))^2} \tag{3}$$

With

$$a = \frac{2 * 0.0254}{\sqrt{\sqrt{3}C_D}} - \sqrt{3}(\delta_m + 2\delta_a)$$

Where a is the triangular cells side length, δ_m and δ_a are metal foil and coated adsorbent layer thickness respectively and C_D is cell density representing cells per unit area of cross section.

The mass transfer rate of component *i* between the gas and solid phases is described by the following LDF expression

$$\frac{\partial q_i}{\partial t} = k_i\left(q_i^* - q_i\right) \qquad i = 1 \text{ to } N \qquad (4)$$

Where k_i is the mass transfer coefficient of component *i*,

The equilibrium loading q_i^* of component *i* is calculated from the multicomponent form of the triple process Langmuir (TPL) isotherm model in the perfect positive formulation according to **Ritter et al. (2011) and Bhadra et al. (2012)**

$$q_i^* = q_{1,i}^s \frac{b_{1,i} P y_i}{\left[1 + \sum_{j=1}^{N} b_{1,j} P y_j\right]} + q_{2,i}^s \frac{b_{2,i} P y_i}{\left[1 + \sum_{j=1}^{N} b_{2,j} P y_j\right]} + q_{3,i}^s \frac{b_{3,i} P y_i}{\left[1 + \sum_{j=1}^{N} b_{3,j} P y_j\right]} \qquad (5)$$

Where the temperature dependences of parameters $b_{1,i}$, $b_{2,i}$ and $b_{3,i}$ are given by

$$b_{1,i} = b_{1,i}^0 exp\left(\frac{B_{1,i}}{T}\right) \qquad (6)$$

$$b_{2,i} = b_{2,i}^0 exp\left(\frac{B_{2,i}}{T}\right) \qquad (7)$$

$$b_{3,i} = b_{3,i}^0 exp\left(\frac{B_{3,i}}{T}\right) \qquad (8)$$

$B_{1,i}$, $B_{2,i}$ and $B_{3,i}$ are the isosteric heats of adsorption for component *i* on sites 1,2 and 3.

The pressure drop along the column is evaluated via the Darcy-Forchheimer equation with friction factors specifically obtained for structured adsorbents with triangular channels

$$\frac{\partial p}{\partial z} = -f_D(Re).\rho\frac{v^2}{2D_h} \tag{9}$$

ρ is the average density of the gas phase at each point along the structured bed, f_D is the Darcy friction factor and is expressed in the following form

$$f_D(Re) = f_1 + \frac{f_2}{Re} \tag{10}$$

Where the friction factor parameters f_1 and f_2 are $5.00646*10^{-6}$ and $5.08388*10^{-2}$ respectively. The Reynolds number and hydraulic diameter for equilateral triangular channels are described as

$$Re = \frac{\rho v D_h}{\mu} \tag{11}$$

$$D_h = \frac{\sqrt{3}a}{3} \tag{12}$$

Where μ is the average viscosity of the gas phase at each point along the channel.

For an N-component system, there are 2N+2 variables and equations that have to be solved at each node. The initial conditions of any particular cycle step correspond to the prevailing conditions at the end of the previous cycle step. The initial and boundary conditions are summarized in Supplemental **Table 4.9**. These represent the equations used in the first (z/L = 0) and last (z/L = 1) nodes of the bed with L being the bed length. At given boundaries the molar flow rate F through a valve is described by the valve equation according to

$$F = C_v v\frac{1}{\sqrt{S_g T}} min(49.08|P^2 - P_o^2|^{0.5}, 41.63P_o) \tag{13}$$

where C_v is the valve coefficient, S_g is the specific gravity of the gas relative to air at 1 atm and 21.45 °C, P_o is the pressure downstream of the valve, and the expressions within the min function account for either non-choking or choking conditions. It is important to note that C_v in **Eq. (13)** is dimensionless when flow, pressure and temperature are expressed in units of SLPM, kPa and K, respectively. When concentrations, flow rates, temperatures and valve equations are not specified or required, consistency at the boundary is maintained by utilizing the corresponding balances identified in **equations (1) ,(2), (4) and (9).**

The performance indicators of the PSA process are evaluated in terms of CO_2 purity in heavy product, CO_2 recovery in heavy product and feed throughput θ, which are defined as

$$\%\ Purity = \frac{moles\ of\ CO_2\ product\ produced\ during\ CnD}{total\ moles\ of\ product\ produced\ during\ CnD} * 100 \quad (14)$$

$$\%\ Recovery = \frac{moles\ of\ CO_2\ product\ produced\ during\ CnD}{moles\ of\ CO_2\ fed\ to\ the\ bed\ during\ F} * 100 \quad (15)$$

$$\theta\left(\frac{L(STP)}{h * kg}\right) = \frac{gas\ fed\ to\ one\ bed\ during\ F\ in\ one\ cycle}{mass\ of\ adsorbent\ in\ one\ bed * total\ cycle\ time} \quad (16)$$

4.7 RESULTS AND DISCUSSION

A preliminary simulation study was carried out to investigate the possibility of enriching CO_2 in a bench scale to required purity (≥95 vol%) and recovery (≥90% vol%) by DOE with much lower than packed bed bulk densities associated with structured adsorbents. Bed, structured core, adsorbent and process parameters for these simulations are summarized in **Table 4.4.** Two different cell density each with a different thickness of adsorbent layer was chosen resulting in 406.49 and 241.79 kg/m^3 bulk densities while keeping the triangular channel size in the same range. These bulk densities were chosen

with the former being the target density to achieve with the actual structured cores and the latter to test the lower limits of bulk density in structured cores with almost one third of conventional packed bed bulk density. The periodic state process performances obtained for each structured core in a range of throughputs are shown in **Figure 4.5** and are summarized in **Table 4.5.** The process performances are reported in terms of CO_2 purity, CO_2 recovery and feed throughput (θ) as defined in **Equations 14, 15** and **16**.

Figure 4.5(a) reveals the effects of the feed throughput (θ) and adsorbent bulk density on the CO_2 purity and CO_2 recovery obtained from the 3-bed 7-step PSA cycle schedule. The recovery always decreases with increasing feed throughput. In contrast, the purity always increases with increasing feed throughput with it tapering off at higher values of θ for 241.79 kg/m^3 bulk density. **Figure 4.5(a)** and **(b)** show that it was possible to obtain a CO_2 purity > 95 vol% at CO_2 recoveries > 90% even with bulk densities as low as 241.79 kg/m^3 at high θ attainable in structured adsorbents due to their inherently lower pressure drops. However higher bulk densities result in better performance and achieving desired recovery and purity started to become challenging at lower bulk densities.

The effect of the feed throughput on recovery is caused by insufficient bed regeneration, because increasing θ while keeping the cycle time constant is achieved by increasing the feed flow rate, this means more feed is fed to a bed without changing the durations of any of the regeneration steps leading to inadequate regeneration of the bed unable to overcome the higher feed flow.

The effect of θ on purity is explained as follows. At larger θ a larger portion of the bed is saturated at the feed conditions. This results in the higher purities being attained at the larger θ but as explained before with the lower recoveries, when decreasing θ the purity

also decreases, which shows a smaller portion of the bed is saturated and the bed is essentially being underutilized near the light end. But, of course, the recovery keeps increasing.

The higher bulk density leads to more adsorbent and therefore more loading of adsorbed phase per unit volume of the bed, which causes a more enriched in heavy component gas phase to be produced during desorption and consequently results in a higher purity of heavy component in heavy product at every throughput compared to the lower bulk density.

The discussed simulation results show that it is theoretically possible to achieve desire purity and recovery for CO_2 with the 13X zeolite structured adsorbent contactor, the next step is to test the corrugated cores and evaluate their performance experimentally. Single bed apparatus described in previous sections was utilized to perform the designed experiments. The bed, structured core, adsorbent and process parameters for the experimental study are presented in **Table 4.2** and **Table 4.3.**

In order to decrease the complexity instead of using tanks and gas recycling in the experimental runs pure N_2 was used as a substitute for the light product to feed the LR and LPP steps. Simulation results were used to estimate the flow of the light product and subsequently the inlet flow to the LR and LPP steps. Composition and the flow of the LR step outlet stream which then feeds heavy reflux step were also obtained via simulation. The periodic state process performances obtained for experimental runs are shown in **Table 4.6.** Several throughputs, different total cycle and step times and two temperatures were tested experimentally to cover a wide range of operating conditions. As shown in **Table 4.6** target CO_2 recovery (>90 vol%) in HP was achieved but in spite of increasing the

throughput for instance in run 4 to basically saturate the bed and ensure maximum purity which results in major breakthrough of CO_2 into the light product and a significant decrease in the recovery, the maximum purity obtained was 91.31 vol%. Since the bulk density of the adsorbent in the structured cores used in experimental runs was 151.08 kg/m^3 which is much lower than the target density of 400 kg/m^3 and even the lowest density studied in the preliminary simulations (241.79 kg/m3), with the same argument about the effect of bulk density on HP purity, discussed in previous sections, it can be concluded that low purities of HP were due to low bed density and high void volume.

Next step was to validate the mathematical model against the experimental results. **Table 4.6** compares each experimental results with the results obtained from the corresponding simulation carried out in DAPS. As shown in the table, DAPS was able to predict the experimental results with a very good agreement except for the recovery of run 4. The difference in the experimental and simulation recovery of run 4 can be explained with heterogeneity of the channels, as explained in the breakthrough experiment section, channels have differences in size, shape and adsorbent loading that has an effect similar to dispersion and spreads the breakthrough curve, by increasing the throughput and pushing the adsorption front towards the end of the bed this spread curve causes the heavy component to breakthrough into the light product much more than a case with a sharper adsorption front, as discussed before since this spread is caused by channel imperfections and not mass transfer limitations the simulation front is much less spread and the heavy component doesn't breakthrough as much as the corresponding experiment, which leads to the differences in the recovery for run 4. As shown in the results this phenomena does not affect the results when the front is not to close to the end of the bed and also it can be

minimized by better and more careful manufacturing and reducing the imperfections of the structured adsorbent.

The accuracy and consistency of the DAPS over a wide range of conditions validates the model and allows the simulation code to be used for further studies with confidence. Also achieving the desirable performance with the same model using higher bulk densities proves that in the experimental runs the adsorbent densities were too low to get high enough purity in the HP.

Figure 4.6 presents the periodic state temperature history for five consecutive cycles of run 5 recorded by the thermocouple located at the central location along the bed and touching the outer metal wall of the corrugated structure. In conventional zeolite packed beds high interaction between CO_2 and adsorbent causes temperature swings in the order of tens of degrees but surprisingly as seen in the figure the temperature fluctuation resulted from adsorption and desorption steps are less than 0.5 C. Minimal temperature fluctuations can be explained as follows. Highly heat conductive corrugated metal foil used in the manufacturing of the cores that in this case makes 12% of the total volume of the bed absorbs and disperses the heat so quickly that it makes the process operate almost isothermally, this also verifies the isothermal approach to the mathematical modeling of the system.

After validation of the model, the next step is to scale up the design and develop a system able to deal with high flows of flu gas encountered in coal-fired power plants. A systematic and step by step method was implemented to make sure that the scale up process is carried out properly meaning that the scaled up system behaves as similar as possible to the original system while satisfying the design requirements.

Considering the two systems studied in preliminary simulations and due to better results the system with 406.49 kg/m^3 effective bulk density with throughput of 3000 (L_{STP}/h/kg) was chosen for scale up. The first condition in scaling up is to keep the throughput of the large system the same with the small scale system, this ensures that the same amount of feed is processed during each cycle by a unit mass of the adsorbent and that the loading profile of the large bed after the feed step and therefore the subsequent steps are similar which can lead to similar performances. Next the flow of the flu gas in the large system was obtained by dividing the total flow of the flu gas produced in the plant between 20 parallel adsorption units. Since the flow of the flu gas required to be processed, the total cycle time and the density of the adsorbent in the structured cores are known the mass of the adsorbent and hence the volume of each bed in the scaled up system was calculated based on the definition of the throughput in **Eq. 16**. Next an arbitrary and reasonable height to diameter ratio of h/D = 0.85 was chosen and the height and diameter of the system were calculated. The flu gas flow rate fed to each adsorption unit, total cycle time and calculated bed height and diameter along with structured core and adsorbent characteristics are presented in **Table 4.7**.

For conventional beds packed with beads or granular adsorbent one of the main concern when scaling up is the adsorbent fluidization which can cause structural stress and gradual attrition, therefore maximum velocities during cycle steps should be calculated and made sure they don't exceed the fluidization velocity of the bed. In the case of structured adsorbents the adsorbent layer adheres to the support wall and this problem is not encountered which enables these adsorbents to deal with high gas velocities without the fluidization restriction.

The most noticeable difference between small and large adsorption beds and the most challenging problem faced in the scale up process which can cause significant dissimilarity in the dynamic and thus the performance of the two systems is pressure drop. High pressure drop not only imposes high operational costs but also negatively affects the performance of the system, therefore in the second step of the scaling up process the pressure drop of the system was evaluated and made sure that the pressure drop resulted from the calculated height didn't exceed the maximum pressure drop considered for the system which in this case is 20 kPa. Feed step deals with the highest flow in the cycle and hence the highest pressure drop occurs during this step. **Eq. 9** was used to evaluate the pressure drop during the feed step and it was found that with the considered height the pressure drop is less than 20 kPa which satisfies the pressure drop restriction.

After following the two discussed steps and determining the dimensions of the large scale system, DAPS was utilized to evaluate the performance of the scaled up system and analyze possible differences with the bench scale design. **Table 4.7** summarizes the bed, structured core and process characteristics used in the large scale simulations. Achieved 90.05 vol% purity and 70.02 vol% recovery which are surprisingly, much lower than the results obtained in the small scale studies, especially for the recovery with more than 20% difference.

By investigating the periodic state pressure profiles at the beginning and the end of each step during a full cycle, as shown in **Figure** 4.**7** it was found that the pressure along the bed during regeneration steps i.e. CnD and LR does not drop to the intended values and even at the end of the steps remains much higher than the design vacuum pressure of 5kPa.

This seems counterintuitive because the pressure drop issue is not encountered in packed beds under vacuum and structured adsorbents are known to offer less pressure drop compared to packed beds. To investigate this phenomenon, pressure drop for air flow at 25 C predicted by the Ergun equation (**Eq. 17**) used for packed beds was compared to the Darcy-Forchheimer equation (**Eq. 9**) used for structured adsorbents in a range of interstitial velocities and under two different pressure (and hence density) conditions of 101.325 and 5 kPa which represent high and low pressures encountered in the PSA cycle studied in this work. The same structured core as the one used in the large scale simulations and a bed with porosity of 0.4, packed with 5 mm in diameter zeolite beads were considered for pressure drop study. The pressure drop along the packed bed is evaluated via the Ergun equation as

$$\frac{\partial P}{\partial z} + 1.5\times10^{-1}\,\mu\left(\frac{1-\varepsilon_b}{2r_p\varepsilon_b}\right)^2 v + 1.75\times10^{-3} C_T M \frac{1-\varepsilon_b}{2r_p\varepsilon_b} v|v| = 0 \qquad (17)$$

Where μ and M are the viscosity and average molecular weight of the gas phase and r_p is the effective radius of the pellet.

Results are presented in **Figure 4.8** and as displayed in the figure, at higher pressure of 101.325 kPa the pressure drop faced in the packed bed as expected is much higher than the structured adsorbent and as the velocity increases the difference becomes more pronounced, this is the reason structured adsorbents are preferred to conventional packed beds in high throughput applications with high pressure drop, but interestingly at low pressure a different behavior is observed. The pressure drop in structured adsorbent seems to be almost independent of the pressure and higher than packed beds. This can be explained as follows, in the packed beds and thus the Ergun equation the inertial pressure

drop is dominant which is a strong function of density and results in the significant difference between Ergun prediction in low and high pressures, in contrary in structured adsorbents and therefore the Darcy-Forchheimer equation the viscous pressure drop is dominant which is independent of density and leads to almost overlapping pressure drop predictions for high and low pressures. Since the characteristic channel diameter of the packed bed is much larger than the structured adsorbent, during the regeneration steps and at low pressures that the viscous term plays the major role, the pressure drop faced in structured adsorbents is higher than packed beds preventing the bed to reach deep vacuum. Not being able to reach deep vacuum during regeneration steps leads to less desorption and insufficient regeneration of the bed which in turn decreases the bed's capacity during adsorption steps of Feed and HR, with reduced capacity the bed cannot maintain the same throughput and a significant amount of heavy component breaks through into the light product resulting in a noticeable drop in the recovery of the scaled up system.

In the initial stages of the CnD step the gas phase in the bed still has a considerable amount of light gas and thus the heavy product has lower purity, as more gas is removed from the bed and the desorption continues, the gas phase is enriched with the desorbed gas and the gas phase composition converges to the adsorbed phase composition which is enriched in heavy component, this causes the purity of the heavy product to keep increasing during the CnD step. The highest purities for heavy product in this step are achieved when the bed is at the lowest pressure but since as shown before, the large scale system doesn't reach the desired deep vacuum, the average purity of the heavy product is lower compared to the small scale system.

After arguing that the high pressure drop in the regeneration steps and therefore insufficient bed regeneration is be the main culprit for the low performance of the scaled up system, next is to investigate the effects of decreasing the pressure drop on the performance, one of the means to reduce the pressure drop is to decrease the height of the bed, so in the next study two systems with bed heights of half (1.34 m) and one fourth (0.67 m) of the original design were tested. In order to keep the height to diameter aspect ratio of 0.85, the diameter had to change too, which means more units i.e. 4 and 16, are needed respectively to process the same feed flow. To see the effect of the bed height on the pressure drop of the regeneration steps, pressure profiles at the end of CnD and LR steps for the shortest bed with 0.67 m in height is compared in **Figure 4.7** to the original scaled up design with the height of 2.67 m**.** Results show that decreasing the bed high significantly reduces the pressure drop and helps the beds to reach the desired deep vacuum. **Figure 4.9** displays the effect of bed height on the purity and recovery of CO_2 in the heavy product, the simulation results are also summarized in **Table 4.8**. Results indicate that as expected by reducing the bed height and thus the pressure drop along the bed in CnD and LR steps, better regeneration is achieved which in turn increases the beds capacity in adsorption steps and prevents the heavy component to breakthrough into the light product resulting in increased recovery. Also reaching deeper vacuum in CnD step enriches the gas phase in the bed with heavy component and leads to slightly higher purity heavy product.

By investigating the effects of the bed height on recovery and purity, it is clear that achieving high performances using beds with longer heights is quite challenging, so the system with 0.67 m long beds was chosen for further study to see if by tuning the operation conditions the desired performance could be achieved. Also another set of simulations were

carried out with total cycle time of 180 s to give the bed more regeneration time during CnD and LR steps by increasing each step time and thus the total cycle time by 50%. The periodic state process performances obtained for each cycle time in a range of throughputs are shown in **Figure 4.10** and are summarized in **Table 4.8. Figure 4.5(a)** reveals the effects of the feed throughput (θ) and total cycle time on the CO_2 purity and CO_2 recovery obtained from the 3-bed 7-step PSA cycle schedule. As expected the recovery always decreases with increasing feed throughput, but in contrast the purity always increases with increasing feed throughput. The effect of the feed throughput on recovery and purity have been discussed in details in the previous sections. By increasing the cycle time, in order to keep the loading conditions similar and preventing a major breakthrough and loss of recovery the feed flow has to be reduced to feed the same amount of moles during the feed step, this causes the throughput to decrease but as it can be seen in **Figure 4.5(a)** the throughputs are still quite high compared to packed beds. **Figure 4.5(b)** shows that it was only possible to obtain a CO_2 purity > 95 vol% at CO_2 recoveries > 90% with the total cycle time of 180 s. longer regeneration step times lets the bed pressure to drop closer to the design value of 5 kPa and leads to better regeneration and as discussed before this in turn results in higher purity and recovery, m oving the purity-recovery curve into the desired performance zone.

4.8 CONCLUSION

Utilizing both experimental and simulation tools a novel structured adsorbent developed for CO_2 capture from flue gas was extensively studied. To produce CO_2 with desired purity ($\geq$ 90 vol%) and recovery($\geq$ 90 vol%) using 13X zeolite adsorbent, a 3-bed 7-step continuous feed pressure swing adsorption (PSA) cycle schedule was devised. In

order to offer low pressure drop in this high throughput application, a corrugated structured adsorbent with triangular channels coated with a layer of 13X zeolite was manufactured. In a preliminary study it was shown that the structured adsorbents was able to achieve the desired performance with as low as 241.79 kg/m^3 adsorbent bulk density, in these simulations DAPS equipped with the Darcy-Forchheimer pressure drop expression for the structured adsorbent was used. Then the structured adsorbent was experimentally tested with a complex single bed setup enable of mimicking all the steps of a multi bed cycle. To study the dynamic behavior of the cores breakthrough experiments were carried out and the adsorbent bulk density was found to be 151.08 kg/m^3. The developed PSA cycle was then studied via a set of controlled experiments. In spite of efforts to increase the purity the highest value achieved was 91.31 vol% but promising results for recovery ($\geq$ 93.0 vol% in all cases except one) was obtained. DAPS was validated by accurately predicting the experimental results also illustrating that the low adsorbent bulk density was the reason for low CO_2 purity and that by increasing the adsorbent layer thickness this problem can be resolved. A methodical scale up procedure was carried out and the scaled up system was studied using the validated DAPS. Although the structured core shows low pressure drop (<20 kPa) during the feed step the scaled up system achieved surprisingly low recovery of 70.02 vol% with the purity of 90.05 vol%, further study showed that since the viscous pressure drop is dominant in structured adsorbents and also in packed beds at low pressures and because structured cores have smaller characteristic channel sizes compared to packed beds, structured adsorbents create higher pressure drops during regeneration steps i.e. CnD and LR, which in turn results in lower performances. Conclusion can be drawn that although structured adsorbents are an excellent choice for high pressure applications, they

encounter inherent limitations under vacuum which needs to be considered in the design process. It was then shown that this issue can be resolved and the desired performance can be achieved by reducing the bed size (i.e. increasing the number of the units) along with increasing the regeneration time (i.e. increasing the total cycle time).

4.9 TABLES

Table 4.1 Performances of Various Stripping Pressure Swing Adsorption Cycle Configurations Investigated for CO_2 Concentration from Flue Gas[a]

PSA Cycle Configuration		Operating Step Sequence[b]	Ads[c]	yf(%)	PCO2(%)	RCO2(%)	P1(kPa)	Θ(L STP /h.Kg)	K CO2 (1/s)	K N2(1/s)	Energy	T reg(K)	References
5-bed	5-step	F,HR,CnD,LR,LPP	HTlc	15	72.2	82.2	11.49	11.5	0.0058, 0.0006	0	–	–	Ritter
5-bed	5-step	F,HR,CnD,LR,LPP	HTlc	15	75.5	48.8	11.49	23.1	0.0058, 0.0006	0	–	–	Ritter
4-bed	4-step	F,HR,CnD,LPP	HTlc	15	82.7	17.4	11.49	14.4	0.0058, 0.0006	0	–	–	Ritter
5-bed	5-step	F,HR,CnD,LR,LPP	HTlc	15	98.7	98.7	11.64	5.8	0.029, 0.003	0	–	–	Ritter
5-bed	5-step	F+R,HR,CnD,LR,LPP	HTlc	15	98.6	91.8	11.64	5.8	0.029, 0.004	0	–	–	Ritter
4-bed	4-step	F,HR,CnD,LPP	HTlc	15	99.2	15.2	11.64	72	0.029, 0.005	0	–	–	Ritter
4-bed	4-step	F+R,HR,CnD,LPP	HTlc	15	99.2	15.2	11.64	72	0.029, 0.006	0	–	–	Ritter
3-bed	8-step	FP,F,CoD,R,N,HR,CnD,N	13X	16	99	45	6.67	2200	0.33	0	–	–	Yang
4-bed	8-step	FP,F,HR,LEE,CnD,LR,LEE,N	NaX	13	95	50	10	154.6	equation	equation	–	–	Uchida
2-bed	4-step	FP,F,CnD,LR	13X	10	70	68	4	126.8	0.02	0.1	0.217(kWh/Nm3 CO2)	–	Cho
2-bed	6-step	LEE,FP,F,LEE,CnD,LR	13X	10	82	57	6.67	119.3	0.02	0.1	0.211(kWh/Nm3 CO2)	–	Cho
3-bed	5-step	FP,F,HR,CnD,LR	13X	10	83	54	6.67	84.5	0.02	0.1	0.28(kWh/Nm3 CO2)	–	Cho
3-bed	8-step	FP,F,CoD,LEE,HPP,HR,CnD,LEE	AC	17	99.8	34	10.13	338.73	–	–	–	–	Ki Na
3-bed	7-step	FP,F,LEE,HR,N,CnD,LEE	AC	13	99	55	10	166.21	–	–	–	–	Ki Na
3-bed	8-step	FP,F,CoD,LEE,HPP,HR,CnD,LEE	13X	13	99.5	69	5.07	–	0.1	0.01	–	–	Yeo
2-bed	4-step	HPP,FP,CoD,CnD	13X	20	48	94	5.07	–	equlibrium	equlibrium	–	–	Chou
2-bed	5-step	HPP,FP,F,CoD,CnD	13X	20	43	88	5.07	–	equlibrium	equlibrium	–	–	Chou
3-bed	4-step	LPP,F,CnD,LR	13X	20	58	75	5.07	–	equlibrium	equlibrium	–	–	Chou
3-bed	6-step	LPP,FP,F,HR,CoD,CnD	13X	20	63	70	5.07	–	equlibrium	equlibrium	–	–	Chou
2-bed	4-step	FP,F,CnD,LR	13X	15	72	94	90	1631	equation	equation	2508.98 j/mol CO2	–	Biegler
1-bed	4-step	FP,F,CoD,CnD	13X	15	90	94	15	471	equation	equation	5973.08 j/mol CO2	–	Biegler
2-bed	4-step	LPP,F,CnD,LR	13X	15	52	66	10	401	0.11	0.5	–	–	Grande
3-bed	5-step	LPP,F,HR,CnD,LR	13X	15	83	66	10	289	0.11	0.5	1.43 KWh/Kg CO2	–	Grande
3-bed	6-step	F,LEE,CnD,LEE,LPP	13X	12	83	60	4	–	–	–	8 KW/Day.ton CO2	–	Chaffee
3-bed	9-step	F,LEE,HR,CnD,LEE	13X	12	95	60	5	–	experimental	experimental	10 kW/TPDc	–	Webley
3-bed	9-step	F,LEE,I,LEE,CnD,LEE,FP	13X	12	92.5	75	3	824	equation	equation	7 KW/TPD CO2	–	Webley
2-bed	6-step	F+HR,F,HR,CnD,LR	13X	15	95	80	85	58	0.1631	0.2044	637 kWh/tonne CO2	–	biegler
2-bed	8-step	F+HR,F,F+HR,LEE,CnD,LR,LEE	13X	15	90	85	50	115	0.1631	0.2044	465 kWh/tonne CO2	–	biegler
2-bed	4-step	F,H,CnD,C	13X	15	92.7		70	183	experimental	experimental	–	413.15	LU
1-bed	6-step	FP,F,H,CnD,LR,C	13X	15	93.6	92.2	10	478	equation	equation	–	363	Li
1-bed	6-step	FP,F,H,CnD,LR,C	13X	15	94.4	98.5	3	437	equation	equation	–	363	Li
2-bed	4-step	FP,F,CnD,LR	HTLc	15	99.9	79	110	105	0.0088,0.00091	0	230 kWh/ton of CO2	–	Othman
2-bed	6-step	F+HR,LEE,CnD,LR,LEE,I	13X	20	99.48	99.3	34.4	516	0.808	0	170.2 kWh/ton of CO2	–	Rao
3-bed,2-bed	5-step, 6-step	FP,F,HR,CnD,LR FP,F,LEE,CnD,LR,LEE	5a	15	96.05	91.05	15.2	52.3	–	–	645.7 kJ/kgCO2	–	Rodrigues
3-bed	12-step	FP,F,LEE,CoD,LEE,I,CnD,I,LEE,I,LEE,LPP	AC	13	99.6	92.8	1	198	equlibrium	equlibrium	0.139 kWh/kgCO2	–	Delgado
1-bed	2-step	F+C,LR+H	5a	10	95	81	100	363	0.1	0	3.23 MJ/kgCO2	433.15	Clausse
3-bed	7-step	F,CoD,HR,LEE,CnD,LR,LEE	5a	15	85	79	5	149	–	–	2.37 MJ/kgCO2	–	Yu
1-bed	3-step	FP,F,CnD+H	AC	17	43	97	0.005	258	experimental	experimental	–	323	Pevida

2-bed,2-bed	4-step,5-step	FP,F,CnD,LR FP,F,LEE,CnD,LEE	AC	15	96.4	80.42	5	172	194.925	142.38	831.53 kJ/kg-CO2	–	Yu

[a]Here, the process performance has been judged primarily in terms of the CO_2 purity in the heavy product (PCO2(%)), with the CO_2 recovery (RCO*2*(%)) and the feed throughput (θ) being secondary but also important process performance indicator. [b] Cycle-step abbreviation legend: CnD, counter-current depressurization; CoD, co-current depressurization; FP, feed pressurization; F, high-pressure feed; HPP, heavy product pressurization; HR, heavy reflux; LEE, light-end equalization; LPP, light-product pressurization; LR, light reflux; N, null or delay; and R, recycle. *c* Adsorbent abbreviation legend: 13X, 5a and NaX, molecular sieve zeolites; AC, activated carbon; and HTlc, K-promoted hydrotalcite.

Table 4.2 Experimental bed, structured core and adsorbent characteristics along with adsorbate equilibrium and kinetic properties.

Structured Core Characteristics	
Core diameter (m)	0.0381
Single core length (m)	0.1524
Bed length (m)	0.4572
Cell density (CPSI)	741
Adsorbent layer thickness (m)	3.1×10^{-5}
Metal foil thickness (m)	5.2×10^{-5}
Core porosity	0.74
Adsorbent bulk density (kg/m^3)	151.08
Average side length of triangular channels (m)	1.22×10^{-3}
Average hydraulic diameter of triangular channels (m)	7.05×10^{-4}
Adsorbent Characteristics	
Adsorbent	13X zeolite
Adsorbent layer density (kg/m^3*)*	1110
Adsorbent layer porosity	0.54
Equilibrium and Kinetic Properties	
$B_{1,i}$ for CO_2, N_2, , O_2 (K)	5771.89, 2370.54,
$B_{2,i}$ for CO_2, N_2, , O_2 (K)	4614.19, 0.0, 0.0
$B_{3,i}$ for CO_2, N_2,, O_2 (K)	4222.59, 0.0, 0.0

$b^0_{1,i}$ for CO_2, N_2, , O_2 (kPa^{-1})	2.367×10^{-8}, 7.599×10^{-7}, 4.077×10^{-6}
$b^0_{2,i}$ for CO_2, N_2, , O_2 (kPa^{-1})	4.496×10^{-8}, 0.0, 0.0
$b^0_{3,i}$ for CO_2, N_2, , O_2 (kPa^{-1})	1.475×10^{-8}, 0.0, 0.0
$q^s_{1,i}$ for CO_2, N_2, , O_2 (mol/kg)	1.325, 1.777, 0.603
$q^s_{2,i}$ for CO_2, N_2, , O_2 (mol/kg)	2.233, 0.0, 0.0
$q^s_{3,i}$ for CO_2, N_2, , O_2 (mol/kg)	1.880, 0.0, 0.0
k_i for CO_2, N_2, , O_2 (s^{-1})	1.0, 1.0, 1.0

Table 4.3 Experimental breakthrough and PSA process parameters.

Breakthrough Parameters	
Feed mole fraction : CO_2, N_2	0.05, 0.95
Feed flow (SLPM)	10.0
Bed temperature (K)	293.15
Pressure (kPa)	117.2
PSA Process Parameters	
Feed mole fraction: CO_2, N_2	0.1592, 0.8408
Bed temperature (K)	338.15, 294.15
High pressure (kPa)	117.9
Low pressure (kPa)	4
LR, LPP step recycle ratio	0.03, 0.2

Table 4.4 Preliminary simulations bed, structured core and process characteristics.

Structured Core Characteristics	
bed diameter (m)	0.098
bed length (m)	0.125
Cell density (cpsi)	600, 741
Adsorbent layer thickness (m)	1.0×10^{-4}, 5.1×10^{-5}
Metal foil thickness (m)	5.2×10^{-5}
Core porosity	0.52, 0.66
Adsorbent bulk density (kg/m^3)	406.49, 241.79

Average side length of triangular channels (m)	1.139×10^{-3}, 1.151×10^{-3}
Average hydraulic diameter of triangular channels (m)	6.578×10^{-4}, 6.647×10^{-4}
Adsorbent Characteristics	
Adsorbent	13X zeolite
Adsorbent layer density (kg/m^3)	1110
Adsorbent layer porosity	0.54
PSA Process Parameters	
Feed mole fraction: CO_2, N_2, O_2	0.1592, 0.8029, 0.0379
Feed and bed temperature (K)	348.15
High pressure (kPa)	101.325
Low pressure (kPa)	5.0
Total cycle time (s)	120
LR, LPP step recycle ratio	0.03, 0.2

Table 4.5 Preliminary simulation performances in terms of CO_2 purity and CO_2 recovery for two different bulk densities and a range of feed throughput.

Run	Bulk Density (kg/m^3)	Feed (s)	HR, LR (s)	EqD, EqU(s)	CnD, LPP (s)	Θ (L_{STP}/h/kg)	CO_2 Purity (vol %)	CO_2 Recovery (vol %)
1	406.49	40	20	6.67	13.33	2317.75	94.50	94.79
2	406.49	40	20	6.67	13.33	2575.27	96.74	94.06
3	406.49	40	20	6.67	13.33	2832.80	98.75	92.93
4	241.79	40	20	6.67	13.33	2596.18	92.25	95.31
5	241.79	40	20	6.67	13.33	3028.88	95.28	93.07
6	241.79	40	20	6.67	13.33	3461.57	95.73	83.52

Table 4.6 Experimental vs corresponding simulation performances in terms of CO_2 purity and CO_2 recovery for a range of feed throughput and cycle step times.

Run	Feed (s)	HR, LR (s)	EqD, EqU (s)	CnD, LPP (s)	T(K)	Θ (L_{STP}/h/kg)	Exp. CO_2 Purity (vol %)	Sim. CO_2 Purity (vol %)	Exp. CO_2 Recovery (vol %)	Sim. CO_2 Recovery (vol %)
1	40	20	6.67	13.33	338.15	4060.19	88.26	87.84	94.90	95.74
2	48	24	8.00	16.00	338.15	3383.49	86.30	87.83	93.59	95.87
3	48	20	8.00	20.00	338.15	3383.49	86.05	87.64	94.01	94.75
4	48	20	8.00	20.00	338.15	4060.19	89.00	90.48	87.07	93.65
5	80	40	13.34	26.66	338.15	2030.10	87.79	87.87	96.36	96.17
6	80	40	13.34	26.66	338.15	2436.11	91.31	90.77	94.00	95.55
7	80	40	13.34	26.66	294.15	2436.11	88.56	88.83	94.70	94.75

Table 4.7 Large scale simulations bed, structured core and process characteristics.

Structured Core Characteristics	
bed diameter (m)	3.14, 1.58, 0.79
bed length (m)	2.67, 1.34, 0.67
Cell density (cpsi)	600
Adsorbent layer thickness (m)	1.0×10^{-4}
Metal foil thickness (m)	5.2×10^{-5}
Core porosity	0.52
Adsorbent bulk density (kg/m^3)	406.49
Average side length of triangular channels (m)	1.139×10^{-3}
Average hydraulic diameter of triangular channels (m)	6.578×10^{-4}
Adsorbent Characteristics	
Adsorbent	13X zeolite
Adsorbent layer density (kg/m^3*)*	1110

Adsorbent layer porosity	0.54
PSA Process Parameters	
Feed mole fraction: CO_2, N_2, O_2	0.1592, 0.8029, 0.0379
Feed and bed temperature (K)	348.15
High pressure (kPa)	110.0
Low pressure (kPa)	5.0
Total cycle time (s)	120, 180
LR, LPP step recycle ratio	0.03, 0.1

Table 4.8 Large scale simulation performances in terms of CO_2 purity and CO_2 recovery for two different cycle times, 3 different bed heights and a range of feed throughput.

Run	Bed Height (m)	Bed diameter (m)	Feed (s)	HR, LR (s)	EqD, EqU(s)	CnD, LPP (s)	Θ (L_{STP}/h/kg)	CO_2 Purity (vol %)	CO_2 Recovery (vol %)
1	2.67	3.14	40	20	6.67	13.33	3000.00	90.05	70.02
2	1.34	1.58	40	20	6.67	13.33	3000.00	91.32	85.70
3	0.67	0.79	40	20	6.67	13.33	3000.00	91.79	92.53
4	0.67	0.79	40	20	6.67	13.33	3282.23	92.83	91.63
5	0.67	0.79	40	20	6.67	13.33	3767.86	94.21	90.01
6	0.67	0.79	40	20	6.67	13.33	4726.41	96.06	90.39
7	0.67	0.79	60	30	6.67	23.33	2411.43	93.69	92.31
8	0.67	0.79	60	30	6.67	23.33	2712.59	94.87	91.26
9	0.67	0.79	60	30	6.67	23.33	3000.00	95.65	90.13
10	0.67	0.79	60	30	6.67	23.33	3282.23	96.32	88.46

Table 4.9. Initial and boundary conditions of the 3-bed 7-step PSA cycle schedule. The cycle step sequence is F, HR, EqD, CnD, LR, EqU and LPP.

Condition	Step I, F	Step II, HR	Step III, EqD	Step IV, CnD	Step V, LR	Step VI, EqU	Step VII, LPP
$t = 0^b$	$y_i = y_{i,LPP,f}$ $v = v_{LPP,f}$ $q_i = q_{i,LPP,f}$ $P = P_{LPP,f}$	$y_i = y_{i,F,f}$ $v = v_{F,f}$ $q_i = q_{i,F,f}$ $P = P_{F,f}$	$y_i = y_{i,HR,f}$ $v = v_{HR,f}$ $q_i = q_{i,HR,f}$ $P = P_{HR,f}$	$y_i = y_{i,EqD,f}$ $v = v_{EqD,f}$ $q_i = q_{i,EqD,f}$ $P = P_{EqD,f}$	$y_i = y_{i,CnD,f}$ $v = v_{CnD,f}$ $q_i = q_{i,CnD,f}$ $P = P_{CnD,f}$	$y_i = y_{i,LR,f}$ $v = v_{LR,f}$ $q_i = q_{i,LR,f}$ $P = P_{LR,f}$	$y_i = y_{i,EqU,f}$ $v = v_{EqU,f}$ $q_i = q_{i,EqU,f}$ $P = P_{EqU,f}$
$z/L = 0^c$	$y_i = y_{i,F}$ $F = F_F$ LDFE MB	$y_i = y_{i,LR,z/L=0}$ $F = -F_{LR,z/L=0}$ LDFE MB	CMB VE ($P_o = P_{Eq}$, $c_v = 0$) LDFE MB	CMB OMB LDFE VE ($P_o = P_L$, $c_v > 0$)	CMB OMB LDFE VE ($P_o = P_L$, $c_v > 0$)	CMB VE ($P_o = P_{Eq}$, $c_v = 0$) LDFE MB	CMB VE ($P_o = P_L$, $c_v = 0$) LDFE MB
$z/L = 1^c$	CMB OMB LDFE VE ($P_o = P_H$, $c_v > 0$)	CMB OMB LDFE VE ($P_o = P_H$, $c_v > 0$)	CMB OMB LDFE VE ($P_o = P_{Eq}$, $c_v > 0$)	CMB VE ($P_o = P_L$, $c_v = 0$) LDFE MB	$y_i = y_{i,F,z/L=1}$ $F = -\gamma_1 F_{F,z/L=1}$ LDFE MB	$y_i = y_{i,EqD,z/L=1}$ $F = -F_{EqD,z/L=1}$ LDFE MB	$y_i = y_{i,F,z/L=1}$ $F = -\gamma_2 F_{F,z/L=1}$ LDFE MB

[a] CMB: component mass balance, equation (2); OMB: overall mass balance, equation (1); LDFE: linear driving force equation, equation (4); MB: momentum balance, equation (9); VE: valve equation, equation (13); F: molar flow rate; P_o: Pressure outside the valve; P_L: low pressure; P_H: high pressure; P_{Eq}: equalization pressure; γ_1:fraction of light gas produced during F step used to purge the bed in LR step and γ_2:fraction of light gas produced during F step used to pressurize the bed in LPP step.

[b] The subscript f denotes the end of the cycle step.

[c] The molar flow rate F is assumed positive when gas is flowing towards z/L = 1 and negative when gas is flowing towards z/L = 0.

4.10 FIGURES

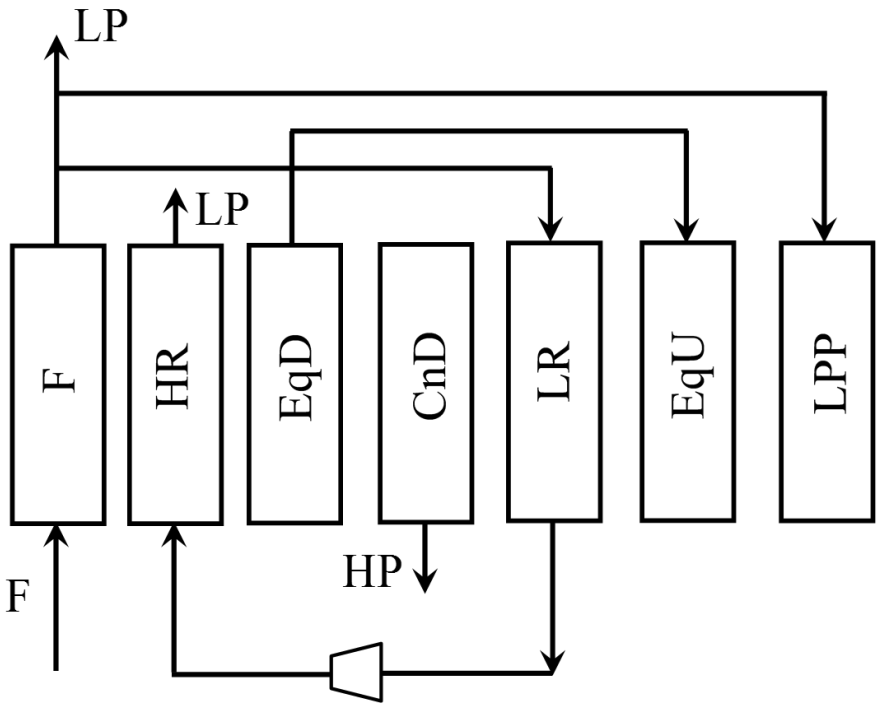

(a)

1	**F**			**HR**	**Eq D**	**CnD**	**LR**	**Eq U**	**LPP**
2	**HR**	**Eq D**	**CnD**	**LR**	**Eq U**	**LPP**	**F**		
3	**LR**	**Eq U**	**LPP**	**F**			**HR**	**Eq D**	**Cn D**

(b)

Figure 4.1 3-bed 7-step PSA cycle schedule F = feed, HR = heavy reflux, EqD = equalization down, CnD = countercurrent depressurization, LR = light reflux, EqU = equalization up, LPP = light product pressurization, LP = light product and HP = heavy product. The first column to the left in the table indicates the bed number.

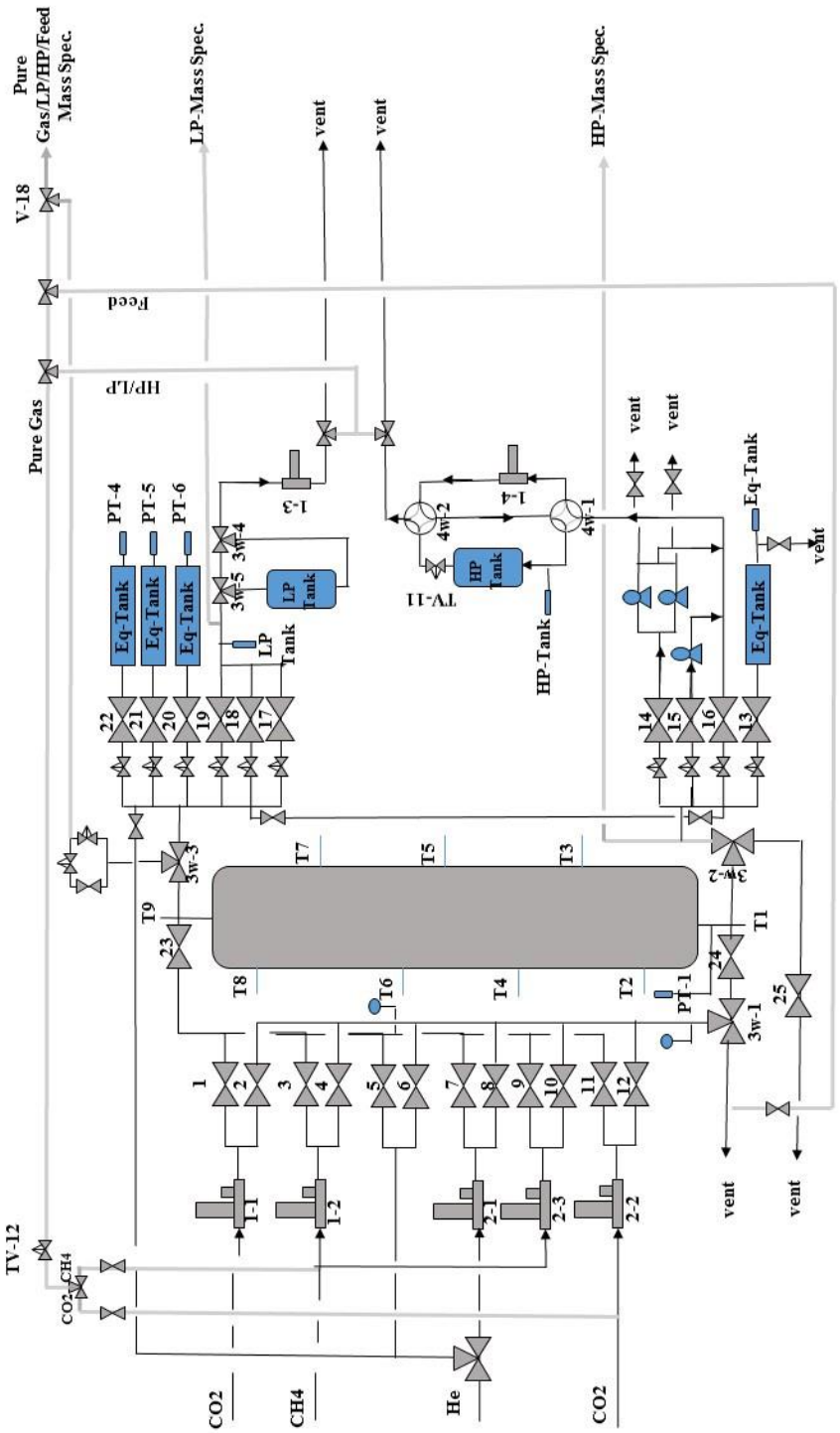

Figure 4.2 Schematic diagram of the single bed PSA apparatus used to study CO_2/N_2 separation with 13X zeolite structured adsorbent.

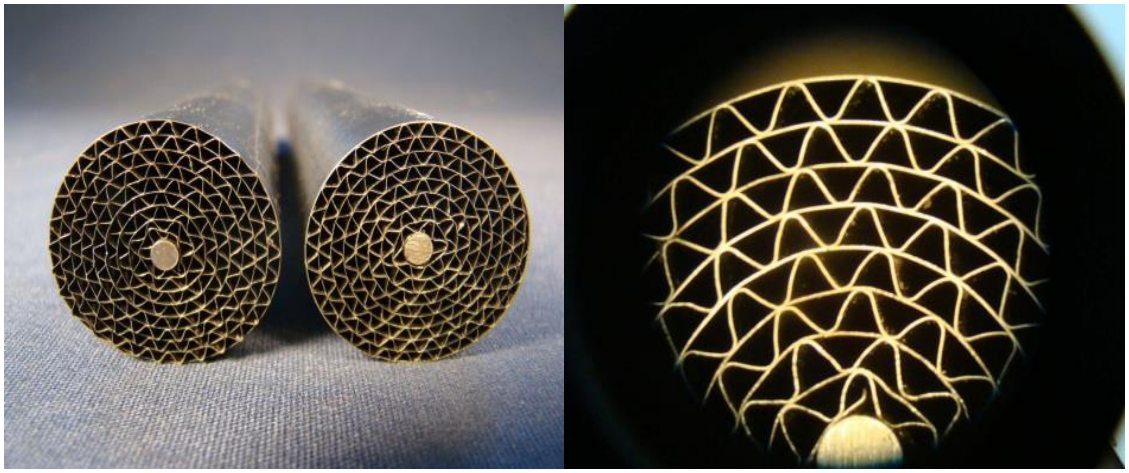

Figure 4.3 A sample of Catacel corrugated structures with triangular channels.

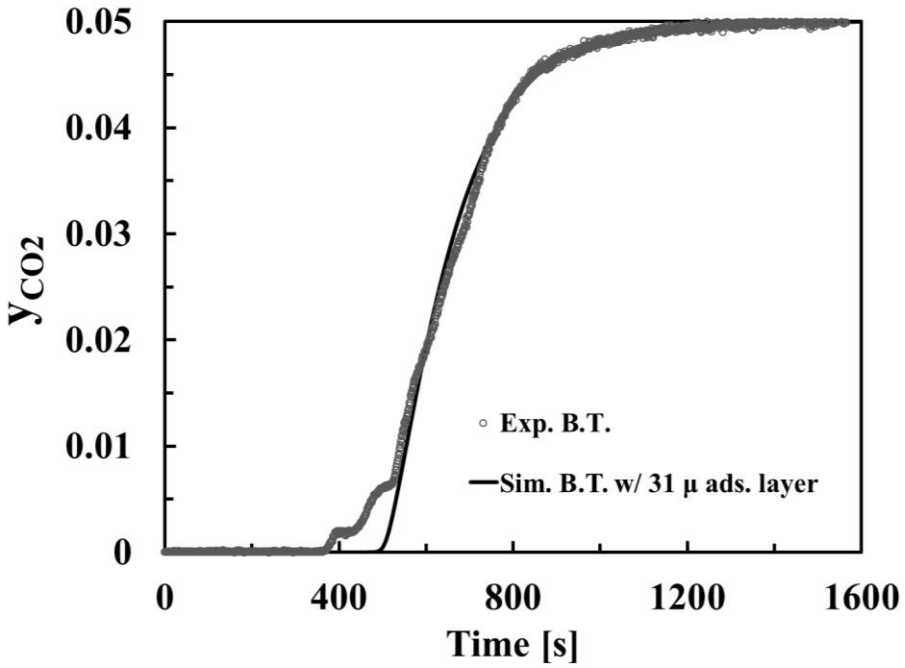

Figure 4.4 Experimental breakthrough curve of structured adsorbent bed for 10 SLPM of feed with CO_2:N_2 ratio of 5:95 vol% vs. DAPS simulation results carried out with 31 μm thick 13X adsorbent layer.

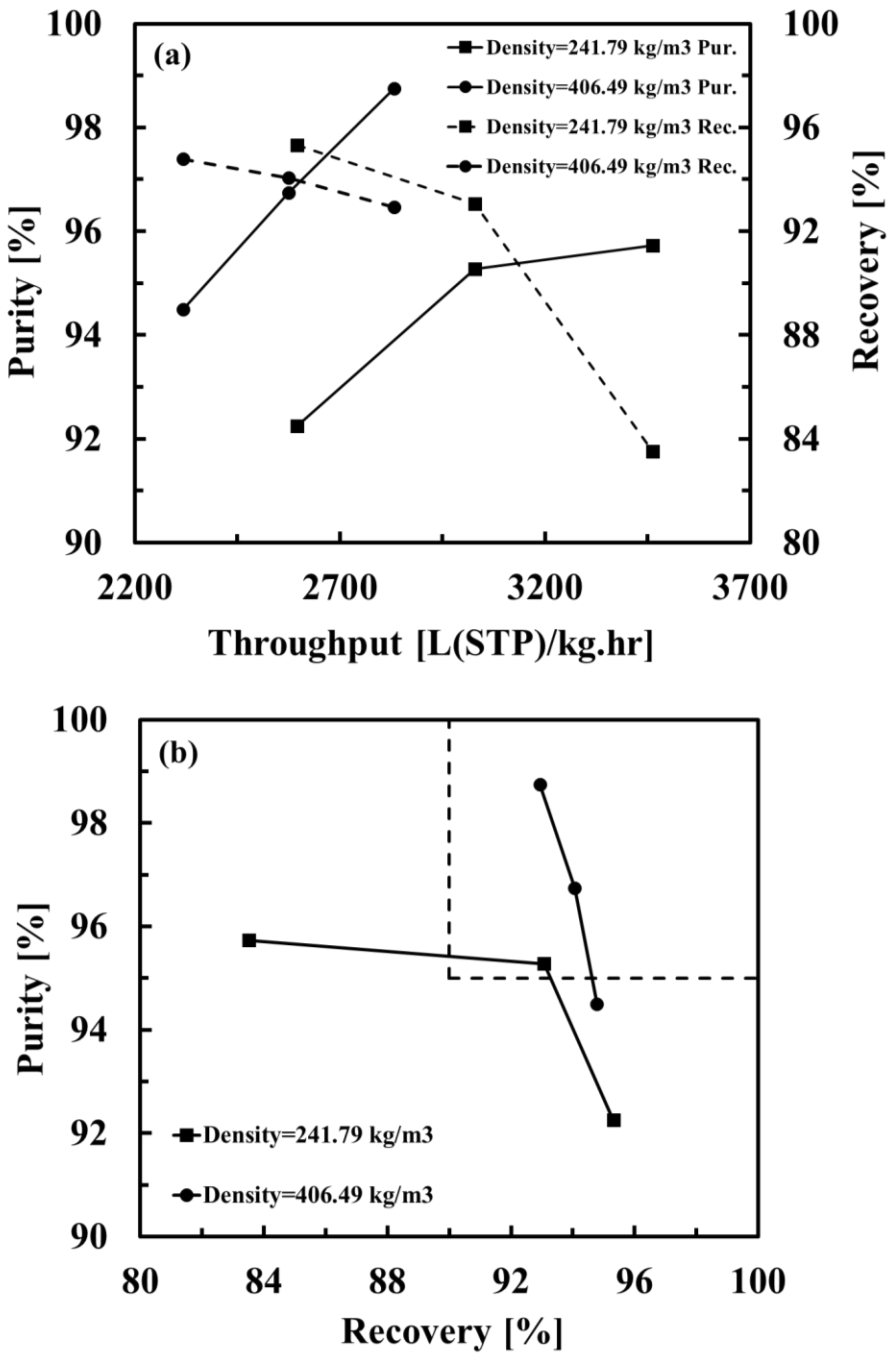

Figure 4.5 Performance of the 3-bed 7-step PSA cycle schedules in preliminary simulation study. Effect of feed throughput and adsorbent bulk density on the CO_2 purity and CO_2 recovery with a) purity vs throughput and recovery vs throughput and b) purity vs recovery.

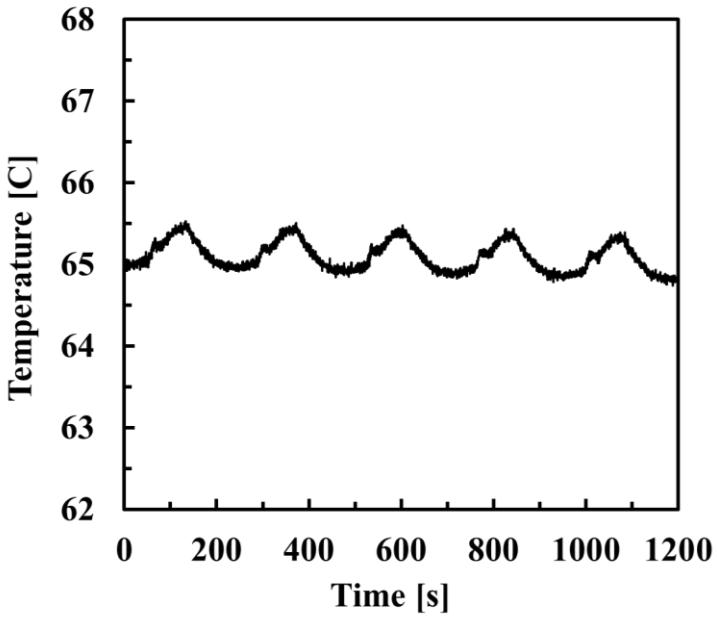

Figure 4.6 Periodic state temperature history for five consecutive cycles of run 5 recorded at the central location along the bed with thermocouple touching the outer metal wall of the core.

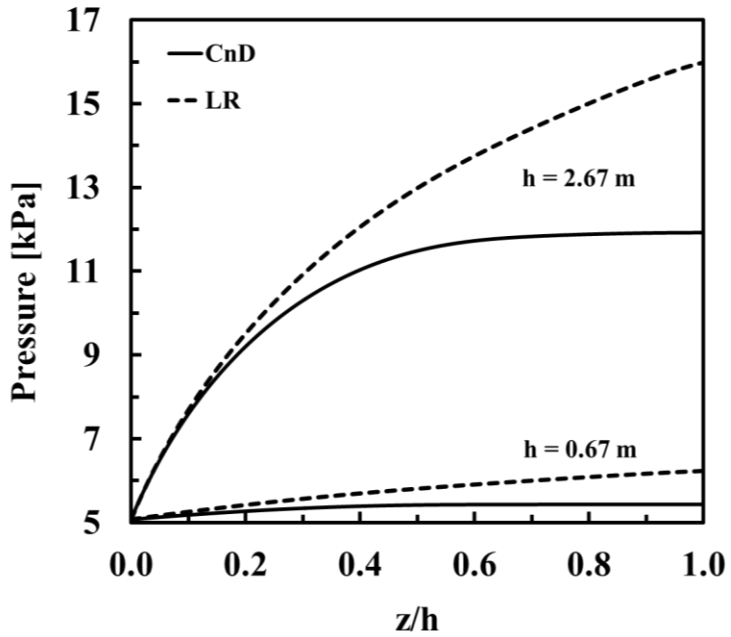

Figure 4.7 Pressure profiles along the scaled up bed at the End of CnD and LR Steps for two different bed heights.

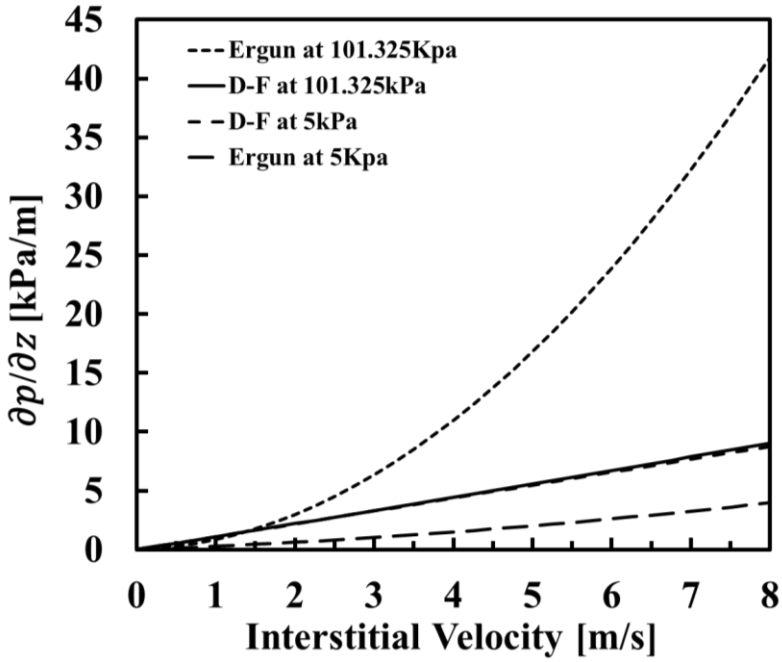

Figure 4.8 Pressure drop prediction for Ergun Eq, Vs Darcy-Forchheimer Eq. in a range of interstitial velocity and for two different total pressure conditions of 5 and 101.325 kPa.

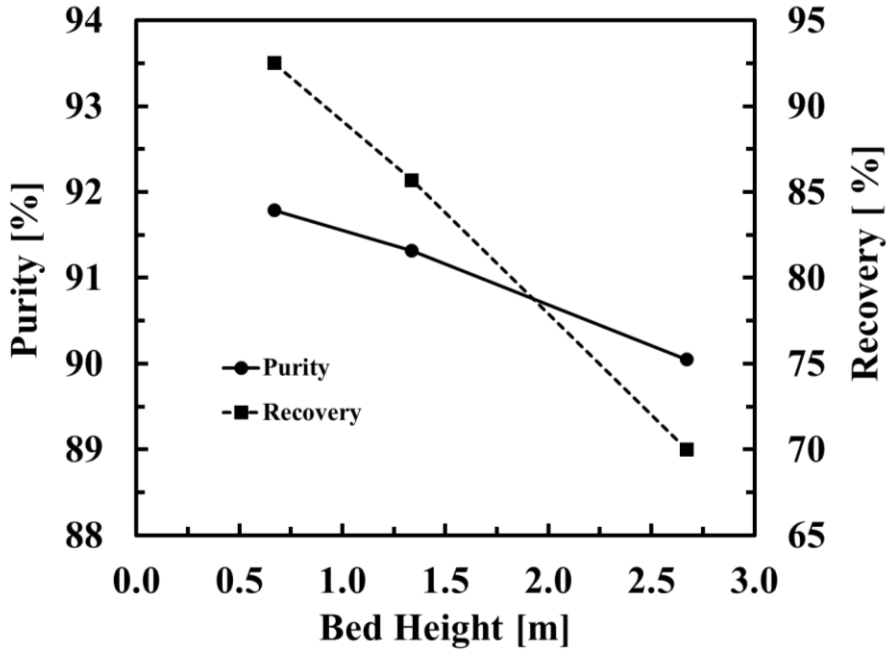

Figure 4.9 Effect of bed height on the performance of the 3-bed 7-step PSA cycle schedule.

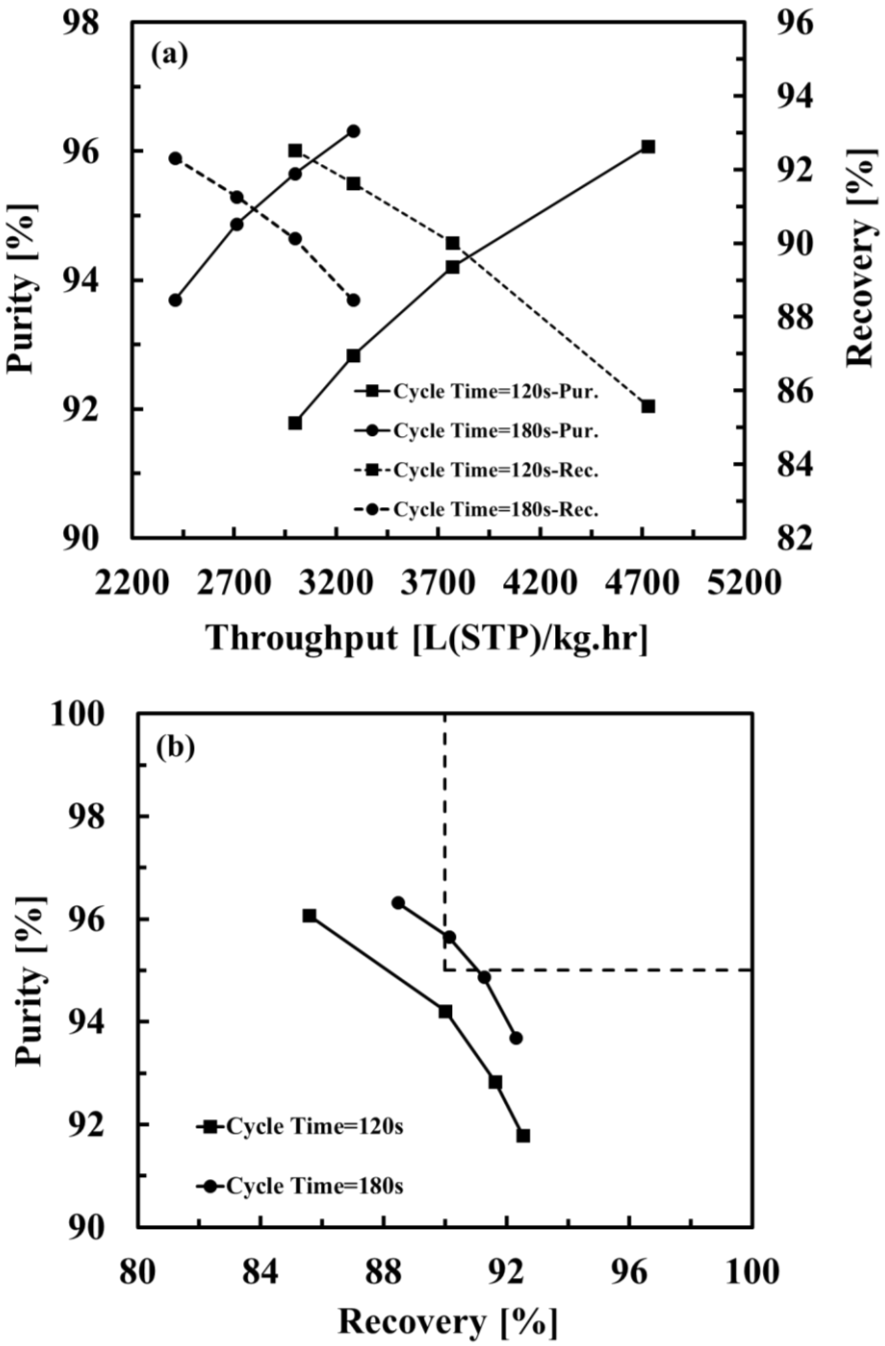

Figure 4.10 Performance of the 3-bed 7-step PSA cycle schedule for the system with 0.67 m long beds and two different cycle times. Effect of feed throughput and total cycle time on the CO_2 purity and CO_2 recovery with a) purity vs throughput and recovery vs throughput and b) purity vs recovery.

REFERENCES

[1] Sircar, S. "Separation of Methane and Carbon Dioxide Gas Mixtures by Pressure Swing Adsorption" *Sep. Sci. Technol.* **1988,** 23, 519–529.

[2] Cavenati, S.; C. A. Grande and A. E. Rodrigues "Layered Pressure Swing Adsorption for Methane Recovery From CH_4/ CO_2/ N_2 Streams" *Adsorption* **2005a,** 11, 549–554.

[3] Mulgundmath V. P.; Tezel F. H.; Saatcioglu T. and Golden T. C. "Adsorption and Separation of CO_2/N_2 and CO_2/ CH_4 by 13X Zeolite" *The Canadian Journal of Chemical Engineering* **2012,** 90,730-738.

[4] Ko D.; Siriwardane R.; Biegler L.T. "Optimization of Pressure Swing Adsorption Process Using Zeolite 13X for CO_2 sequestration" *Ind. Eng. Chem. Res*. **2003,** 42, 339-348.

[5] Santos J. C.; Cruz P.;Regala T.; Magalhães F. D.; and Mendes A. "High-Purity Oxygen Production by Pressure Swing Adsorption" *Ind. Eng. Chem. Res.* **2007,**46, 591.

[6] Da Silva F.A.; Rodrigues A.E. "Propylene/propane separation by vacuum swing adsorption using 13X zeolite" *AIChE Journal* **2001,** 47, 341–357.

[7] Park Y.; Moon D.K.; Kim Y.H.; Ahn H. and Lee C.H. "Adsorption isotherms of CO_2, CO, N_2, CH_4, Ar and H_2 on activated carbon and zeolite LiX up to 1.0 MPa" *Adsorption* **2014,** 20, 631–647.

[8] Siperstein, F.; Gorte, R.J.; Myers, A. L. "A New Calorimeter for Simultaneous Measurements of Loading and Heats of Adsorption from Gaseous Mixtures" *Langmuir* **1999**, *15*, 1570-1576.

[9] Do D. D. "*Adsorption Analysis: Equilibria and Kinetics*" Series in Chem. Eng., Imperial College Press, **1998**.

[10] Ritter J, A.; Bhadra, S.J.; Ebner, A.D. "On the Use of the Dual-Process Langmuir Model for Correlating Unary Equilibria and Predicting Mixed-Gas Adsorption Equilibria" *Langmuir* **2011**, 27, 4700–4712

[11] Pan, H; Ritter, J. A.; Balbuena, P. B. "Examination of the Approximations Used in Determining the Isosteric Heat of Adsorption from the Clausius Clapeyron Equation" *Langmuir* **1998**, 14, 6323.

[12] Bhadra S. J.; Ebner A. D. and J. A. Ritter "On the Use of the Dual Process Langmuir Model for Predicting Unary and Binary Isosteric Heats of Adsorption" *Langmuir* **2012**, 28, 6935−6941.

[13] Yang R.T., "*Adsorbents: Fundamentals and Applications*" John Wiley & Sons, Hoboken, New Jersey, **2003**.

[14] Dunne J.A.; Rao M.; Sircar S.; Gorte R.J. and A.L. Myers, "Calorimetric heats of adsorption and adsorption isotherms .2. O-2, N-2, Ar, CO_2, CH_4, C2H6, and SF6 on NaX, H-ZSM-5, and Na-ZSM-5 zeolites" *Langmuir* **1996,** 12, 5896–5904.

[15] Deng H.; Yi H.; Tang X.; Yu Q.; Ning P. and Yang L. "Adsorption equilibrium for sulfur dioxide, nitric oxide, carbon dioxide, nitrogen on 13X and 5A zeolites" *Chemical Engineering Journal* **2012,**188, 77–85.

[16] Li J.R.; Kuppler R. J. and Zhou H.C. "Selective gas adsorption and separation in metal–organic frameworks" *Chem. Soc. Rev.* **2009**, 38, 1477–1504.

[17] Ruthven D. M. ; Thaeron C., "Performance of a parallel passage adsorbent contactor" *Gas. Sep. Purif.*, **1996**, 10, 63.

[18] Rezaei F. ; Mosca A.; Webley P.; Hedlund J. ; Xiao P. "Comparison of Traditional and Structured Adsorbents for CO_2 Separation by Vacuum-Swing Adsorption" *Ind. Eng. Chem. Res.* **2010**, *49,* 4832–4841.

[19] Kodama, A.; Goto, M.; Hirose, T. ; Kuma, T. "Experimental study of optimal operation for a honeycomb adsorber operated with thermal swing" *J. Chem. Eng. Jpn.* **1993**, 26, 530.

[20] Gadkaree, K. P. "System and method for adsorbing contaminants and regenerating the adsorber" U.S. Patent 5,658,372, **1997**.

[21] Li, Y. Y.; Perera, S. P.; Crittenden, B. D. "Zeolite monoliths for air separation, part 2: Oxygen enrichment, pressure drop and pressurization" *Chemical Engineering Research and Design* **1998**, 76 (A8), 931.

[22] Brandani, F.; Rouse, A.; Brandani, S.; Ruthven, D. M. "Adsorption kinetics and dynamic behavior of a carbon monolith" *Adsorption* **2004**, 10,99.

[23] Li, L.; Xue, B.; Chen, J.; Guan, N.; Zhang, F.; Liu, D.; Feng, H. "Direct synthesis of zeolite coatings on cordierite supports by in situ hydrothermal method" *Appl. Catal.*, A **2005**, 292, 312.

[24] Lee, L. Y.; Perera, S. P.; Crittenden, B. D.; Kolaczkowski, S. T. "Manufacture and characterisation of silicalite monoliths" *Adsorpt. Sci. Technol.* **2000**, 18, 147.

[25] Yu, F. D.; Luo, L. A.; Grevillot, G. "Adsorbption isotherms of VOCs onto an activated carbon monolith: Experimental measurement and correlation with different models" *J. Chem. Eng. Data* **2002**, 47, 467.

[26] Yates, M.; Blanco, J.; Martin-Luengo, M. A.; Martin, M. P. "Vapour adsorption capacity of controlled porosity honeycomb monoliths" *Microporous Mesoporous Mater.* **2003**, 65, 219.

[27] Farooq S., Thaeron C., Ruthven D. M., "Numerical simulation of a parallel-passage piston-driven PSA unit" *Separation and Purification Technology*, **1998**, *13*, 181.

[28] Hyungwoong A., Brandani S., "Analysis of Breakthrough Dynamics in Rectangular Channels of Arbitrary Aspect Ratio" *AIChE Journal*, **2005**, *51*.

[29] Rezaei F., Webley P., "Structured adsorbents in gas separation processes" *Separation and Purification Technology*, **2010**, *70*, 243.

[30] Ruthven D. M.; Thaeron C., "Performance of a parallel passage adsorbent contactor" *Gas. Sep. Purif.*, **1996**, 10, 63.

[31] Rezaei F. ; Mosca A.; Webley P.; Hedlund J. ; Xiao P. "Comparison of Traditional and Structured Adsorbents for CO_2 Separation by Vacuum-Swing Adsorption" *Ind. Eng. Chem. Res.* **2010**, *49*, 4832–4841.

[32] Kodama, A.; Goto, M.; Hirose, T.; Kuma, T. "Experimental study of optimal operation for a honeycomb adsorber operated with thermal swing" *J. Chem. Eng. Jpn.* **1993**, 26, 530.

[33] Gadkaree, K. P. "System and method for adsorbing contaminants and regenerating the adsorber" U.S. Patent 5,658,372, **1997**.

[34] Li, Y. Y.; Perera, S. P.; Crittenden, B. D. "Zeolite monoliths for air separation, part 2: Oxygen enrichment, pressure drop and pressurization" *Chemical Engineering Research and Design* **1998**, 76 (A8), 931.

[35] Brandani, F.; Rouse, A.; Brandani, S.; Ruthven, D. M. "Adsorption kinetics and dynamic behavior of a carbon monolith" *Adsorption* **2004**, 10, 99.

[36] Li, L.; Xue, B.; Chen, J.; Guan, N.; Zhang, F.; Liu, D.; Feng, H. "Direct synthesis of zeolite coatings on cordierite supports by in situ hydrothermal method" *Appl. Catal.*, A **2005**, 292, 312.

[37] Lee, L. Y.; Perera, S. P.; Crittenden, B. D.; Kolaczkowski, S. T. "Manufacture and characterisation of silicalite monoliths" *Adsorpt. Sci. Technol.* **2000**, 18, 147.

[38] Yu, F. D.; Luo, L. A.; Grevillot, G. "Adsorption isotherms of VOCs onto an activated carbon monolith: Experimental measurement and correlation with different models" *J. Chem. Eng. Data* **2002**, 47, 467.

[39] Yates, M.; Blanco, J.; Martin-Luengo, M. A.; Martin, M. P. "Vapor adsorption capacity of controlled porosity honeycomb monoliths" *Microporous Mesoporous Mater.* **2003**, 65, 219.

[40] Celata G.P.; Chmiel K.; Kulenovic R.; Martin-Callizo C.; McPhail S.; Mertz R.; Owhaib W.; Palm B.; Sobierska E.; Zummo G. "Frictional Pressure Drop in Single-Phase Flow in Narrow Channels" *Proceedings of ICNMM2006, Fourh International Conference on Nanochannels, Microchannels and Minichannels* **2006**, 717-724.

[41] Mala G.M.; Li D. "Flow characteristics of water in microtubes" *International Journal of Heat and Fluid Flow* **1999,** 20, 142–148.

[42] Peng X.F.; Peterson G.P.; Wang B.X. "Frictional Flow Characteristics of Water flowing Through Rectangular Microchannels" *Experimental Heat Transfer* **1994**, 7, 249-264.

[43] Qu W.; Mala Gh. M.; Li D. "Heat Transfer for Water Flow in Trapezoidal Silicon Microchannels" *Int. J. Heat Mass Transfer* **2000**, 43, 3925-3936.

[44] Flockhart S.M.; Dhariwal R.S. "Experimental and Numerical Investigation into the Flow Characteristics of Channels Etched in <100> Silicon" *J. Fluids Engng* **1998**, 120, 291-295.

[45] Judy J.; Maynes D.; Webb B.W. "Characterisation of Frictional Pressure Drop for Liquid Flows through Microchannels" *Int. J. Heat and Mass Transfer* **2002**, 45, 3477-3489.

[46] Wu H.Y.; Cheng P. "Friction Factors in Smooth Trapezoidal Silicon Micro-Channels with Different Aspect Ratios" *Int. J. Heat Mass Transfer* **2003**, 46, 2519-2525.

[47] Yang C.Y.; Wu J.C.; Chien H.T.; Lu S.R. "Friction Characteristics of Water, R-134a and Air in Small Tubes" *Microscale Termophys. Eng.* **2003**, 253-256.

[48] Hetsroni G.; Mosyak A.; Pogrebnyak E.; Yarin L.P. "Fluid Flow in Micro-Channels" *Int. J. Heat Mass Transfer* **2005**, 48, 1982-1998.

[49] Perry R.H.; Green D. "Perry's Chemical Engineers' Handbook" *McGraw-Hill, New York, USA* **1984** 6th edition.

[50] Shah, R.K.; Bhatti, M.S. "Laminar convective heat transfer in ducts, in Handbook of Single-Phase Convective Heat Transfer" *Wiley, New York, USA* **1987**Chap 3.

[51] Shah, R.K.; London, A.L. “Advances in Heat Transfer: Laminar Flow Forced Convection in Ducts” **1978** *Academic Press, New York, USA.*

[52] Sadasivam, R.; Manglik, R.M.; Jog, M.A. “Fully developed forced convection through trapezoidal and hexagonal ducts” *Int J Heat Mass Transfer* **1999,** 42, 4321–4331.

[53] White, C.M.; Strazisar, B.R.; Granite, E.J.; Hoffman, J.S.; Pennline, H.W. “Separation and Capture of CO_2 from Large Stationary Sources and Sequestration in Geological Formations—Coalbeds and Deep Saline,” *J. Air Waste Manage. Assoc.*, 53, 645–715 (**2003**).

[54] Reynolds, S. P.; Mehrotra, A.; Ebner, A. D.; Ritter, J. A. “Heavy Reflux PSA Cycles for CO_2 Recovery from Flue Gas Part I. Performance Evaluation,” *Adsorption*, 14, 399–413(**2008**).

[55] Haszeldine, R.S. “Carbon Capture and Storage: How Green Can Black Be?,” *Science*, 325(5948), 1647–1652 (**2009**).

[56] Ebner, A.D.; Ritter, J.A. “State-of-the-Art Adsorption and Membrane Separation Processes for Carbon Dioxide Production from Carbon Dioxide Emitting Industries” *Separation Science and Technology*, 44, 1273–1421 (**2009**).

[57] Ribeiro, R.P.P.L.; Grande, C.A.; Rodrigues, A.E. “Activated Carbon Honeycomb Monolith – Zeolite13X Hybrid System to Capture CO_2 from Flue Gases Employing Electric Swing Adsorption,” *Chemical Engineering Science*, 104, 304–318(**2013**).

[58] Krishnamurthy, S.; Rao, V. R.; Guntuka, S.; Sharratt, P.; Haghpanah, R.; Rajendran, A.; Amanullah, M.; Karimi, I. A.; Farooq, S. “CO_2 Capture from Dry Flue Gas by Vacuum Swing Adsorption: A Pilot Plant Study” *AIChE Journal*, 60(5), 1830 (**2014**).

[59] Reynolds ,S. P.; Ebner, A. D.; Ritter, J. A. “Stripping PSA Cycles for CO_2 Recovery from Flue Gas at High Temperature Using a Hydrotalcite-Like Adsorbent,” *Ind. Eng. Chem. Res.*, 45, 4278-4294 (**2006**).

[60] Xiao, P.; Zhang, J.; Webley, P.; Li, G.; Singh, R.; Todd, R. “Capture of CO_2 from F lue Gas Streams with Zeolite 13X by Vacuum- Pressure Swing Adsorption,” *Adsorption*, 14, 575 (**2008**).

[61] Zhang, J.; Webley, P. A. “Cycle Development and Design for CO_2 Capture from Flue Gas by Vacuum Swing Adsorption,” *Environmental Science &Technology* 42, 563–569 (**2008**).

[62] Liu, Z.; Wang, L.; Kong, X.; Li, P.; Yu, J.; Rodrigues, A. E. “Onsite CO_2 Capture from Flue Gas by an Adsorption Process in a Coal-Fired Power Plant,” *Ind. Eng. Chem. Res.*, 51(21), 7355–7363 (**2012**).

[63] Rege, S. U.; Yang, R. T. “Kinetic Separation of Oxygen and Argon Using Molecular Sieve Carbon. *Adsorption*” 6, 15−22 (**2000**).

[64] Kim, M. B.; Jee, J. G.; Bae, Y. S.; Lee, C. H. “Parametric Study of Pressure Swing Adsorption Process to Purify Oxygen Using Carbon Molecular Sieve” *Ind. Eng. Chem. Res.* 44, 7208−7217 (**2005**).

[65] Jee, J. G.; Kim, M. B.; Lee, C. H. “Pressure Swing Adsorption Processes to Purify Oxygen Using a Carbon Molecular Sieve” *Chem. Eng. Sci.*, 60, 869−882 (**2005**).

[66] Jin, X.; Malek, A.; Farooq, S. “Production of Argon from an Oxygen-Argon Mixture by Pressure Swing Adsorption” *Ind. Eng. Chem. Res.* 45, 5775−5787 (**2006**).

[67] Mohammadi, N.; Ebner, A. D.; Ritter, J. A. “Adsorption Equilibria of N_2, O_2, Ar, CO_2, CO, CH_4, C_2H_4, C_3H_6, C_2H_6 and C_3H_8 on Zeolite 13X” *Under Review*.

[68] Brown, P. N.; Hindmarsh, A. C.; Petzold, L. R. “Using Krylov Methods in the Solution of Large-Scale Differential-Algebraic Systems,” *SIAM J. Sci. Comp.*, 15, 1467 (**1994**).

[69] Ritter, J. A.; Bhadra, S. J.; Ebner, A. D. “On the Use of the Dual Process Langmuir Model for Correlating Unary and Predicting Mixed Gas Adsorption Equilibria” *Langmuir* 27, 4700−4712 (**2011)**.

[70] Bhadra, S. J.; Ebner, A. D.; Ritter, J. A. “On the Use of the Dual Process Langmuir Model for Predicting Unary and Binary Isosteric Heats of Adsorption” *Langmuir* 28, 6935−6941 (**2012)**.

[71] Mohammadi, N.; Ebner, A. D.; Ritter, J. A. “Experimental and Numerical Study of Pressure Drop in Structured Adsorbents with Narrow Triangular Channels” *Under Review*.